Journal of Wind Engineering & Industrial Aerodynamics 252 (2024) 105769

Contents lists available at ScienceDirect

Journal of Wind Engineering & Industrial Aerodynamics

journal homepage: www.elsevier.com/locate/jweia

Shape- and frequency-dependent self-excited forces emulation for the aero-structural design of bluff deck bridges

Sumit Verma *, Miguel Cid Montoya, Ashutosh Mishra

ASTRO Lab, Texas A&M University-Corpus Christi, Corpus Christi, TX, USA

ARTICLE INFO

Keywords:
Bridge aeroelasticity
Flutter derivatives
Surrogates
CFD simulations
Forced-vibration
Buffeting
Aero-structural optimization

ABSTRACT

The shape design and optimization of bluff decks prone to aeroelastic phenomena require emulating the fluid-structure interaction parameters as a function of the body shape and the oscillation frequency. This is particularly relevant for long- and medium-span bridges equipped with single-box decks that are far from being considered streamlined and for other girder typologies such as traditional truss decks and modern twin- and multi-box decks. The success of aero-structural design frameworks, which are inherently iterative, relies on the efficient and accurate numerical evaluation of the wind-induced responses. This study proposes emulating the fluid-structure interaction parameters of bluff decks using surrogate modeling techniques to integrate them into aero-structural optimization frameworks. The surrogate is trained with data extracted from forced-vibration CFD simulations of a typical single-box girder to emulate the values of the flutter derivatives as a function of the deck shape and reduced velocity. The focus is on deck configurations ranging from streamlined to bluff cross-sections and on low reduced velocities to capture eventual aerodynamic nonlinearities. The girder cross-section geometry is tailored based on its buffeting performance. This design tool is fundamental to finding the optimum balance between the structural and aeroelastic requirements that drive the design of bluff deck bridges.

1. Introduction

Over the past three decades, the trend of designing and building long-span and super-long-span bridges has been on the rise worldwide. The Akashi Kaikyo Bridge in Japan (Kashima et al., 2001), the Xihoumen Bridge in China (Deng et al., 2021), and a more recently completed 1915 Çanakkale Bridge in Turkey (Arıoğlu, 2021) with main span lengths of 1991 m, 1650 m, and 2023 m, respectively, are a few notable examples of long and super-long span bridges. While longer spans are advantageous for traversing large water bodies with a single bridge construction project, the increasing span length also makes a bridge behave more like a slender, flexible structure with pronounced aerodynamic and aeroelastic loading and subsequent responses. Besides, medium-span cable-stayed bridges with span length of around 500 m is also very common in different parts of the world, such as the Constitution Bridge (540 m main span) in Cadiz, Spain (Díaz García et al., 2018); the Harbor Bridge (506 m) in Corpus Christi, USA (TxDOT, 2022); the Gordie Howe International Bridge (853 m) across the USA-Canada border (Martin et al., 2023) and the Cebu-Cordova Link Expressway (390 m) in the Philippines (Cruz et al., 2023). Some of these bridges (TxDOT, 2022; Cruz et al., 2023) are located in hurricane- and typhoon-prone regions and possess relatively bluff deck sections, which significantly impacts their aeroelastic behavior, making these strongly vulnerable to wind-induced instabilities and large aeroelastic responses. This situation is further exacerbated by climate change (Orcesi et al., 2022a, 2022b), which has resulted in the increase in both frequency and intensity of severe windstorms, typhoons, and hurricanes in the past few years, affecting critical infrastructure systems such as bridges (Nasr et al., 2020). Thus, it is of paramount importance to provide due consideration to the aerodynamic aspect of streamlined and bluff bridge decks in addition to meeting the structural load demands before finalizing the design of medium- and long-span bridges.

The design of contemporary bridge decks involves dealing simultaneously with responses of structural and aeroelastic nature, hence addressing the design problem from a holistic aero-structural perspective (Cid Montoya, 2024). This requires handling design requirements, such as deck and tower displacements under live loads, stresses developed at the member level, and global aeroelastic responses, such as buffeting-induced responses and flutter and aerostatic instability, among others, that can involve contradictory design modifications.

* Corresponding author.
E-mail addresses: sumit.verma@tamucc.edu (S. Verma), miguel.cidmontoya@tamucc.edu (M. Cid Montoya), amishra1@islander.tamucc.edu (A. Mishra).

https://doi.org/10.1016/j.jweia.2024.105769
Received 29 December 2023; Received in revised form 22 April 2024; Accepted 14 May 2024

Besides their clear influence on the structural responses, deck shape design modification impacts the aeroelastic responses by means of changes in (a) the mechanical properties (e.g., natural frequencies, mode shapes, etc.) and (b) the aerodynamic and aeroelastic characteristics (e.g., force coefficients, flutter derivatives, admittance functions, etc.). The direct relationship of the deck cross-section with most of the critical bridge responses turns its definition into a fundamental step in the bridge design characterized by its complexity due to the nonlinear nature of bluff body aerodynamics and bridge aeroelasticity (Shiraishi and Matsumoto, 1983; Lin et al., 2005; Kareem and Wu, 2013, 2015). Besides shape modifications, the use of appendages, as well as passive and active flow control methods, have also been proposed to mitigate wind-induced responses (Xue et al., 2021; Wang et al., 2023). However, shape modification remains one of the most cost-effective and functional techniques to improve the aeroelastic performance of bridges compared to adding appendages or countermeasures, which involve higher installation and maintenance costs (Larsen and Wall, 2012).

Developing aero-structural bridge design tools requires the accurate numerical evaluation of the shape-dependent wind-induced responses. In order to overcome the traditional heuristic-based sequential analysis (Chen and Duan, 1999; Cid Montoya et al., 2018a proposed a numerical methodology based on the combination of surrogate models, computational fluid dynamics (CFD) simulations of the bridge aerodynamics, and the quasi-steady theory (QST). The QST (Scanlan, 1987; Chen and Kareem, 2002; Tubino, 2005) permits the approximation of fluid-structure interaction parameters such as flutter derivatives and admittance functions by using the force coefficients and their slopes, reducing the CFD simulations' computational burden because only static simulations are needed. This approach shows a good performance for streamlined geometries at high reduced velocities (Chen and Kareem, 2003; Wu and Kareem, 2013), which is adequate for the evaluation of ultimate limit states such as flutter instability or buffeting response at high wind velocities. However, a major shortcoming of the QST model is its inability to take into account the fluid memory effect (Chen and Kareem, 2003; Wu and Kareem, 2013; Kavrakov and Morgenthal, 2017) in the aerodynamic characterization of flow. In other words, the QST model assumes that the structure is oscillating with such low frequencies that the fluid particle interacting at the frontal end of the structure (deck section) passes around the deck and through to the wake region on the downstream side even before the structure could respond to the flow field (which is applicable for cases when the reduced velocity $U^* \rightarrow \infty$). These assumptions make the QST approach suitable for application in the higher reduced velocity ranges, and that too mostly for streamlined deck sections. As the deck section becomes bluffer, which may be necessary in certain instances to enhance the mechanical properties of the bridge to account for certain bridge loading conditions, the QST model shows poor performance (Øiseth et al., 2011). The shortcomings of the QST model were first highlighted by Diana et al., 1993, when comparing the aeroelastic analyses of the Humber bridge to full-scale monitoring data (Bocciolone et al., 1992). Similarly, the manifestation of the poor performance of QST model in the severe underestimation of the stability limit of the Hardanger bridge in Norway was emphasized by Øiseth et al., 2010, thus leading the authors to conclude that the traditional QST was inadequate to model the self-excited forces in coupled flutter or buffeting response analysis when compared to full bridge monitoring measurements. In addition, the QST model is not suited for application in bridge typologies other than the streamlined single-box decks such as the twin-box decks of the Xihoumen bridge (Deng et al., 2021) or Stonecutters bridge (Hui and Wong, 2009) and truss bridges like the Akashi Kaikyo bridge (Kashima et al., 2001), Verrenzano bridge (Kinney et al., 1966), and Golden Gate bridge (Ludke, 2013). The effect of gap-width on the aerodynamic behavior of twin-box decks and subsequent responses is detailed in Kwok et al., 2012; Laima and Li, 2015, and the limitations of the QST model for application in bluff decks and twin-box decks are highlighted in Febo and D'Asdia, 2010; Nieto et al., 2020. Similarly, in the case of truss bridges, the estimated flutter derivatives from the QST formulation show relevant variations in magnitude when compared to the experimental results as reported by Russo et al., 2023 for the Akashi-Kaikyo bridge. Hence, it can be inferred that the QST model fares from poor performance when applied to twin-box (or multi-box) decks and truss bridges, and thus, a more elaborate extraction of aeroelastic parameters obtained from an actual fluid-structure interaction study is necessary for buffeting analysis and a better estimation of flutter stability limits.

In addition, the QST assumes frequency independence (Lazzari, 2005) in aeroelastic loading of bridge decks (i.e., the flutter derivatives are independent of the frequency of oscillation of the deck). However, the fundamental mechanism driving the phenomenon of aeroelastic flutter is the addition of flow energy into the structural system, leading to the increase in total potential energy of the structure, which ultimately leads to instabilities and, thus, divergent oscillations (Dyrbye and Hansen, 1997; Abbas et al., 2017). Alternately, the flow energy derived from the aerodynamic forces (harmonically oscillating with a specific frequency) under a certain condition of phase lead/lag relation with the structural motion starts feeding energy to the structural system leading to flutter instability (Dyrbye and Hansen, 1997). This underscores the necessity to consider the frequency-dependent aeroelastic loading (Lazzari et al., 2004; Diana et al., 2013a, 2013b) in the preliminary design of medium and long-span bridges. For that purpose, either free vibration (Sarkar et al., 1994; Iwamoto and Fujino, 1995; Mannini, 2006; Argentini et al., 2022) or forced vibration (Matsumoto et al., 1996; Neuhaus et al., 2009; Wu et al., 2020; Diana and Omarini, 2020) tests in the wind tunnel can be carried out to identify the flutter derivatives. However, the necessity to conduct either the forced vibration or free vibration wind tunnel tests for multiple deck shape candidates along the design process makes the experimental approach a costly pursuit for design purposes, and its applicability is typically limited to the validation of final designs and for addressing minor modifications (Argentini et al., 2022). An alternative cost-effective approach to expensive experimental testing is to solve the flow field around a dynamically oscillating bridge deck numerically using the Navier--Stokes' (NS) equation with appropriate boundary conditions, which has also gained popularity over the past few years (Frandsen, 2004; Selvam et al., 2002; Šarkić et al., 2012; Brusiani et al., 2013; Sun et al., 2009; Sarwar et al., 2008; Mannini et al., 2016; Fransos and Bruno, 2010). With the aid of a numerically solved flow field obtained from CFD simulation, the unsteadiness in the flow (or, alternately, the fluid memory effect) can be properly accounted for in addition to the aerodynamic non-linearities. Thus, CFD simulations offer a cost-effective, viable solution to experimental testing during the deck shape design process. In this study, we adopt this approach in order to produce a fully numerical design framework that permits the implementation of numerical optimization algorithms to conduct the aero-structural design of bridges. The accuracy of the numerical results obtained throughout CFD simulations is guaranteed by performing multiple verification and validation studies using experimental data. Then, once the CFD-based design optimization is completed, a final experimental validation of the optimized deck can be carried out as is customary in current engineering practice.

On the other hand, adopting surrogate models for emulating aerodynamic parameters permits the creation of smooth response surfaces (Forrester et al., 2008) that guarantee their continuity and differentiability within the design space, which are fundamental properties for their effective use in design frameworks such as those adopting gradient-based optimization algorithms (Haftka and Gürdal, 1992; Hernández, 2010; Arora, 2011). A first contribution in this direction was reported in Cid Montoya et al., 2018b, where a long-span bridge under multiple displacements- and stress-related design constraints along with a flutter instability design constraint was optimized by performing 3D multi-mode flutter analyses. This study highlighted the importance of the shape-dependent mechanical contribution of the deck to the flutter-resistant design. One of the key conclusions of this investigation

was the positive impact of increasing the deck depth for handling static responses such as deck displacements and stresses, but also in increasing the torsional natural frequency, which helped to increase the flutter response. As a consequence, the optimization algorithm tried to increase this value as much as possible, always reaching the maximum depth allowed, i.e., the design variable upper bound formulated in the optimization problem. Similar behavior was observed when conducting bridge aero-structural optimization considering buffeting-induced accelerations (Cid Montoya et al., 2022). These studies, including other similar studies reported in the existing literature (Jaouadi et al., 2020; Tinmitondé et al., 2022; Zheng et al., 2023), all rely on QST-based formulation and aerostatic analyses for the surrogate modeling framework and thus suffer from the limitations of QST-based formulation as highlighted in the previous paragraphs.

Indeed, in some design scenarios, the optimum design with the best combination of the aerodynamic and mechanical properties to fulfill all structural and aeroelastic requirements may be within the design domain where the QST formulation shows an acceptable performance. However, further increasing the deck depth, which is a very efficient way to increase the torsional and vertical stiffness, may lead to bluff deck designs for which the hypothesis of the QST will not hold. This design challenge is conceptually sketched in Fig. 1. This can be the case of medium and not-that-long span bridges, as well as other typologies commonly adopted for long- and super-long span bridges, such as truss decks or multi-box decks, where the QST formulation does not provide enough accuracy for being used in the wind-resistant design without ad hoc corrections (Øiseth et al., 2010; Nieto et al., 2020).

Hence, to perform the aerodynamic and aero-structural design of decks considering design domains involving both streamlined and bluff geometries, as well as considering other scenarios where the QST does not hold, such as low reduced velocities, the aeroelastic characterization of the bridge deck must be advanced to avoid the limitations and assumptions of the QST, such as frequency independence. Thus, in this study, we propose an improved framework based on the direct calculation of the 18 flutter derivatives (Chen et al., 2002; Chowdhury and Sarkar, 2004) using dynamic CFD simulations to directly train the aeroelastic emulator with the fluid-structure interaction parameters as a function of the deck shape and the reduced velocity. Therefore, the methodology adopted is conceived to explore wide shape design domains that include streamlined and bluff deck cross-sections, hence allowing designers and design optimization algorithms to accurately transition back and forward from streamlined to bluff deck cross-sections. With this aim, a kriging surrogate (Krige, 1951; Sacks et al., 1989) is trained to emulate the flutter derivatives of the bridge as a function of the shape and reduced velocity. Force-vibration simulations (Šarkić et al., 2012, 2015; Nieto et al., 2015; Mannini et al., 2016; Zhuo et al., 2022) are used to obtain the time history of aeroelastic forces for further computation of flutter derivatives as per procedures outlined in Xu et al., 2014.

The design framework proposed in this study is introduced in Section 2 and each step is discussed in detail, including the fundamental aerodynamic and aeroelastic formulations for flutter and buffeting analyses, and the surrogate modeling technique adopted. The details about the single-box deck adopted as an application example, which is based on the experimental CRIACIV (Inter-University Research Centre on Building Aerodynamics and Wind Engineering) section from Mannini et al., 2010, are discussed in depth in Section 3, including the definition of design domain, design variables, sampling plan, and the design of experiments. Section 4 is devoted to the full description of the computational modeling aspects adopted for the CFD simulation, including the spatial discretization of the computational domain, and the different verification and validation studies carried out for aerostatic (in the form of time-averaged force coefficients vs. angle of attack) and aeroelastic (flutter derivatives vs. reduced velocity) analyses. The response surfaces of the shape- and frequency-dependent emulator obtained from the kriging surrogate model for all the 18 flutter derivatives are reported in Section 5, whereas Section 6 discusses the influence of the shape-dependent flutter derivatives on the bridge aeroelastic responses. Given that the focus of this piece of research is the nonlinear behavior of the self-excited forces that typically occurs at low reduced velocities, buffeting will be the aeroelastic response under study in order to analyze the response in the three degree-of-freedom independently and to study the response at different reduced velocities. The buffeting responses are later used for tailoring the bridge deck, showing the methodology's effectiveness. Finally, Section 7 summarizes the key conclusions drawn from the different analyses covered in this study and discusses future lines of research.

2. Aero-structural design via emulating shape- and frequency-dependent flutter derivatives

Previous aero-structural design frameworks developed for bridges with streamlined deck cross-sections resulted in effective and powerful design tools for improving the wind-resistant design by reducing the material volume while achieving the structural and aeroelastic safety and serviceability specifications (Cid Montoya et al., 2018b, 2021, 2022; Cid Montoya, 2024). Alternative frameworks were also developed by Jaouadi et al., 2020; Tinmitondé et al., 2022; Zheng et al., 2023. A commonality in all those reported studies, however, is the adoption of the QST-based formulation and assumptions of frequency independence, which confines the scope of shape design space strictly to streamlined deck cross-sections and neglects the dependency of the aeroelastic forces on the reduced velocity ($U^* = U/fB$). This last consideration gains importance when dealing with not-so-long spans, as the natural frequencies are higher and, consequently, the reduced velocities are low. According to Diana and Omarini, 2020, nonlinear frequency-dependent effects are relevant when the reduced velocity is lower than $U^* < 10 - 15$. The range of reduced velocities at which the QST holds

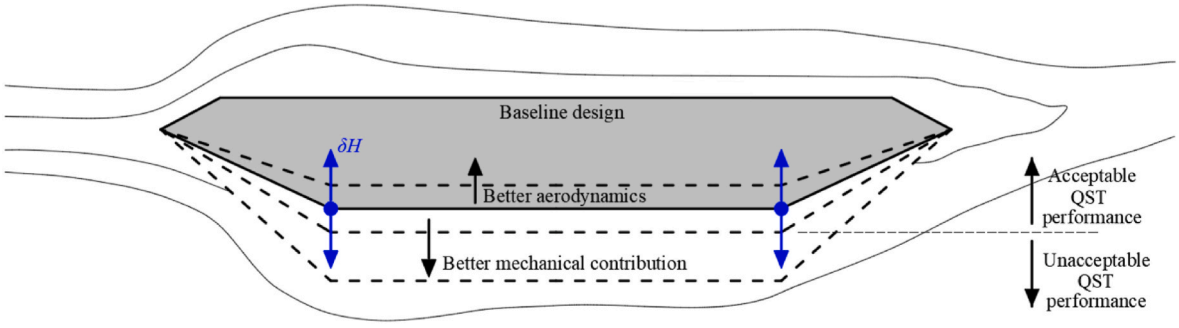

Fig. 1. Conceptual illustration of the typical contradictory aerodynamic and mechanical contributions of deck shape modifications to the bridge aeroelastic responses and the expected performance of the QST along classical shape design domains (based on Cid Montoya et al., 2018b).

depends on the specific deck cross-sections, and other studies suggest different ranges for the validity of the QST at low reduced velocities (see, for instance, Diana et al., 2013a, b; Calamelli et al., 2024). To overcome all the limitations posed by QST-based formulation within design frameworks, this study proposes a QST-free aeroelastic surrogate-based design methodology, which enables the exploration of a wide shape design space comprising of both streamlined and bluff deck sections of any deck typology and allows to account for the frequency-dependency of the aeroelastic loading.

The proposed QST-free aeroelastic surrogate-based design framework is described in Fig. 2 and comprises four key sequential modules that permit the construction of an aeroelastic emulator to be implemented in aero-structural design frameworks. The first step is the definition of the design variables and design parameters and their allowed range of variation. The variables defining the cross-sectional dimensions of the bridge that impact the aeroelastic response of the bridge, such as the chord width, depth, fairing angle, etc., qualify under shape design variables S_d, whereas the aeroelastic parameters, such as the reduced frequency/velocity, fall under design parameters. While the distinction between the shape design variables (derived from the deck cross-section definition) and the design parameters (derived from aeroelasticity, i.e., oscillation frequency or wind velocity) may not be very distinct from a purely mathematical standpoint in the surrogate training process, in a truly physical and functionality sense, however, the variables that can be controlled by the designer and/or is based on designer's will qualifies under design variables, whereas the design parameters encompass those that are not generally controlled by the designer and rather represents the different instances/possibilities exhibiting the dynamic interaction of bridge deck with winds with variability in phase lead/lag relation with the structural motion. Hence, the set of shape design variables composes the design domain, while the set of aeroelastic parameters originates the aeroelastic parametric domain. Therefore, the aeroelastic emulator will be defined within a "surrogate domain" that comprises the union of the design and parametric domains. From a designer's perspective, it would be compelling to define a large number of design variables to achieve better designs; however, as the problem's dimensionality rises, so does the associated computational cost due to the so-called 'curse of dimensionality' (Forrester et al., 2008). With the same motivation and a view to minimize the computational burden, two variables are chosen in this work: one shape design variable, which is the deck depth (H) because of its ability to tailor the deck ranging from streamlined to bluff geometries, hence $S_d = H$, and one aeroelastic design parameter, which is the reduced velocity (U^*). Hence, the surrogate domain is $\mathscr{D}_s = [S_d, U^*]$. It is worth mentioning that the elimination of the QST applicability requirements enables the definition of wider design domains only limited by engineering criteria and computational resources.

Once the design variables and parameters are identified and their ranges are defined, the next step is to create an adequate sampling plan that permits the effective exploration of the surrogate domain previously defined. The sampling plan must be designed to seek an effective domain exploration considering the particularities of the selected surrogate domain, such as eventual nonlinear aeroelastic behaviors. Further details are discussed in Sections 2.3 and 4.1.2. The next step in the sequential process is to conduct dynamic CFD simulations to quantify the aeroelastic response or fluid-structure parameters of interest as a function of design variables and parameters at discrete observation points. While the aeroelastic response of streamlined deck bridges can be assessed with reasonable accuracy using only eight flutter derivatives, i.e., the lift and moment flutter derivatives $A_i^*, H_i^*, i = 1, \ldots,4$, the aeroelastic responses of bluff deck bridges are impacted by the drag flutter derivatives P_i^*, as demonstrated in the analysis of some specific bridges, such as the Akashi Kaikyo Bridge (Miyata et al., 1995) and the Lions Gate Bridge (Jones et al., 2003), and in other research studies (Singh et al., 1996; Chowdhury and Sarkar, 2003; Xu et al., 2016). Hence, it is pivotal to emulate the full set of flutter derivatives to properly model all aeroelastic effects in a design domain comprising streamlined and bluff deck cross-sections. The CFD simulations required to extract the 18 flutter derivatives throughout the forced vibration technique can be carried out either in an uncoupled manner (one DoF imposed at a time as considered in the current work or in Mannini et al., 2016; Wang and Chen, 2022) or in a coupled manner (all the 3 DoFs imposed at once as in Xu et al., 2014) at the discrete points defined in the sampling plan. From the CFD simulations, the time history of aeroelastic forces is obtained, to which either the Fast Fourier Transform (FFT) (Mannini et al., 2016) or the least squares method (Xu et al., 2014) can be applied to obtain the aeroelastic flutter derivatives. Since the proposed numerical design methodology intends to advance current design methods well established in the engineering practice, the boundary conditions enforced on the CFD model should reflect the wind tunnel testing conditions commonly adopted in the industry, and a representative subset of numerical results must be validated against experimental measurements. Two levels of experimental validation for the CFD results should be conducted in the context of the proposed QST-free methodology: (1) time-averaged force coefficients and Strouhal numbers as a function of the angle of attack obtained throughout static CFD simulations and (2) time-variant aeroelastic force coefficients and integrated values of the flutter derivatives as a function of the reduced velocity obtained by dynamic CFD simulations. This is a fundamental part of the proposed methodology that advances previous frameworks based on the QST that only required static CFD simulations. Following the aeroelastic evaluations carried out by the CFD simulations, the next step is to train the surrogate model to build an aeroelastic emulator, which comprises a smooth response surface of flutter derivatives satisfying the design requirements of differentiability and continuity over the design space. From a mathematical black-box perspective, the QST-free aeroelastic emulator of the self-excited forces $\mathscr{A}_{se}$ can be formulated as:

$$\mathscr{A}_{se}(S_d, U^*) = \left[A_i^*, H_i^*, P_i^*\right] \tag{1}$$

Where the input is the surrogate domain $\mathscr{D}_s = [S_d, U^*]$ and the output is the complete set of 18 flutter derivatives A_i^*, H_i^*, P_i^*, where $i = 1, \ldots,6$, at angle of attack $\alpha = 0°$. From the obtained response surfaces, either the values of flutter derivatives can be used for design purposes adopting

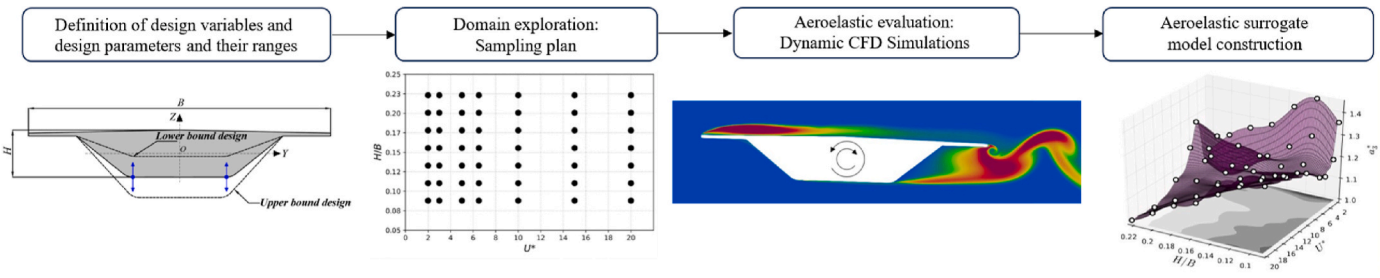

Fig. 2. Proposed framework for creating a design-oriented QST-free aeroelastic emulator.

traditional heuristic design approaches, or alternately, the surrogate may be employed in the surrogate-based design optimization (SBDO) process to obtain an optimal bridge deck shape design.

2.1. Aerodynamic and aeroelastic formulations

2.1.1. Aerodynamic force coefficients and Strouhal number

The aerodynamic force coefficients are the result of the integration of the time-averaged pressures distribution and viscous stresses along the deck perimeter caused by a constant wind without fluctuations on a bridge deck that is assumed to be rigidly supported. The aerodynamic steady forces are usually expressed in non-dimensional form (normalized by the dynamic pressure $\frac{1}{2}\ \rho U^2$ and a representative dimension of the deck) and are given by the expressions in Eq. (2). The Strouhal number, which depends on the frequency of vortex shedding is calculated by the expression for S_t in Eq. (2) below.

$$C_D = \frac{D}{\frac{1}{2}\ \rho U^2\ B},\quad C_L = \frac{L}{\frac{1}{2}\ \rho U^2\ B},\quad C_M = \frac{M}{\frac{1}{2}\ \rho U^2\ B^2},\quad S_t = \frac{f_{vs}\ H}{U} \tag{2}$$

In Eq. (2), D and L are the drag and lift forces, respectively, whereas M is the torsional moment acting on a unit of span length of the deck at a particular angle of attack. Similarly, ρ represents the density of air, U stands for the free-stream flow velocity and f_{vs} is the vortex shedding frequency in Eq. (2). The chord width of the bridge deck is represented by B whereas the depth of deck is represented by H. The sign convention adopted for evaluating static aerodynamic force coefficients is shown in Fig. 3.

2.1.2. Self-excited forces

Dynamically flexible medium- and long-span bridges oscillate under the wind action and the structural motion of these structures in turn induces aeroelastic forces on them, which are also called the motion-induced or the self-excited forces. The self-excited forces acting on a wind-sensitive structural system are usually expressed in the form of aeroelastic coefficients called the aerodynamic flutter derivatives, which are a set of nondimensional unsteady parameters that establish the relationships between the self-excited forces and the deck displacements. The flutter derivatives can be expressed in different notations such as the most popular Scanlan notation (Scanlan and Tomko, 1971), PoliMi (Politecnico di Milano) notation (Zasso, 1996), Küssner notation (Szechenyi, 1973), quasi-steady modified notation (Zasso, 1996), etc. In the present work, the Scanlan notation and the PoliMi notation, which provides a better resolution of flutter derivatives in the lower reduced velocity range, are used, and discussed below.

(a) Scanlan Notation:

The aeroelastic self-excited forces induced on the deck section under the wind action can be evaluated using the semi-empirical approach proposed by Scanlan and Tomko, 1971. In this approach, the aeroelastic forces on the deck section are related with the deck motion components (displacements and rotations) via a first order linear approximation, which can also be realized using a Taylor series expansion of aerodynamic forces around the respective motion component under consideration retaining the first order derivative while neglecting the higher order derivative terms from the Taylor series. Two degrees of freedom (corresponding to 'pitch' and 'heave') were considered in the original formulation proposed by Scanlan and Tomko, 1971. Later, the same formulation was extended to determine all the 18 flutter derivatives by incorporating the third degree of freedom based on horizontal oscillations of the deck section (Singh et al., 1996; Jain et al., 1996). Based on the same formulation, the self-excited forces are given by Eq. (3).

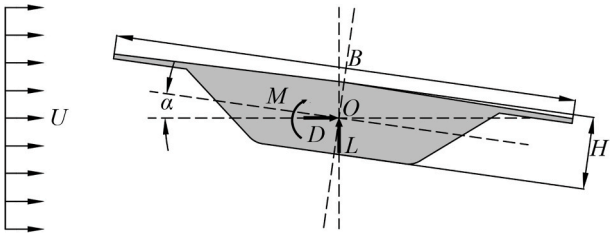

Fig. 3. Sign convention adopted for the force coefficients.

$$L_{se} = \frac{1}{2}\rho U^2 B\left[K_h H_1^* \frac{\dot{h}}{U} + K_\alpha H_2^* \frac{B\dot{\alpha}}{U} + K_\alpha^2 H_3^* \alpha + K_h^2 H_4^* \frac{h}{B} + K_p H_5^* \frac{\dot{p}}{B} + K_p^2 H_6^* \frac{p}{B}\right] \tag{3a}$$

$$D_{se} = \frac{1}{2}\rho U^2 B\left[K_p P_1^* \frac{\dot{p}}{U} + K_\alpha P_2^* \frac{B\dot{\alpha}}{U} + K_\alpha^2 P_3^* \alpha + K_p^2 P_4^* \frac{p}{B} + K_h P_5^* \frac{\dot{h}}{B} + K_h^2 P_6^* \frac{h}{B}\right] \tag{3b}$$

$$M_{se} = \frac{1}{2}\rho U^2 B^2\left[K_h A_1^* \frac{\dot{h}}{U} + K_\alpha A_2^* \frac{B\dot{\alpha}}{U} + K_\alpha^2 A_3^* \alpha + K_h^2 A_4^* \frac{h}{B} + K_p A_5^* \frac{\dot{p}}{B} + K_p^2 A_6^* \frac{p}{B}\right] \tag{3c}$$

In Eq. (3), the self-excited lift and drag force per unit length of span are represented by L_{se} and D_{se} whereas the aeroelastic moment per unit span length is represented by M_{se}. Similarly, K_h, K_α and K_p represent the reduced frequency of oscillation corresponding to heave (h), pitch (α), and shove (p) degrees of freedom, which are defined by $K_h = 2\pi/\ U^*$, $K_\alpha = 2\pi/\ U^*$, $K_p = 2\pi/\ U^*$, respectively, where U^* is the reduced velocity associated with respective degrees of freedom. The reduced velocity U^* is defined as $U^* = 2\pi U/\ \omega_x\ B$, where $x = h,\ \alpha,\ p,$ denote the respective motion components, and ω_x denotes the circular frequency associated with the motion. Similarly, $\dot{h}$, $\dot{\alpha}$ and $\dot{p}$, are the first order derivatives with respect to time for the heave, pitch, and shove motion components respectively. Finally, H_i^*, A_i^* and P_i^* ($i = 1, 2, \ldots 6$) are the flutter derivative values computed from the time history of aeroelastic forces. The sign convention adopted for the aeroelastic forces and different degrees of freedom for the dynamical system is shown in Fig. 4.

(b) PoliMi Notation:

The PoliMi notation for representing the flutter derivatives proposed by Zasso, 1996 has some salient features and adds to the advantage from other notations. This notation allows a quantitative comparison of aerodynamic forces on the deck cross-section from the coefficient values with no normalization factors and maintains the representation with same intrinsic resolution at high and low reduced velocities (Zasso, 1996). The loss of resolution in the lower reduced velocity range for flutter derivatives A_2^*, A_3^*, H_2^*, H_3^* is commonly encountered in Scanlan representation of flutter derivatives. However, when flutter derivatives are expressed in PoliMi notation, distinct non-linear trends of flutter derivatives as a function of reduced velocity can be observed. In addition, the flutter derivatives expressed in PoliMi notation converge towards that obtained from the QST exhibiting asymptotic trends approaching a limiting value at higher reduced velocity range (more distinctly observed for streamlined sections). The manifestation of such a tendency serves as an additional verification for the computed flutter derivatives using CFD simulations. Hence, the advantages offered by the PoliMi notation are also utilized in this work while formulating the sampling plan and training the surrogate model. In the PoliMi notation, the self-excited forces are given by Eq. (4), where $U_\omega^* = \frac{U^*}{2\pi}$.

$$L_{se} = \frac{1}{2}\rho U^2 B\left[-h_1^* \frac{\dot{h}}{U} - h_2^* \frac{B\dot{\alpha}}{U} + h_3^* \alpha + h_4^* \frac{\pi}{2\ U_\omega^{*2}} \frac{h}{B} - h_5^* \frac{\dot{p}}{U} + h_6^* \frac{\pi}{2\ U_\omega^{*2}} \frac{p}{B}\right] \tag{4a}$$

$$D_{se} = \frac{1}{2}\rho U^2 B\left[-p_1^* \frac{\dot{h}}{U} - p_2^* \frac{B\dot{\alpha}}{U} + p_3^* \alpha + p_4^* \frac{\pi}{2\ U_\omega^{*2}} \frac{h}{B} - p_5^* \frac{\dot{p}}{B} + p_6^* \frac{\pi}{2\ U_\omega^{*2}} \frac{p}{B}\right] \tag{4b}$$

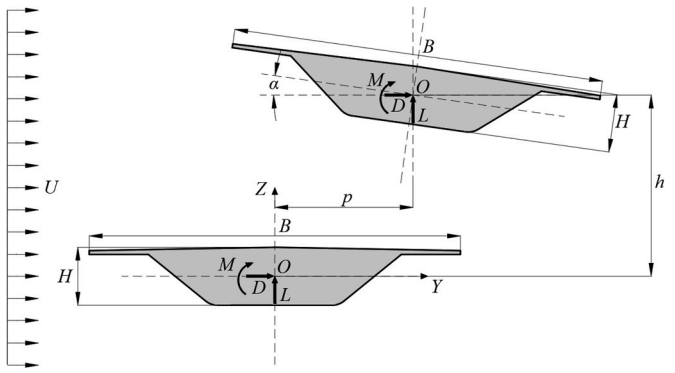

Fig. 4. Sign convention adopted for the aeroelastic forces and motion components.

$$M_{se}=\frac{1}{2}\rho U^2B^2\left[-a_1^*\frac{\dot{h}}{U}-a_2^*\frac{B\dot{\alpha}}{U}+a_3^*\alpha+a_4^*\frac{\pi}{2}\frac{h}{U_\omega^{*2}B}-a_5^*\frac{\dot{p}}{B}+a_6^*\frac{\pi}{2}\frac{p}{U_\omega^{*2}B}\right] \quad (4c)$$

As both the notations are used in different sections of the current work, the conversion relation between the flutter derivatives expressed in the Scanlan notation to the PoliMi notation and vice-versa are also included and are given by Eq. (5) below.

$$H_1^*=-\frac{U^*}{2\pi}h_1^*;\quad H_2^*=-\frac{U^*}{2\pi}h_2^*;\quad H_3^*=\left(\frac{U^*}{2\pi}\right)^2h_3^* \quad (5a)$$

$$H_4^*=\frac{\pi}{2}h_4^*;\quad H_5^*=-\frac{U^*}{2\pi}h_5^*;\quad H_6^*=\frac{\pi}{2}h_6^* \quad (5b)$$

$$A_1^*=-\frac{U^*}{2\pi}a_1^*;\quad A_2^*=-\frac{U^*}{2\pi}a_2^*;\quad A_3^*=\left(\frac{U^*}{2\pi}\right)^2a_3^* \quad (5c)$$

$$A_4^*=\frac{\pi}{2}a_4^*;\quad A_5^*=-\frac{U^*}{2\pi}a_5^*;\quad A_6^*=\frac{\pi}{2}a_6^* \quad (5d)$$

$$P_1^*=-\frac{U^*}{2\pi}p_5^*;\quad P_2^*=-\frac{U^*}{2\pi}p_2^*;\quad P_3^*=\left(\frac{U^*}{2\pi}\right)^2p_3^* \quad (5e)$$

$$P_4^*=\frac{\pi}{2}p_6^*;\quad P_5^*=-\frac{U^*}{2\pi}p_1^*;\quad P_6^*=\frac{\pi}{2}p_4^* \quad (5f)$$

The key difference between the two notations is that the flutter derivatives P_1* and P_4* refer to the lateral velocity/displacement whereas p_5* and p_6* refer to the same in PoliMi notation. Similarly, P_5* and P_6* refer to the vertical velocity/displacement in Scanlan notation whereas p_1* and p_4* refer to the same in PoliMi notation.

(c) Quasi-Steady Theory (QST) formulation:

The quasi-steady theory (Scanlan, 1988) is a modeling scheme for wind-induced loads in which the interaction of flow with the bridge at the current time instant is mapped to the state at infinite time neglecting the wake effect on the downstream end of the deck (Wu and Kareem, 2013). A more in-depth discussion of the quasi-steady theory can be found in Tubino (2005). To perform a standard frequency domain analysis, the quasi-steady load model is linearized (Salvatori and Spinelli, 2007; Lazzari, 2005), which upon further simplification and comparison with Scanlan's semi-empirical relations yields a relationship connecting the flutter derivatives with mean aerostatic force coefficients and their slopes. The flutter derivatives based on QST model are given by Eq. (6), where $K=\frac{2\pi}{U^*}$ is the reduced frequency of oscillation.

$$H_1^*=-\frac{C'_{L,0^\circ}+C_{D,0^\circ}}{K};\ H_2^*=-\frac{C'_{L,0^\circ}+C_{D,0^\circ}}{K}\mu_H;\ H_3^*=-\frac{C'_{L,0^\circ}}{K^2};\ H_5^*=-\frac{2C_{L,0^\circ}}{K};$$
$$A_1^*=\frac{C'_{M,0^\circ}}{K};\quad A_2^*=\frac{C'_{M,0^\circ}}{K}\mu_A;\quad A_3^*=\frac{C'_{M,0^\circ}}{K^2};\quad A_5^*=-\frac{2C_{M,0^\circ}}{K};$$
$$P_1^*=-\frac{2C_{D,0^\circ}}{K};\quad P_2^*=-\frac{C'_{D,0^\circ}-C_{L,0^\circ}}{K}\mu_P;\ P_3^*=\frac{C'_{D,0^\circ}}{K^2};\quad P_5^*=\frac{C'_{D,0^\circ}-C_{L,0^\circ}}{K}; \quad (6)$$

Similarly, $C_{D,0^\circ}$, $C_{L,0^\circ}$ and $C_{M,0^\circ}$ are the mean drag, lift and moment coefficients respectively at 0° angle of attack whereas $C'_{D,0^\circ}$, $C'_{L,0^\circ}$ and $C'_{M,0^\circ}$ are the slopes of the mean drag, lift, and moment coefficients respectively. The coefficients μ_A,μ_H,μ_P are the aerodynamic centers, which represent the distance between the elastic center of the cross section and the distances between the point of application of the aerodynamic forces expressed as a fraction of the section width B and are defined by $\mu_A=A_3^*/H_3^*$,$\mu_H=A_1^*/H_1^*$,$\mu_P=\mu_H$ (Chen and Kareem, 2002). Alternately, Diana et al. (1993) have proposed that the aerodynamic centers can be determined from the ratio of flutter derivatives defined by $\mu_A=A_2^*/A_1^*$, $\mu_H=-H_2^*/H_1^*$, $\mu_P=P_2^*/P_1^*$, obtained from the wind tunnel tests at the highest reduced velocity where the QST holds true. However, as no information exists about the flutter derivatives beforehand in the frame of standalone application of QS formulation, so, in this work, the aerodynamic centers inferred from the QS approximation of the flutter derivatives A_1^*, H_1^*, A_3^* and H_3^* as proposed by Larose and Livesey (1997) is used to determine the aerodynamic centers. The remaining flutter derivatives such as the H_i*, A_i* and P_i* (i = 4, 6) are 0 in the QST formulation. The application of QST-based formulation in the case of streamlined decks can be found in Larose and Livesey, 1997; Borri and Costa, 2004; Febo and D'Asdia, 2010; Cid Montoya et al., 2020.

2.1.3. Buffeting forces

The buffeting wind loads per unit length of bridge, due to the turbulent velocity fluctuations, defined by $u=u_oe^{i2\pi f^*t^*}$ and $w=w_oe^{i2\pi f^*t^*}$, (Diana et al., 2020a) is given by Eq. (7), where u and w are the turbulent fluctuations at a given time instant whereas u_o and w_o are the amplitudes of the harmonic fluctuation components in the horizontal and vertical directions respectively.

$$D_b=\frac{1}{2}\rho U^2B\left(\chi_{Du}^*\frac{u}{U}+\chi_{Dw}^*\frac{w}{U}\right), \quad (7a)$$

$$L_b=\frac{1}{2}\rho U^2B\left(\chi_{Lu}^*\frac{u}{U}+\chi_{Lw}^*\frac{w}{U}\right), \quad (7b)$$

$$M_b=\frac{1}{2}\rho U^2B^2\left(\chi_{Mu}^*\frac{u}{U}+\chi_{Mw}^*\frac{w}{U}\right), \quad (7c)$$

Similarly, χ_{Du}^*, χ_{Dw}^*, χ_{Lu}^*, χ_{Lw}^*, χ_{Mu}^*, χ_{Mw}^* are the aerodynamic admittance functions, which are a function of the deck cross-section and can be determined through experimental measurement or numerical simulations. Further details about buffeting analysis and determination of aerodynamic admittance functions can be obtained from Larose, 1999; Zasso et al., 2013; Diana et al., 2013a, b.

The goal of this work is to model the nonlinear behavior of the self-excited forces with a focus on the low reduced velocities. In order to simplify the interpretation of the results, the admittance functions will be calculated using the Davenport admittance (Davenport, 1963), hence avoiding the nonlinearities coming from the buffeting loads part. This approach was also used in the activities of the IABSE Task Group 3.1. (Diana et al., 2020a, 2020b). Hence, the admittance functions will be calculated as per Eq. (8), where $A(f^*)$ is the davenport admittance (Davenport, 1963). A decay factor of 7 is used to be on the conservative side when performing the buffeting-resistance deck shape tailoring.

$$\begin{aligned}
\chi^{*}_{Du} &= 2.C_{D,0^\circ}.A(f^{*}), \quad \chi^{*}_{Dw} = \left(C^{'}_{D,0^\circ} - C_{L,0^\circ}\right).A(f^{*}),\\
\chi^{*}_{Lu} &= 2.C_{L,0^\circ}.A(f^{*}), \quad \chi^{*}_{Lw} = \left(C^{'}_{L,0^\circ} + C_{D,0^\circ}\right).A(f^{*}),\\
\chi^{*}_{Mu} &= 2.C_{M,0^\circ}.A(f^{*}), \quad \chi^{*}_{Mw} = C^{'}_{M,0^\circ}.A(f^{*})
\end{aligned} \tag{8}$$

2.2. CFD modeling formulation

2.2.1. Static simulation

Flow around the bridge deck is modeled by incompressible Unsteady Reynolds Averaged Navier-Stokes (URANS) equations with k-ω SST turbulence model (Mannini et al., 2010, 2016; Fransos and Bruno, 2010; Brusiani et al., 2013; Álvarez et al., 2018). A 2D flow is considered in a rectangular domain inside of which the deck of bridge is modeled.

The governing fluid flow equations are given by Eqs. (9) and (10) for the static case (stationary deck section).

$$\frac{\partial U_i}{\partial x_i} = 0 \tag{9}$$

$$\rho\frac{\partial U_i}{\partial t} + \rho U_j\frac{\partial U_i}{\partial x_j} = -\frac{\partial P}{\partial x_i} + \frac{\partial}{\partial x_j}\left[\mu\left(\frac{\partial U_i}{\partial x_j} + \frac{\partial U_j}{\partial x_i}\right) - \rho\,\overline{u_i^{'}u_j^{'}}\right] \tag{10}$$

In Eqs. (9) and (10), U_i is the mean velocity of flow, P is the mean pressure, μ is the molecular dynamic viscosity of fluid, $u^{'}$ is the fluctuating component of velocity, S_{ij} is the mean strain rate tensor and x_i represents the spatial coordinates of the fluid domain in 2D cartesian frame. In the URANS approach, the averaging operator defined in Eq. (11) is applied on the Navier-Stokes (NS) equation, which represents the average of many statistically identical realizations of flow variables at a certain time (Ferziger and Peric, 1996).

$$\varphi(x,t) = \lim_{N\to\infty}\frac{1}{N}\sum_{n=1}^{N}\varphi(x,t) \tag{11}$$

After applying the averaging operator on the NS equation, some additional terms appear due to the non-linearity of convection term in NS equation leading to the classical closure problem. The residual term $-\rho\overline{u_i^{'}u_j^{'}}$ obtained after the averaging procedure is called the Reynolds stress tensor, which is equated to the mean velocity gradient using the classic Boussinesq hypothesis to close the system of equation. After some mathematical simplification and substitutions, the specific Reynold's stress tensor is obtained as follows:

$$\tau^{'}_{ij} = 2\vartheta_t \,.\, S_{ij} - \frac{2}{3}k\delta_{ij} \tag{12}$$

For incompressible flow, the second term in Eq. (12) is usually combined with the pressure gradient term of NS equation resulting in a turbulent pressure field, i.e., $p \leftarrow p + \left(\frac{2}{3}k\right)$; here, $p = P/\rho$ is the kinematic pressure field. The only remaining unknown in the system of equation is the turbulent kinematic viscosity ϑ_t which is obtained by solving the transport equation of k and ω. The details about the k-ω *SST* turbulence model along with all the model coefficients used in the transport equations can be obtained from Menter et al., 2003.

2.2.2. Dynamic simulation

For the determination of self-excited forces to compute the flutter derivatives, forced harmonic oscillations are imposed on the deck section using the Arbitrary Lagrangian Eulerian (ALE) formulation (Donea et al., 2004). The imposed motion for pitching, heaving, and shoving are applied by $\alpha = \alpha_o \sin(\omega t)$, $h = h_o \sin(\omega t)$, and $p = p_o \sin(\omega t)$ respectively. The amplitudes of the imposed motions α_o, h_o, and p_o are selected by mimicking the common engineering practice for extracting the flutter derivatives. The flutter derivatives dependency on the vibration amplitude, which is important to accurately predict VIV responses (Wang and Chen, 2022), is not addressed in this investigation. In this work, only one degree of freedom (DoF), i.e., either 'pitch', 'heave', or 'shove' DoF is imposed at a time as shown in Fig. 5. For imposing the motion, the mesh of the domain is adjusted in each time-step by moving the boundaries of the deck section. The conservation of mass and momentum for the motion-imposed deck system is given by Eqs. (13) and (14), where U_{gi} is the grid velocity in the ith direction.

$$\frac{\partial\left(U_i - U_{gi}\right)}{\partial x_i} = 0 \tag{13}$$

$$\rho\frac{\partial U_i}{\partial t} + \rho U_j\frac{\partial\left(U_i - U_{gi}\right)}{\partial x_j} = -\frac{\partial P}{\partial x_j} + \frac{\partial}{\partial x_j}\left(2\mu S_{ij} - \rho\overline{u_i^{'}u_j^{'}}\right) \tag{14}$$

The mesh motion is implemented using a second-order quasi-tetrahedral Finite Element method (Jasak and Tuković, 2007). The governing equation for mesh motion is given by Eq. (15), in which the Laplace equation for mesh node displacement vector (u) is solved with a variable diffusivity (γ).

$$\nabla.(\gamma\nabla u) = 0 \tag{15}$$

The variable diffusivity is computed using the quadratic inverse distance method, in which the amplitude of imposed motion at the oscillating boundary gets diffused to the rest of the domain following an inverse proportionality relation on the square of the distance of a cell from the moving boundary. After obtaining the time history of aeroelastic forces, the values of flutter derivatives are computed using the method of least squares (Xu et al., 2014).

2.3. Surrogate modeling

In engineering design problems, often, a situation is encountered in which it is difficult to ascertain the exact functional dependence of the key response variables of interest subject to a given input and/or a set of input variables. Due to the inherent complexity involved in the physical process (either experiment or numerical simulation), a set of discrete observations and samples often becomes the only alternative to explore and gain valuable insights into the functional dependence between the variables in certain cases (Forrester et al., 2008). Applying the same philosophy to bridge aeroelasticity, the aerodynamic/aeroelastic responses subject to either the changes in the flow/aerodynamic conditions and/or the structural parameters (such as due to the different shapes, sizes, structural properties, etc.) would require an enormously large set of experiments or numerical simulations to be carried out as the relationship between the aeroelastic response of bridge deck subject to several aerodynamic and structural constraints usually exhibits highly non-linear relationships. In such a scenario, a surrogate model (which is an approximating function to the real function describing the relationship between the response variable and the design variables/-parameters) becomes an easy-to-evaluate and computationally efficient alternative to a plethora of physical/computational experiments.

The fundamental requirement for implementing surrogate models in design frameworks based on gradient-based optimization algorithms is that the response surface describing the relationship between the response variable (aerodynamic/aeroelastic response within the current scope of work) and the design variables/parameters is continuous, smooth, and differentiable over the design space. The next important consideration in surrogate modeling is the quality of the space exploration, which consists of the necessity to sample a high enough number of discrete observations of the response with an efficient distribution along the design domain that guarantees that the set of observations provides an accurate and sufficient representation of the real response in the design domain for its intended use. For that purpose, different sampling techniques are available such as the full-factorial sampling plan, Latin hypercube sampling plan, space-filling Latin Hypercube sampling plan, to name a few. Each of these techniques has its own strengths and drawbacks, as discussed in McKay et al. (1979), Sacks

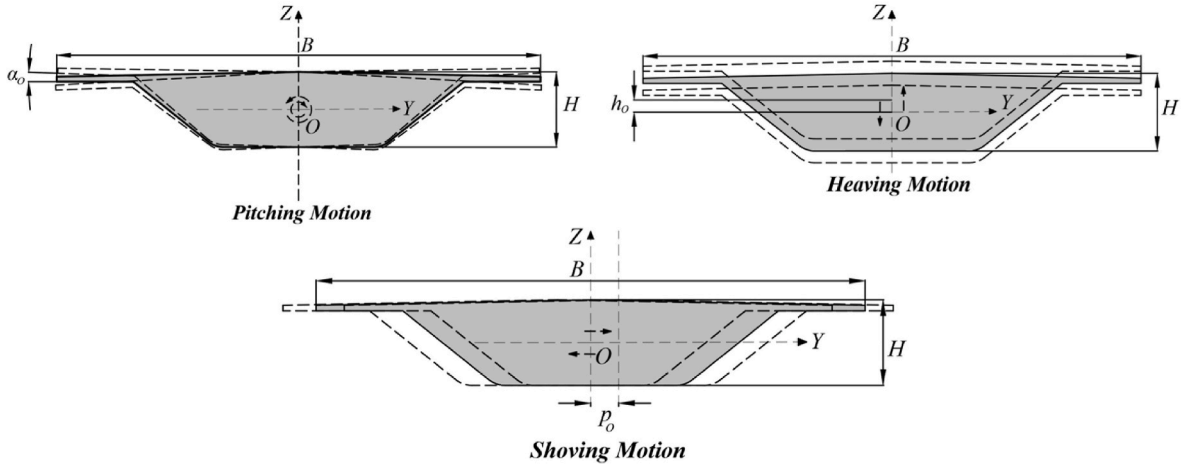

Fig. 5. Schematic representation of a deck cross-section subjected to forced vibration and oscillating in different (torsional, vertical, and lateral) vibration modes.

et al. (1989), Olsson et al. (2003), Picheny et al. (2010), and Yondo et al. (2018). For instance, the full factorial sampling plan provides a uniform level of accuracy throughout the design space with the uniformly spread point distribution on its input variable axes but results in the overlap of sample points when projected onto its constituent axes. The Latin hypercube sampling technique ensures a stratified distribution of sample points in each of the dimensions; however, it still might suffer the drawback of not fulfilling the space-filling criteria. The space filling Latin hypercube sampling could be an alternative to satisfy the space-filling criteria, but its computational complexity may rise very rapidly as the size of sampling plan (or the number of sampling points) increases. The choice of a specific sampling plan suited for a particular problem is generally an open issue. In the context of wind engineering problems, the computational extraction of fluid-structure interaction parameters is typically conditioned to its later interpretation and validation with wind tunnel tests, which requires comparisons changing only one variable, e.g., flutter derivatives as a function of the reduced velocity, while the other variables are unchanged (ceteris paribus). In this context, full factorial sampling stands as a very suitable alternative for engineering interpretation and systematic analysis (Cid Montoya et al., 2023). Further details about the full factorial sampling strategy adopted in this investigation are described in Section 3.3.

Once the dimensionality of the problem is ascertained (based on the number of design variables and design parameters) and an appropriate sampling plan has been worked out, the next step is to determine the responses (the output of the emulator, i.e., the flutter derivatives in the current scope of work) via dynamic CFD simulations. Once these responses are available for every design included in the sampling plan, the next step is to train the surrogate model. The Kriging surrogate model (Krige, 1951; Sacks et al., 1989), which is a popular choice in surrogate-based optimization problems, is chosen for this task as it guarantees that all the responses of the samples are contained in the response surface. This is a key advantage in problems where the computation of the responses for each sample has a high computational burden, as it is the case for dynamic CFD simulations. Previous applications in the bridge engineering field for emulating bridge deck force coefficients can be found in Cid Montoya et al., 2018a; Kusano et al., 2020; Nieto et al., 2020; Xu et al., 2020; Li et al., 2021. The kriging emulator $\widehat{f}_k(\mathbf{x})$ is made of a regression model or trend function $\boldsymbol{k}(\mathbf{x})^T\boldsymbol{\rho}$ and a stationary Gaussian process error model $\boldsymbol{\varepsilon}(\mathbf{x})$ that corrects the trend function:

$$\widehat{f}_k(\mathbf{x}) = \boldsymbol{k}(\mathbf{x})^T\boldsymbol{\rho} + \boldsymbol{\varepsilon}(\mathbf{x}) \tag{16}$$

Another key assumption in the Kriging model is that the observed responses are the realization of random variables from a stochastic process in which the random variables are correlated to each other through the basis function defined in Eq. (17).

$$cor\left[Y\left(\mathbf{x}^{(i)}\right), Y\left(\mathbf{x}^{(l)}\right)\right] = \psi^{(i)} = exp\left(-\sum_{j=1}^{k}\theta_j\left|x_j^{(i)} - x_j\right|^{p_j}\right) \tag{17}$$

In Eq. (17), k is the number of design variables, the vector $\mathbf{x}^{(i)}$ is the i^{th} sample and $Y\left(\mathbf{x}^{(i)}\right)$ is the observed response of the i^{th} sample. Similarly, $\left|x_j^{(i)} - x_j\right|^{p_j}$ is the absolute distance between sample points, and θ_j and p_j are model parameters obtained maximizing the likelihood of the vector of observed data $\mathbf{y}$. Further details about the Kriging surrogate model can be obtained from Forrester et al., 2008.

2.4. Buffeting analysis

Buffeting is commonly a governing load in the wind-resistant design of bridges. Depending on the characteristics of the incoming flow in terms of the magnitude of the variations of the mean velocity and angle of attack as a function of time, different modeling approaches can be implemented, ranging from linear frequency domain methods (Cheynet et al., 2016; Diana et al., 2020b; Cid Montoya et al., 2020) to nonlinear time-domain methods (Chen and Kareem, 2002; Diana et al., 2010; Diana and Omarini, 2020; Barni et al., 2022). In this study, a synoptic wind scenario is used for analyzing the impact of deck shape modifications on the bridge's self-excited forces and its impact on the buffeting response. In this context, a linear frequency domain analysis is sufficient to obtain an accurate response (Diana et al., 2023).

2.4.1. Multi-mode buffeting response

Under the action of turbulent winds, the bridge is subjected to three main wind-induced forces, viz. (a) mean aerodynamic forces on the deck submerged in the flow (b) self-excited forces due to the structural motion and (c) buffeting forces due to the turbulent velocity fluctuations. The mean aerodynamic forces acting on the deck are defined in Eq. (2), whereas the aeroelastic forces are given by Eq. (3). Since the RMS of the accelerations of the bridge deck is considered for buffeting response evaluation, the effect of mean aerodynamic forces can be neglected, and the equation of motion can be written as:

$$\mathbf{M}\ddot{\mathbf{u}} + (\mathbf{C} - \mathbf{C}_{\mathbf{se}})\dot{\mathbf{u}} + (\mathbf{K} - \mathbf{K}_{\mathbf{se}})\mathbf{u} = \mathbf{f}^{\mathbf{b}} \tag{18}$$

Either the frequency domain or the time domain buffeting analysis (Strømmen, 2010; Caracoglia and Jones, 2003; Diana et al., 2023) can be adopted for multi-mode buffeting response evaluation. However, frequency domain analysis is relatively more efficient compared to time domain analysis from a computational perspective, which makes it very

suitable for design purposes when dealing with synoptic winds.

2.4.2. Frequency domain buffeting analysis

The buffeting response of a bridge deck, when expressed in physical coordinates S_r, as the matrix of power spectral density (PSD) of the displacements is given by:

$$\mathbf{S_r} = \mathbf{\Phi H \Phi^T S_b \Phi H^{*T} \Phi^T} \tag{19}$$

In Eq. (19), $\mathbf{\Phi}$ is the modal matrix normalized to the mass, $\mathbf{H}$ is the impedance matrix of the system at a given frequency and $\mathbf{S_b}$ is the matrix of PSDs of the buffeting forces. The matrix $\mathbf{S_b}$ is defined by:

$$\mathbf{S}_b(f^*) = \boldsymbol{\chi}_A^*(V^*)\, \boldsymbol{S}_{wind}(f^*)\, \boldsymbol{\chi}_A^{*T}(V^*) = \left(\frac{1}{2}\rho U B l_e\right)^2 \cdot \begin{vmatrix} \chi_{Du}^* & \chi_{Dw}^* \\ \chi_{Lu}^* & \chi_{Lw}^* \\ B\chi_{Mu}^* & B\chi_{Mw}^* \end{vmatrix} \cdot \begin{vmatrix} S_{uu} & S_{uw} \\ S_{uw} & S_{ww} \end{vmatrix} \cdot \begin{vmatrix} \chi_{Du}^* & \chi_{Lu}^* & B\chi_{Mu}^* \\ \chi_{Dw}^* & \chi_{Lw}^* & B\chi_{Mw}^* \end{vmatrix} \tag{20}$$

In Eq. (20), $\boldsymbol{\chi}_A^*$ represent the admittance functions, $\boldsymbol{S}_{wind}(f^*)$ is the cross-power spectrum matrix of the incoming turbulence whereas S_{uu}, S_{vv}, S_{ww} and S_{uw} are the different components of the wind spectrum that is multiplied by the space coherence function (Davenport, 1967). The root mean square (RMS) of the buffeting responses given by $r_{RMS} = [u_{RMS}, w_{RMS}, \theta_{RMS}]$, which are the RMS of lateral, vertical, and torsional displacements and the RMS of accelerations $\ddot{r}_{RMS} = \left[\ddot{u}_{RMS}, \ddot{v}_{RMS}, \ddot{\theta}_{RMS}\right]$, are obtained from the PSD matrix of displacements $\mathbf{S_r}$ for each node of the deck and wind velocity and are given by:

$$r_{RMS} = \sqrt{\int_0^\infty S_r df} \text{ and } \ddot{r}_{RMS} = \sqrt{\int_0^\infty 16\pi^4 f^4 S_r df} \tag{21}$$

Further details about the procedure of frequency domain buffeting analysis can be obtained from Hui et al., 2005; Zhu and Xu (2005); Diana et al., 2020a; Diana et al., 2020b, and the references cited therein.

3. Application case

3.1. Baseline geometry

The reference geometrical cross-section considered in this work is inspired by the Sunshine Skyway bridge in Florida (Shahawy and Arockiasamy, 1996a, 1996b). Due to the popularity and ubiquity of this type of section in medium-span bridges in different parts of the world, several studies have been carried out to develop a better understanding of the wind loading on this type of section. For instance, the peak vertical displacement of the Farø bridge (resembling the cross-section used in this work) obtained through full-scale monitoring showed good agreement with that predicted from the quasi-steady approach (Petersen et al., 1987). Similarly, the comparison of the mid-span deflection of the prototype Sunshine Skyway bridge showed a very good agreement when compared with the results obtained from section model tests and full bridge model tests (Davenport and King, 1982a, 1982b). Further details about the full-scale monitoring of bridges and comparison with experimental and analytical approaches can be obtained from Larose et al., 1992. In addition, the details of the sectional model tests and full aeroelastic model tests carried out for the Prospect Verona bridge (with similar cross-section) in Maine is well documented in King et al., 2005. All these studies highlight the importance of this type of cross-section in medium-span bridges, thus leading to the motivation for its selection as an application case in this work.

The baseline geometry comprises the single box deck as shown in Fig. 6. Although the selection of this deck section as the baseline geometry is inspired by the Sunshine Skyway bridge, it is worth pointing out that the bottom edge corners of the Sunshine Skyway bridge are made sharp using acrylic blocks whereas in the current work, a small radius of curvature ($R = 0.05B$) is provided. This is done to make the computational studies carried out in this work consistent with the experimental studies conducted in the experimental CRIACIV section at the Inter-university Research Center on Building Aerodynamics and Wind Engineering, Boundary Layer Wind Tunnel, Prato, Italy. During the fabrication process, a slight degree of roundness was introduced in the deck section bottom corners (marked by '*e*' and '*f*' in Fig. 6) due to the bending of aluminum sheets (Mannini et al., 2010). The degree of roundness (whether perfectly sharp or with a slight curvature) strongly influences the flow separation, attachment, and re-attachment points and subsequently the Strouhal number. Experimental tests carried out at the Western Ontario Wind Tunnel Laboratory, Canada (Davenport and King, 1982b ; Ricciardelli and Hangan, 2001) on similar deck section (but with sharp bottom corners) revealed positive lift force at zero degrees angle of attack (AoA) and demonstrated earlier stall whereas that from the experimental CRIACIV section (with a slight curvature) yielded negative lift force on the section at 0° AoA with a delayed stall. CFD studies carried out by Mannini et al., 2010; Fransos and Bruno, 2010 later confirmed that a small degree of curvature introduced at the bottom corners of the deck section makes a more realistic idealization of the actual CRIACIV section, thus leading to better agreement in the flow field and force coefficients. Since most of the validation aspects of the CFD model employed in this work is based on the experimental CRIACIV section and computational studies from Mannini et al., 2010; Fransos and Bruno, 2010; Mannini et al., 2016, a small radius of curvature ($R = 0.05B$) is introduced at the bottom corners in the baseline geometry as well as any other candidate design within the shape design domain adopted.

3.2. Surrogate domain: design and parametric domains

Aiming at avoiding the curse of dimensionality issues discussed in Section 2, a judicious choice of shape design variables and parameters is necessary while still ascertaining the required degree of accuracy to be achieved from the metamodel. Accordingly, two variables, viz. (a) depth of deck (H) and (b) reduced velocity (U^*) are chosen as shape design variable and aeroelastic parameter respectively, which makes the dimensionality of the surrogate modeling problem as 2. However, the methodology presented in this investigation can be extended by adding more shape design variables, such as the deck width (see, for instance, Cid Montoya, 2024), corner angles (Jiang et al., 2020), the position of appendages (Cid Montoya et al., 2023), and others, which may entail a higher computational burden to properly explore the design domain. The next step is the definition of the bounds of the surrogate domain $\mathscr{D}_s = [S_d, U^*]$ in which a set of discrete observations are taken to learn about the behavior of the responses.

The design domain is defined by setting lower and upper limits to the only shape design variable adopted, the deck depth H. As shown in Fig. 6, the profile of deck bounded by the letters '*a* - *k*' defines the shape of the baseline geometry with deck depth of $H_0 = 0.1556B$, where $B =$

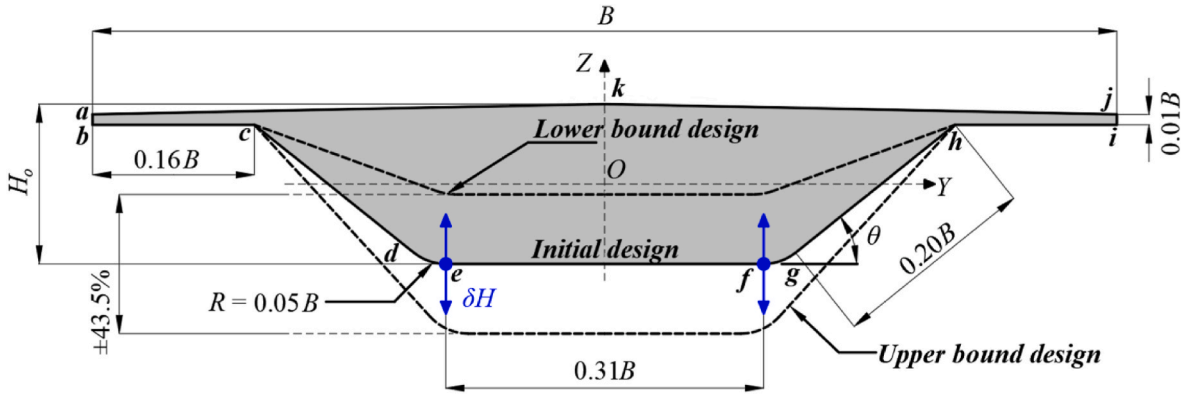

Fig. 6. Deck cross-section of the baseline geometry (gray) including the upper and the lower bounds of the selected shape design domain.

36 m, is considered in the current work. The baseline design, or initial design (H_0), corresponds to the deck cross-section geometry of the Sunshine Skyway Bridge, as previously discussed in Section 3.1. The lower bound and the upper bounds of the design domain with deck depths $H_{min} = 0.0879B$ and $H_{max} = 0.2232B$ respectively, are obtained by shifting the positions of '*e*' and '*f*' vertically upwards leading to more streamlined geometrical sections than the baseline geometry as well as downwards leading to relatively bluffer ones. This information is also reported in Table 1. It should be noted that the radius of curvature ($R = 0.05B$) is maintained for any candidate design within the shape design domain.

On the other hand, the parametric domain consists of setting upper and lower bounds to the reduced velocity U^*. The domain adopted is $U^* = [2.0, 20.0]$, seeking the reproduction of eventual nonlinear aeroelastic features at low reduced velocities, typically occurring for reduced velocities lower than 10 (Diana and Omarini, 2020), and also aiming at capturing the flutter derivative values at large reduced velocities, in order to cover the complete range usually required for aeroelastic analyses.

3.3. Domain exploration: sampling plan

Once the design domain is defined, the next step is to create a sampling plan to evaluate the responses of interest (18 aerodynamic flutter derivatives in the current scope of work) at discrete sample points residing in the *n*-dimensional surface/plane formed by the design variables/parameters, where *n* is the dimensionality of the problem. The classical full factorial sampling plan combined with some applied engineering judgement is adopted in this work. Engineering judgement is applied in the sense that the projection of sampling points on the *H/B*-axis is uniform in order to explore the entire design domain with a uniform sample density. However, the projection on the U^* axis is non-uniform with larger number of points (4) stacked towards the lower bound of reduced velocity range (*i.e.,* $2.0 \leq U^* \leq 10.0$) in order to capture eventual aerodynamic nonlinearities, while only 3 points are considered towards the upper bound ($10.0 \leq U^* \leq 20.0$), since it is expected that the flutter derivatives tend to exhibit an asymptotic behavior at large reduced velocities when represented as a function of U^* in PoliMi notation. Hence, the resulting samples for the reduced velocity are $U^* = [2.0, 3.0, 5.0, 6.5, 10.0, 15.0, 20.0]$. The sampling plan adopted is represented in the U^*-*H/B* plane as shown in Fig. 7. Table 1 reports some geometrical characteristics of the 7 shape designs adopted for the full factorial sampling plan, where $H_{model-scale}$ represents the dimensional properties of the CFD/experimental model deck section whereas the $H_{Sunshine\ Skyway\text{-}scale}$ represents the dimensional properties of the Sunshine Skyway bridge, δH is the relative variation in depth of deck with respect to that of the baseline geometry and θ is the corner angles (refer Fig. 6) of the geometry samples.

3.4. Numerical evaluation of the samples

The next step is to carry out dynamic CFD simulations for each of the sample points as defined in the sampling plan to obtain the time history of aeroelastic forces. After obtaining the time history, all the 18 flutter

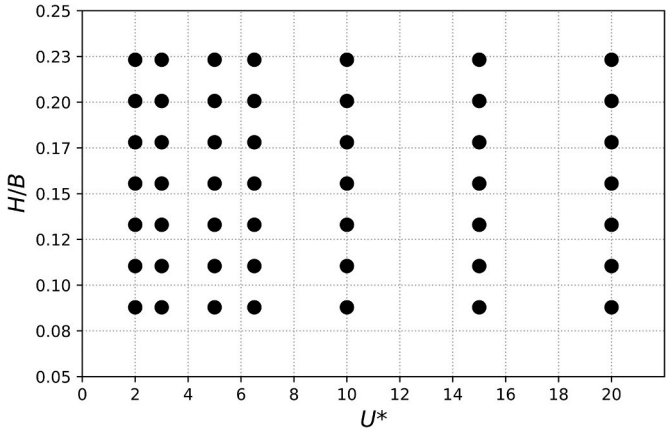

Fig. 7. Sampling plan over the surrogate domain in the U^*-*H/B* plane.

Table 1
Details of the deck depth (*H*) and corner angles (θ) for all the 7 shape designs included in the sampling plan, including the initial design (H_o), the lower bound design (H_{min}), and the upper bound design (H_{max}).

Design	*H/B*	$H_{model-scale}$ (m)	$H_{Sunshine\ Skyway\text{-}scale}$ (m)	δH (%)	θ (°)
1 (H_{min})	0.0879	0.03955	3.164	−43.50	21.78
2	0.1104	0.04970	3.976	−29.00	28.05
3	0.1330	0.05985	4.788	−14.50	33.66
4 (H_o)	0.1556	0.07000	5.600	0.00	38.63
5	0.1781	0.08015	6.412	14.50	43.00
6	0.2007	0.09030	7.224	29.00	46.82
7 (H_{max})	0.2232	0.10045	8.036	43.50	50.17

derivatives of a given geometrical section can be determined. It can be inferred from the sampling plan in Fig. 7 that there are 7 geometries in total and 7 distinct reduced velocities are considered, which results in a test grid of 49 cases. Since, these 49 cases are carried out for each of the 3 degrees of freedom (DoF), i.e., pitch, heave, and shove motion, the total budget of the CFD simulations is 147 to determine the full set of 18 flutter derivatives for all the 7 geometries and reduced velocities defined in the sampling plan.

The chosen domain comprises of a combination of more streamlined and bluffer geometries as compared to the baseline geometry, which also tend to exhibit fairly different and contrasting aerodynamic behavior. This allows some degree of flexibility to the designer to play with the deck section properties and decide whether to improve the aerodynamic characteristics or to improve the structural stiffness by varying the sectional depth based on the local wind climate. Similarly, the consideration of a wide range of reduced velocities, comprising of low reduced velocities where non-linear features are typically present and high reduced velocities exhibiting where an asymptotic trend approaching the QST values is expected can also be appreciated, permitting a wide exploration of the aeroelastic phenomena.

4. CFD simulations

4.1. Computational modeling

4.1.1. Spatial discretization of the computational domain

The overall computational domain is a rectangle as shown in Fig. 8. The entire domain is divided into different regions with varying levels of mesh refinement to capture the important flow features, vortices, and the wake on the downstream side of the deck, which has a significant impact on the flow-induced aerodynamic forces. The key dimensional parameters of the computational domain, which is very similar to that in Fransos and Bruno, 2010, are reported in Table 2. An attempt is made to discretize the computational domain as efficiently as possible with adequate refinement level while still maintaining the Control Volume (CV) cells count as low as possible to reduce the overall computational cost/burden of simulation. Accordingly, the entire domain is divided into 5 regions, viz. Region A, B, C, D, and E. The overall length of the computational domain in the horizontal and the vertical direction are $Dx = 38.5B$ and $Dy = 27.0B$ respectively. Similarly, the rectangular refinement region within the domain is located at a distance of $\Delta x = \Delta y = 8.5B$ from the inlet boundary in the horizontal and from the bottom face in the vertical direction. All the relevant dimensions of the computational domain including the refinement regions expressed in terms of the deck width (B) are shown in Fig. 8.

Table 2
Region wise distribution of CV cells in the computational domain along with max/min sizes in the medium mesh.

Region	Min. Size (m)	Max. Size (m)	Growth Rate	Num. of Cells
A	0.0008	0.0090	0.009144	247,589
B	0.0080	0.0250	0.015750	7,516
C	0.0250	0.1000	0.057500	3,219
D	0.0100	0.2000	0.045000	21,089
E	0.1500	0.4000	0.060000	3,718

Region A is the rectangular buffer region surrounding the deck section, in which important flow-critical phenomena such as the flow separation, attachment, and re-attachment takes place. The growth rate of cells within Region A is limited to about 0.09%, which provides a very finely resolved buffer region for flow-critical phenomena in the boundary layer. The region lying next to the Region A is Region B, which acts as a buffer region for capturing the wake formed on the downstream end of the deck. The growth rate of the CV cells within Region B is about 1.57%, which is coarser than Region A but still adequately fine to capture the vortex shedding on the downstream end. The region adjoining Region B is the wake refinement region designated as Region C, which serves two essential purposes, i.e., (a) to capture the separated shear layers from the surface of the deck which is then transported along the flow and gets dissipated on the downstream side including the wake formed behind the deck, and (b) to gradually increase the grid size while progressing ahead in the downstream side of the deck. The region lying exterior to the boundary layer, wake buffer, and wake refinement region is the Region D, whose primary purpose is to serve as a medium for smooth transition from a very finely resolved Region A, B and C to a relatively coarse CV cells distribution in Region D. Finally, Region E defines the overall extent of the computational domain which is located far away from the deck section, the boundary layer and wake refinement regions whose primary objective is to provide a freestream flow conditions and to minimize the effect of imposed boundary conditions on the flow around the deck. The details about the spatial discretization of

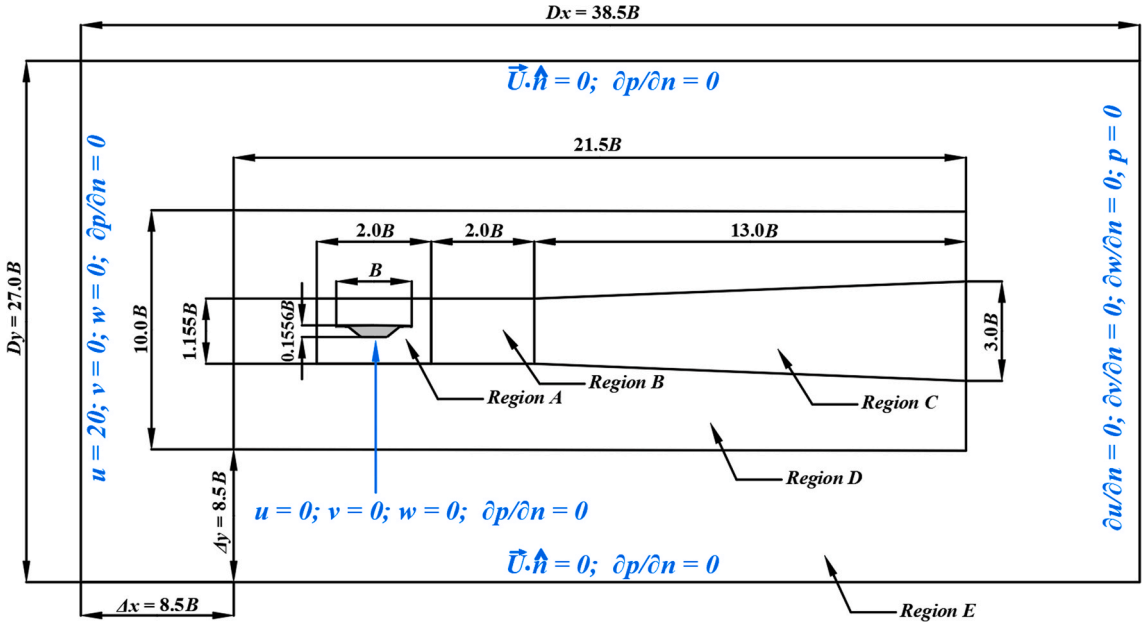

Fig. 8. Discretization of the computational domain with refinement regions for the baseline geometry ($H/B = 0.1556$).

computation domain including the wake buffer and wake refinement region for the baseline geometry, the lower and the upper bound shape designs, and the corner details are shown in Fig. 9. Further details about the region wise distribution of control volume cells including the maximum, the minimum cell sizes, their growth rate, and total region-wise cell count for the baseline geometry is presented in Table 2.

It is worth highlighting that a special care has been taken for the spatial discretization of the domain, especially the boundary layer, wake buffer and wake refinement regions. A target y^+ value of 1 (i.e., $y^+ \approx 1$) is sought after in the first layer of CV cells around the deck perimeter. The distribution of the y^+ values around the deck perimeter is shown in Fig. 10, in which it can be observed that the y^+ values around the deck perimeter remains less than 1 largely, exceeds 1 only at a few points and exceeds 2 at even fewer points. It should be noted that the plotted y^+ around the deck correspond to the time-averaged values over one complete cycle of harmonically fluctuating aerodynamic forces. While computing the time-averaged y^+ values over the full cycle, the y^+ distribution corresponding to 105 different time steps used to discretize a full cycle were averaged in time to obtain the plotted values.

Further details about the mean and the maximum y^+ of CV cells around the deck perimeter including the number and percentage of cells with $y^+ > 1$ and $y^+ > 2$ for the medium mesh considered in the current work is reported in Table 3. However, it is pointed out that the metrics presented in Table 3 correspond to that at the final timestep (at $t = 1$ s) of simulation using the medium mesh as opposed to an average over the full 1 cycle as presented in Fig. 10.

The comparison of mesh resolution considered in this work to that present in the contemporary literature reveals that the percentage of cells with $y^+ > 2$ is around 3.6% (Álvarez et al., 2019) whereas the same metric in current work is about 1.0%. Hence, this comparison provides an additional verification about the adequacy of mesh resolution pursued in the current piece of research.

4.1.2. *Parametrization of the computational domain for deck shape tailoring*

A parametrized semi-automated workflow was developed for the generation of any design candidate geometry needed in the sampling plan and in future design-oriented frameworks. In order to obtain a mesh for any geometry with the required depth of deck and refinement level, at first, the profile of the deck cross-section is created from nine control points, resembling the experimental CRIACIV section with $R/B = 0$. Among the nine control points, the two bottom edge corner points are shifted vertically up or down to obtain more streamlined geometries or bluffer geometries as compared to the baseline geometry configuration. Then, a small radius of curvature, $R = 0.05B$ is introduced at the two bottom corner points resulting in the curved arcs (arcs '*d-e*' and '*f-g*'; refer Fig. 6), which is the final profile of deck used in the CFD simulation. Once the deck outline with curved bottom edges is obtained, the coordinates of the boundary layer are then determined by uniformly projecting the deck outline outwards by a distance of $B/45$. Then, different refinement regions as highlighted in Fig. 8 are created with the maximum, the minimum cell size, and the growth rate of cells

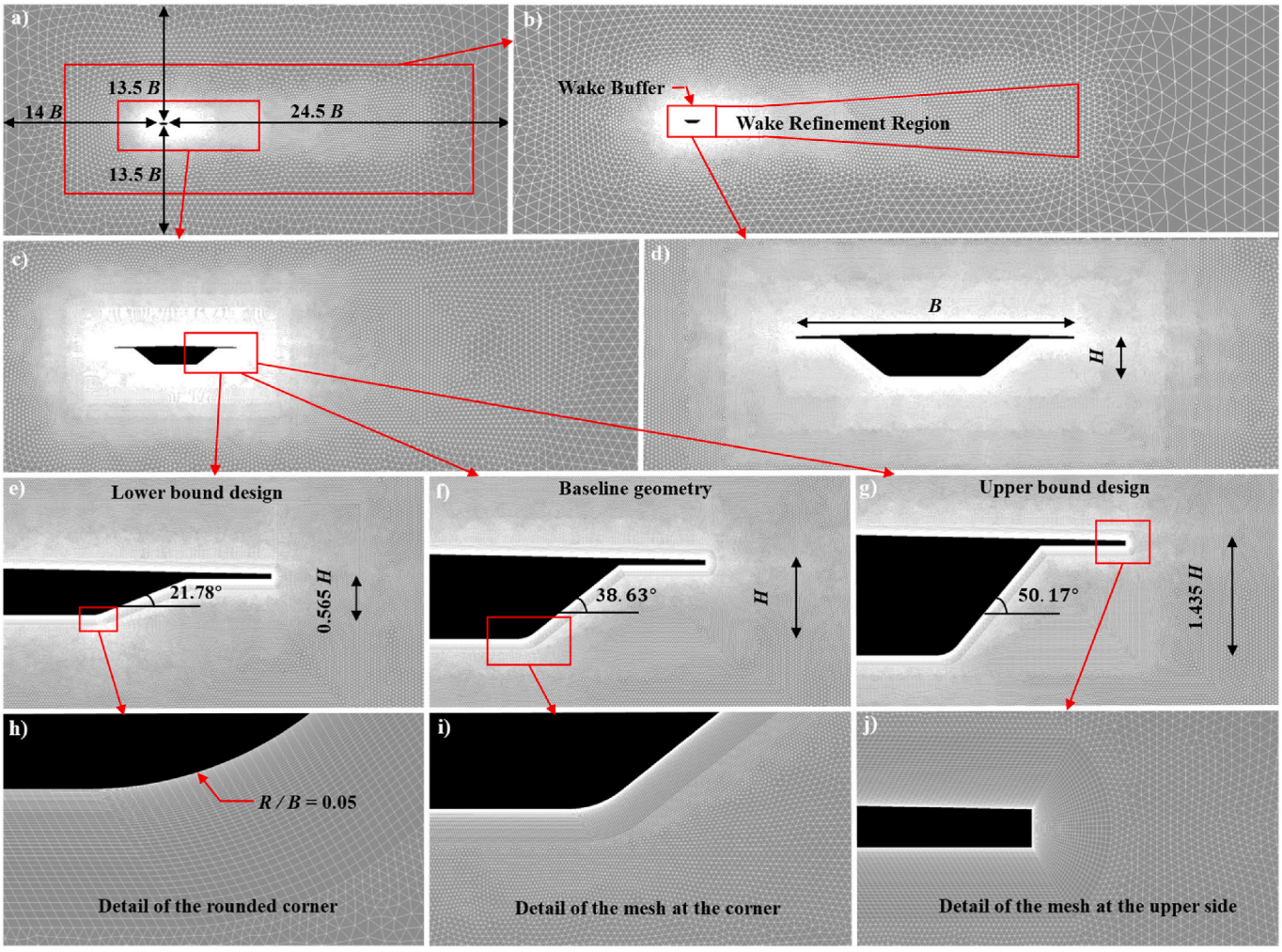

Fig. 9. Spatial discretization of the computational domain with refinement details for the baseline geometry ($H/B = 0.1556$), the lower bound design ($H/B = 0.0899$), the upper bound design ($H/B = 0.2232$) including the corner details.

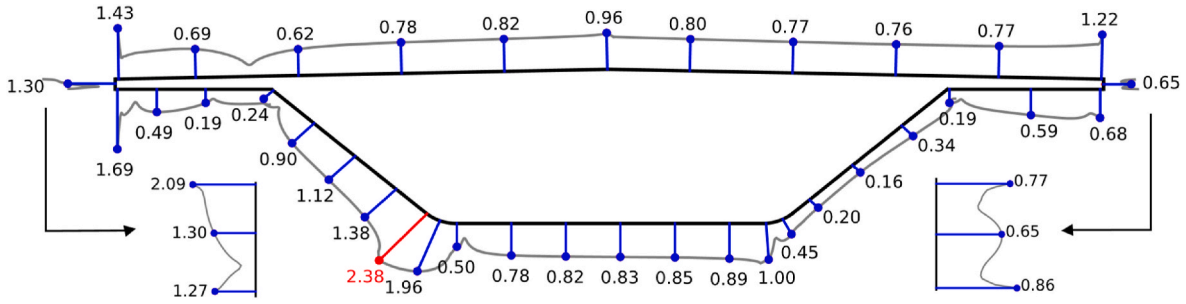

Fig. 10. Distribution of time-averaged y^+ over a full cycle around the perimeter of deck cross-section. The red marker represents the maximum y^+ around the deck perimeter.

Table 3
Mean and maximum y^+ values for CV cells around the deck perimeter at $\alpha = 0°$ in the medium mesh. y_1 is the height of the first layer cells in the BL, N_{BL} is the number of layers of hexahedral cells in BL, y_{BL} is the thickness of the BL, N_H is the number of cells around the deck perimeter, $\bar{y}^+$ is the mean y^+ value at the last time step ($t = 1$ s), Max. y^+ is the maximum value of y^+ at $t = 1$ s, % $y^+ > 1$ and % $y^+ > 2$ indicates the percentage of cells with y^+ value greater than 1 and 2 respectively, BL cells indicates the number of hexahedral cells in the boundary layer.

Fineness	y_1/B	N_{BL}	y_{BL}/B	N_H	$\bar{y}^+$	Max. y^+	% $y^+ > 1$	% $y^+ > 2$	BL cells
Medium	6.67×10^{-5}	50	0.022	1595	0.71633	2.37909	10.41	1.00	79,750

parametrized for each region to control the mesh refinement level in each region independently. Likewise, the number of divisions along the deck perimeter is also parametrized to control the cell aspect ratio in the 1st layer hexahedral cells in the boundary layer while that in the normal direction (to deck edges) is governed by the target y^+ value. Hence, this parametrization strategy enables (1) a precise control on the number of cells and the cell aspect ratio in the boundary layer including mesh refinement levels and (2) the ability to control the key mesh parameters for creating meshes for different deck shape designs in a semi-automated fashion.

4.1.3. Boundary conditions

The flow and boundary conditions imposed on the CFD model should reflect the experimental wind tunnel testing conditions so that a one-to-one comparison could be made while comparing the CFD datasets with the experimental datasets. Accordingly, at the inlet, Dirichlet boundary condition is specified with a uniform inlet velocity (U) of 20 m/s in the positive x-direction while a Neumann boundary condition is specified for pressure. At the outlet, Dirichlet boundary condition is specified for pressure with a value of $P = 0$ while the normal gradient of velocity is specified to be zero. The top and the bottom wall are set as slip walls while the boundary of the deck section is treated as a no-slip wall. The free-stream turbulent kinetic energy (k_∞) to be specified at the inlet is determined considering a turbulence intensity (I) of 1% using Eq. (22). The turbulent kinematic viscosity is computed from the internal field after solving the transport equations of k and ω.

$$k_\infty = {}^3\!/_2 (UI)^2 \tag{22}$$

Similarly, the free stream specific dissipation rate is computed using the eddy-viscosity ratio of unity in Eq. (23) and the specific dissipation rate at the walls is computed using Eq. (24).

$$\omega_\infty = \frac{\rho k_\infty}{\mu}\left(\frac{\mu_t}{\mu}\right)^{-1} \tag{23}$$

$$\omega_{wall} = 10\frac{6\nu}{\beta y_p^2} \tag{24}$$

In Eq. (23), μ is the molecular dynamic viscosity of fluid (air) whereas μ_t is the turbulent dynamic viscosity. Similarly, y_p is the distance of the centroid of the 1st CV cell from the wall, ν is the kinematic viscosity of air, and $\beta = 0.075$ in Eq. (24). For the dynamic CFD simulations, the amplitude of vibration imposed in the pitching motion is 2° whereas in the heaving and shoving motion are each 0.009 m in the respective directions, which corresponds to a non-dimensional amplitude of $0.128H_o$ as used in the study by Mannini et al. (2016).

4.1.4. Numerical schemes and solution algorithms

The second order accurate Finite Volume Method (FVM) is used for the discretization of the governing pde's into a linear system of equations. The convection term of the NS equation is discretized using the second order linear upwind scheme that requires the gradient of velocity to be specified. Similarly, the diffusion term in the NS equation is discretized using the Gauss linear corrected scheme, in which the viscosity is linearly interpolated across the control volume cells and a non-orthogonal correction factor is applied to account for non-orthogonality in non-orthogonal meshes. For the computation of surface normal gradient scheme, which is important to solve the Laplacian in the diffusion term of NS equation, corrected scheme is chosen, that applies an explicit non-orthogonal correction factor to maintain the second order accuracy. The pressure gradient term is approximated using the central differencing scheme and the solution advances in time using the second order accurate backward scheme with an adaptive timestep size such that the maximum Courant number is 1. The pressure-velocity coupling is done using the PISO algorithm using 2 outer corrector loops (also known as the PIMPLE algorithm). The pressure correction equation is solved using the PCG iterative solver while the momentum equation and the transport equations for k and ω are solved using the preconditioned bi-conjugate gradient (PBiCG) solver. The pressure correction equation is solved 3 times in the inner loop with 2 additional non-orthogonal correctors. An under-relaxation factor of 0.5 is used for the pressure field while a factor of 0.7 is chosen for the velocity, k and ω fields.

4.2. Verification and validation of static CFD simulation

4.2.1. Spatial verification of the entire computational domain

The verification studies of the CFD solution are used to assess whether the conceptual model from continuum mechanics/mathematics is solved correctly using discrete mathematics that is embodied in the form of a computer code (Oberkampf and Trucano, 2002; AIAA G-077-1998, 2002). The process of discretization occurs with respect to space and time. In the context of space, the discretization of the governing partial differential equations (PDE's) on a finite volume mesh

inherently introduces some spatial discretization error in CFD solution. Thus, it is important to conduct mesh convergence studies to ensure that the solution obtained from the CFD simulation is mesh independent. Accordingly, a mesh verification study was carried out using three different meshes, viz., Coarse, Medium, and Fine mesh for a static bridge deck (baseline geometry) at 0° angle of attack. The total number of control volume cells in the computational domain, the time-averaged force coefficients, the standard deviations, and the Strouhal number obtained from the three meshes is reported in Table 4. The integrated time-averaged force coefficients, the standard deviations, and the Strouhal number are calculated using a suitable length of the time history of aerodynamic forces once the flow attains a statistically steady state.

As it can be observed in Table 4 that the time-averaged force coefficients and the standard deviations obtained from 3 different meshes converge towards the same value (differing only in the 3rd or the 4th significant digit), which testifies that the obtained solution from CFD simulation is mesh independent. Hence, for all the further studies, the medium mesh is used unless otherwise stated.

4.2.2. Spatial verification of the boundary layer computational domain

Usually, the verification studies reported in the literature are done to check the adequacy of the spatial and the temporal resolution chosen for the CFD simulations. However, from some prior physical understanding of the problem, it has been observed that small vortical structures may form around the periphery of the deck section under the action of the wind. In the event that the cell aspect ratio of the hex-dominant cells in the boundary layer is too large, the mesh would fail to resolve the velocity gradients close to the wall, which in turn would lead to the failure of mesh in resolving the vortical structures in the periphery of the deck section. The failure to account for these vortical structures affects the aerodynamics of the deck section leading to inaccuracies in the calculated time-averaged force coefficients from aerostatic analyses and other subsequent analyses up to the computation of flutter derivatives. For an accurate depiction of the integrated time-averaged force coefficients on the deck section, the boundary layer formed around the deck is the most critical region from spatial discretization and CFD modeling point of view. This is because the solved pressure field and the shear stress in these CV cells (especially the 1^{st} layer cells) are used for the computation of integrated time-averaged force coefficients in each time-step (in either the aerostatic or the aeroelastic analyses). Thus, to ensure that the small vortical structures including the velocity gradients both in the direction of flow as well as the flow normal direction are captured well, another sensitivity study was carried out considering the mean cell aspect ratio of the 1^{st} layer cells in the boundary layer.

For that purpose, three different simulations were carried out for the static deck (baseline geometry) at 0° angle of attack with the medium mesh (as described in Section 4.2.1) by varying the cell aspect ratio around the deck perimeter. The number of hex-dominant cells in the 1^{st} layer cells of the boundary layer for different cell aspect ratio cases including the time-averaged force coefficients, Strouhal number, and the standard deviation values are listed in Table 5. Since, the values of the time-averaged force coefficients, the standard deviations, and the Strouhal number tend to converge towards the same value (only with subtle variations) in Table 5, thus, this sensitivity study with respect to the cell aspect ratio serves as an additional confirmation that the spatial discretization considered in Section 4.2.1 provides adequate spatial resolution to capture all the relevant flow structures. Unless otherwise stated, the medium mesh with cell aspect ratio, AR ≈ 20 is considered for all the simulations, analyses, and results presented in the subsequent Sections.

4.2.3. Temporal verification

In addition to spatial discretization errors, there is a possibility of error being introduced in the CFD solution if the temporal resolution chosen for the simulation is not adequate. In other words, if the time-step size is too large in an unsteady problem, the solution becomes prone to errors as all the relevant transient flow phenomena are not resolved due to the lack of adequacy of temporal resolution. This applies for both the implicit scheme and the explicit time schemes; for implicit schemes, the solution may still be obtained but with inaccuracies while for the explicit schemes, the solution often becomes unstable and diverges beyond a certain time-step size (when the courant number exceeds unity). Hence, as per the AIAA G-077-1998, 2002 recommendations, it is a common practice to conduct a set of simulations with varying time-step size to ascertain that the solution remains stable and consistent even when the time-step size is varied, which would ensure the adequacy of the temporal resolution of the CFD solution.

The flow of wind over the deck section considered in the current work is an unsteady problem. So, the flow evolves over the computational domain from one time step to another. As the flow evolves over time, it is necessary to also ensure that the solution remains both stable and is unaffected by the time step size. Thus, three different simulations were carried out for a static deck (baseline geometry) at 0° angle of attack with the medium mesh (as described in Section 4.2.1) by varying the courant number (i.e., $Co = 0.5$, 1.0 and 2.0) as listed in Table 6. The integrated time-averaged force coefficients, the standard deviation values, and the Strouhal number reported in Table 6 are computed using a suitable length of time history once the flow attains a statistically steady state. From Table 6, it can be again observed that the time-averaged force coefficients including the standard deviations, and the Strouhal number converge towards the same value (only with subtle variations), thus, it is concluded that the final solution is independent of the time step size testifying the adequacy of the temporal resolution considered in this work. For all the further analyses, the medium mesh as described in Section 4.2.1 with courant number of $Co = 1$ is used unless otherwise stated.

4.2.4. Validation of time-averaged force coefficients and Strouhal number

In addition to the verification studies, it is also critically important to validate the computational simulation results with experimental datasets or analytical solutions such as the thin airfoil theory (Theodorsen, 1934). Since analytical solutions to complex engineering problems that we encounter in real-life can rarely be found, usually the computational simulation datasets are compared/validated using the experimental datasets. As per the AIAA Guide for verification and validation of CFD simulations (AIAA G-077-1998, 2002), validation is the process of determining the degree to which a model is accurate representation of the real world from the perspective of the intended use of the model. For measuring the accuracy of the representation (computational simulation) of the real world, AIAA Guide recommends a systematic comparison of CFD results with the experimental data, while also underscoring the fact that all experimental data contain bias and random errors and the comparison of CFD results does not necessarily imply that the experimental data has higher accuracy. Hence, for the purposes of

Table 4
Comparison of time-averaged force coefficients, standard deviations, and Strouhal number between three different meshes at $\alpha = 0°$.

Mesh	No. of Cells	C_D	C_L	C_M	S_t	$\widetilde{C}_D$	$\widetilde{C}_L$	$\widetilde{C}_M$
Coarse	244,071	0.0675	−0.1186	0.0956	0.2833	0.00061	0.04861	0.01019
Medium	283,131	0.0676	−0.1197	0.0953	0.2847	0.00059	0.04792	0.01006
Fine	365,965	0.0677	−0.1193	0.0953	0.2855	0.00060	0.04857	0.01014

Table 5
Comparison of time-averaged force coefficients, standard deviations, and Strouhal number for the medium mesh at three different aspect ratio of boundary layer cells and at $\alpha = 0°$.

Aspect Ratio	No. of BL cells	C_D	C_L	C_M	S_t	$\widetilde{C}_D$	$\widetilde{C}_L$	$\widetilde{C}_M$
≈ 10	3,070	0.0675	−0.1066	0.0957	0.2844	0.00063	0.05035	0.01055
≈ 20	1,595	0.0676	−0.1197	0.0953	0.2847	0.00059	0.04792	0.01006
≈ 27	1,284	0.0668	−0.0990	0.0969	0.2812	0.00064	0.05065	0.01065

Table 6
Comparison of time-averaged force coefficients, standard deviations, and Strouhal number for the medium mesh at three different Courant numbers and at $\alpha = 0°$.

Co	dt	C_D	C_L	C_M	S_t	$\widetilde{C}_D$	$\widetilde{C}_L$	$\widetilde{C}_M$
0.5	4.525×10^{-6}	0.0676	−0.1231	0.0953	0.2911	0.00059	0.04786	0.01005
1.0	8.875×10^{-6}	0.0676	−0.1197	0.0953	0.2912	0.00059	0.04790	0.01005
2.0	1.737×10^{-5}	0.0675	−0.1152	0.0953	0.2906	0.00056	0.04782	0.01003

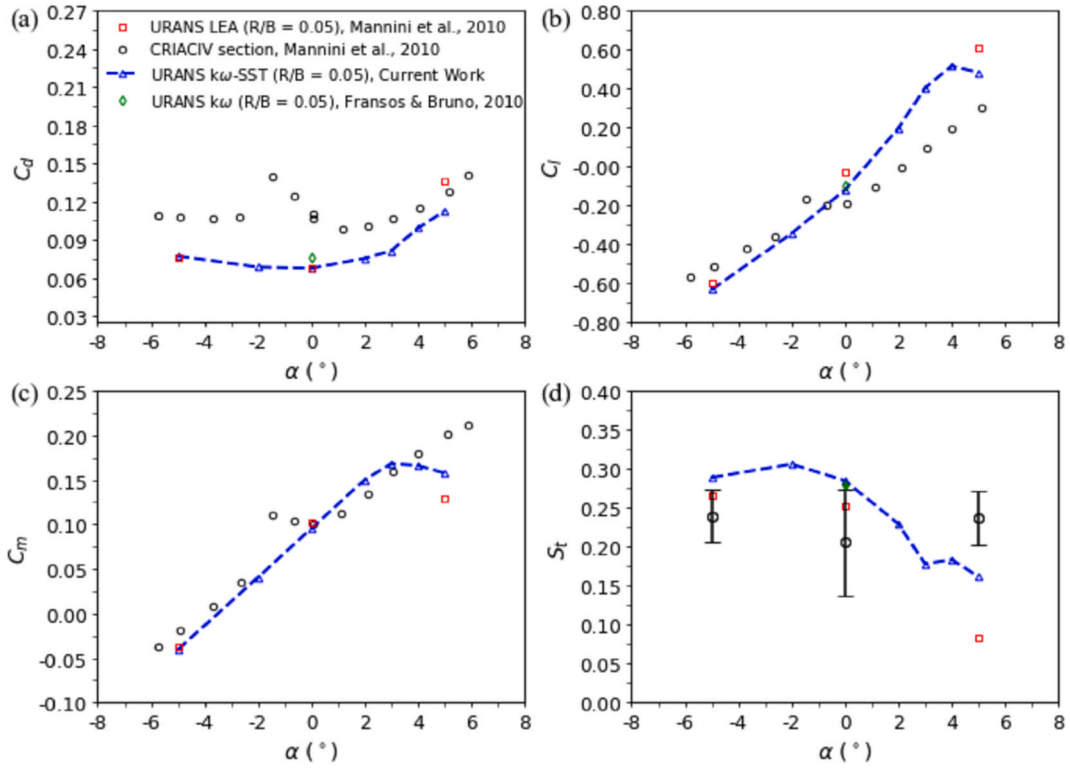

Fig. 11. Comparison of force coefficients and Strouhal number at different angles of attack from current CFD simulations and published literature: (a) Mean C_D vs α, (b) Mean C_L vs α, (c) Mean C_M vs α, and (d) S_t vs α.

validation, the integrated time-averaged force coefficients, and the Strouhal number is plotted as a function of the angle of attack in Fig. 11 and compared with the experimental as well as computational datasets available in the published literature (Mannini, 2006; Mannini et al., 2010; Fransos and Bruno, 2010). From the set of considered references, Mannini, 2006 pertains to the experimental datasets obtained from the CRIACIV wind tunnel facility at the University of Florence whereas the datasets pertaining to Mannini et al., 2010; Fransos and Bruno, 2010, are the datasets obtained from CFD simulation on the deck section same as what is chosen for the current work.

From Fig. 11, it can be observed the time-averaged force coefficients from current simulation exhibits a very good agreement with the computational datasets but shows some degree of variability (especially the drag coefficient curve and the Strouhal number curve) when compared with the experimental datasets. With regards to the drag coefficient curve, it is believed that a rougher surface of the deck sectional model used in the wind tunnel facility could have led to a higher value of mean drag coefficient in the CRIACIV section whereas the surface of deck section considered in the current simulation is smooth, leading to a better match with the numerical data reported by Mannini et al., 2010; Fransos and Bruno, 2010. Additionally, it is reported that the Strouhal number for the CRIACIV section is taken as the average of result at different Reynolds numbers in the range of $0.75 \times 10^5 \leq Re \leq 8.1 \times 10^5$, and some level of uncertainty was noticed in the hot-wire anemometer measurements (Mannini et al., 2010). It is believed that a lack of perfect parity in the flow conditions and the geometry conditions such as the degree of roundedness of the bottom edge corners and the wall roughness is the reason for variability between the experimental datasets and the CFD results from the current work and those reported in the literature.

Nevertheless, it is also emphasized that the CFD datasets from current study exhibit a very good agreement with the computational studies from Mannini et al., 2010; Fransos and Bruno, 2010, which are based on similar aerostatic analysis on the same deck section as considered in the current work. Thus, it is concluded that the validation efforts pursued in

this piece of research is in compliance with that published in the existing literature on the same deck section. Finally, based on the collective analysis of datasets in the validation plot (Fig. 11) by comparing the results from k-ω SST model from the current work with that from the experimental CRIACIV section and CFD datasets from Mannini et al., 2010; Fransos and Bruno, 2010, the following conclusions are drawn: (a) the variation of mean drag coefficient as a function of the angle of the attack is fairly captured as manifested by the concavity of the mean drag coefficient curve (b) the linearity of the mean lift coefficient curve is also captured well for the negative angles of attack and for lower values of the positive angles of attack; however, the CFD model predicts an early onset of stall for the deck section whereas in the experimental model, the onset of stall on the positive angle of attack side is somewhat delayed (c) the mean moment coefficient also exhibits a decent agreement with the experimental curve except for an early prediction of the onset of stall as compared to experiment, and (d) the Strouhal number curve exhibits some degree variability when compared with the experimental datasets; however, the uncertainties associated with the experimental measurements including the CFD modeling assumptions and turbulence model, all collectively might have a role to play in the observed variability. Overall, on a holistic basis, the CFD model follows the trend of a real-world physical measurement quite well and can reproduce the bulk of the important flow features affecting the aerodynamics of the deck system, thus, the CFD model is said to be validated.

4.2.5. Comparison of the flow field

An attempt to comparatively assess the extent of agreement between the streamlines obtained from the current CFD simulation to that from Mannini et al., 2010 is pursued in this Section. For that purpose, a surface line integral convolution (surface LIC) plot is extracted from current CFD simulation (corresponding to the baseline geometry at 0° AoA with $R = 0.05B$) and is plotted in the background as shown in Fig. 12. On top of the surface LIC plot, the digitized streamlines from Mannini et al., 2010 (for the same geometry, AoA, and R/B ratio) is overlayed to yield the plot in Fig. 12.

It should be noted that both the streamlines correspond to a time-averaged flow field in which the time-averaging is carried out for the full one complete cycle of harmonically oscillating aerodynamic forces. The overlay analysis of the streamlines also reveals a fair agreement between the streamlines obtained from the current CFD simulation to that from Mannini et al., 2010 with some minimal differences. For instance, the vortical structure formed on the left top edge in the current CFD simulation is somewhat smaller as compared to that obtained from Mannini et al., 2010. Except for this feature, the surface LIC plot obtained from the current CFD simulation exhibits an overall good agreement.

4.2.6. Analysis of the mean pressure distribution over the deck surface

The aerostatic mean pressure coefficient averaged over a full cycle of harmonically oscillating aerodynamic forces is plotted over the surface of the deck in Fig. 13. In this plot, the pressure coefficient values are orthogonally projected from the surface of the deck in the outward or the inward direction. In this Section, a one-to-one comparison of the pressure distribution plot is not carried out as the mean pressure distribution plot in Mannini et al., 2010 consists of a deck section with a sharp cornered edge ($R/B = 0$) with fairly different aerodynamic behaviour.

4.3. Verification and validation of dynamic CFD simulation

4.3.1. Spatial verification based on sensitivity of self-excited forces

The key variables of interest in the dynamic CFD simulations are the aeroelastic flutter derivatives, which are also used for comparison/validation with existing literature in the following sections. Thus, an additional set of verification studies was carried out for the dynamic CFD simulation (in which a harmonic motion was imposed on the deck) and is reported in this Section. As stated earlier, all the 3 DoFs are imposed on the deck system in an uncoupled manner, i.e., the deck oscillates either in vertical, lateral, or the torsional mode at a time but not concurrently. For the purposes of this verification study, three different simulations were carried out with a motion-imposed deck section oscillating in torsional mode of vibration with an amplitude of oscillation of 2° at reduced velocity ($U^* = 10.0$).

The total number of CV cells including the aeroelastic flutter derivatives obtained from three different meshes is listed in Table 7. From Table 7, it can be again observed that the computed flutter derivatives tend to converge towards the same value (only with subtle variations), thus, it is concluded that a mesh-convergent solution is obtained justifying the adequacy of the spatial resolution considered for dynamic CFD simulations chosen for this work. For all further analyses, the medium mesh as described in Section 4.2.1 with courant number of $Co = 1$, is used unless otherwise stated. In addition, the time-history of aeroelastic lift force obtained from the three meshes including the waveform of the imposed rotation on the deck system is plotted in Fig. 14 (a), which again exhibits a decent agreement in the time-history of aeroelastic lift force from 3 different meshes.

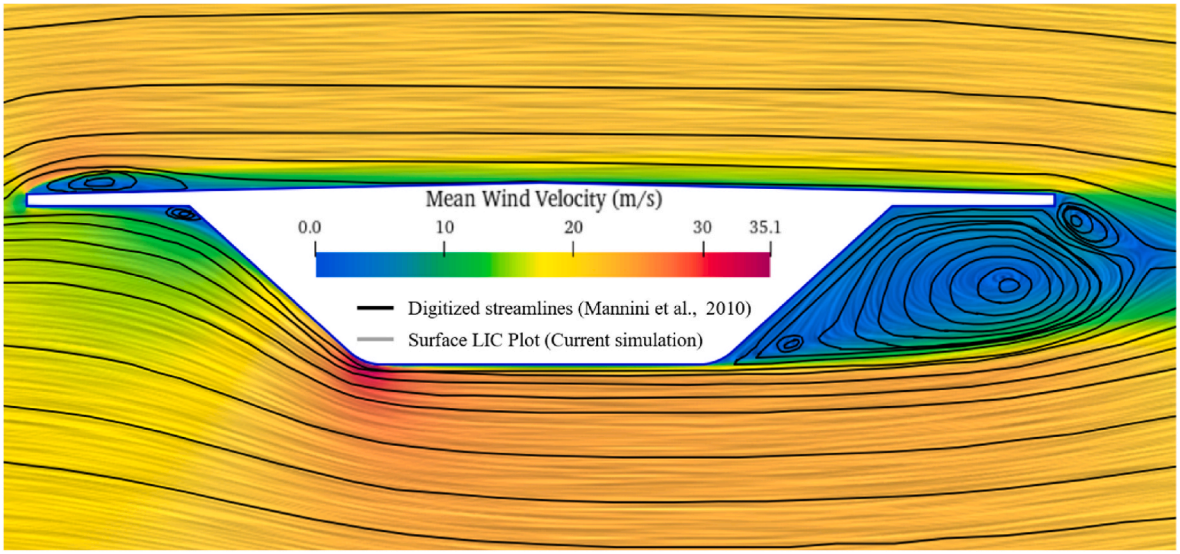

Fig. 12. Overlay analysis of digitized streamlines from Mannini et al., 2010 over the surface LIC plot from current static CFD simulation.

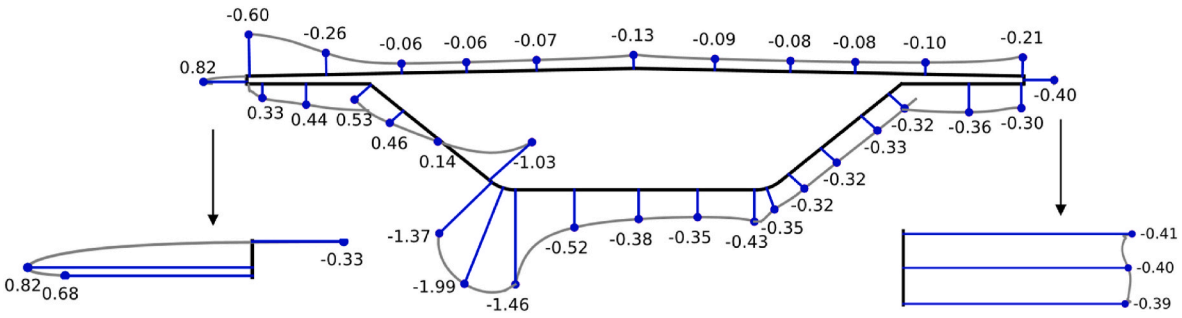

Fig. 13. Distribution of time-averaged C_p over a full cycle around the perimeter of deck cross-section.

Table 7
Comparison of the six flutter derivatives (A_i^*, H_i^*, P_i^*; $i = 2, 3$) obtained from the torsional mode of oscillation from three different meshes.

Mesh	No. of Cells	H_2^*	H_3^*	A_2^*	A_3^*	P_2^*	P_3^*
Coarse	244,071	1.8955	−9.7744	−0.6178	2.8017	0.0672	0.1943
Medium	283,131	1.8615	−9.7932	−0.6190	2.7982	0.0635	0.1962
Fine	365,965	1.8911	−9.8040	−0.6198	2.7977	0.0644	0.1953

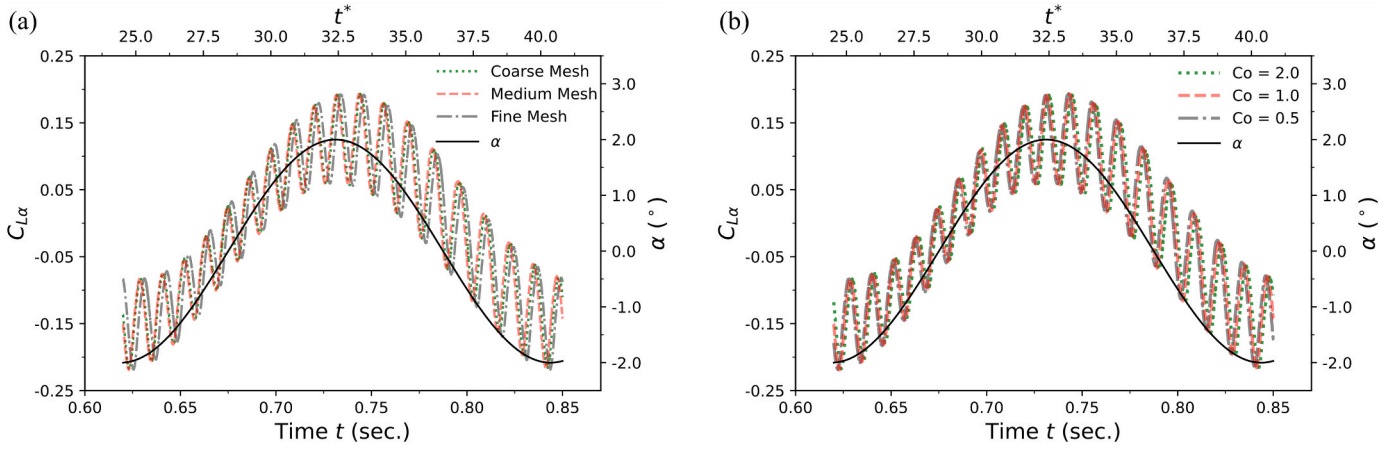

Fig. 14. Comparison of time histories of aeroelastic lift coefficient: (a) from Coarse, Medium, and Fine meshes, and (b) at different Courant numbers ($Co = 0.5$, 1.0, and 2.0).

4.3.2. *Temporal verification based on sensitivity of self-excited forces*

The governing partial differential equations in a dynamic CFD simulation are also discretized with respect to time, so, using similar arguments and reasoning as is included in Section 4.2.3, another temporal verification study was carried out considering the torsional mode of vibration of the deck section at $U^* = 10.0$ with the oscillation amplitude of 2° (same as in Section 4.3.1) with different courant numbers and the medium mesh. Since, the solver chosen for this work is 'pimpleFoam', which has the provision to allow for adaptive time step size depending upon the maximum Courant number (which in this case is $Co = 1$), thus time step size might differ from one time step to another as the simulation progresses. However, once the flow field is stabilized with distinct periodically fluctuating aerodynamic forces in time, the time step size is expected to be constant. Thus, the mean value of time step size is computed after the flow field becomes steady and is reported in Table 8 including the 6 flutter derivatives (A_i^*, H_i^*, P_i^*; $i = 2, 3$) that are obtained from the torsional mode of vibration.

From Table 8, it can be again observed that the computed flutter derivatives tend to converge towards the same value (only with subtle variations) regardless of the time step size (or alternately the Courant numbers), thus, it is concluded the temporal resolution provided by the medium mesh at $Co = 1$ is adequate for the current scope of work. For all further analyses pertaining to dynamic simulations, the medium mesh at $Co = 1$ is used unless otherwise stated.

4.3.3. *Validation of the aeroelastic lift coefficient time history*

The flutter derivatives as a function of the reduced velocity (U^*) are considered for validation in this Section. For the validation of dynamic CFD simulation, two metrics are essentially considered, i.e., (a) validation of the time history of aeroelastic lift coefficient force, reported in

Table 8
Comparison of the six flutter derivatives (A_i^*, H_i^*, P_i^*; $i = 2, 3$) obtained from the torsional mode of oscillation for medium mesh at three different Courant numbers (Co).

Co	dt	H_2^*	H_3^*	A_2^*	A_3^*	P_2^*	P_3^*
2.0	4.410×10^{-6}	1.9316	−9.7793	−0.6145	2.7892	0.0674	0.2076
1.0	2.250×10^{-6}	1.8615	−9.7932	−0.6190	2.7982	0.0635	0.1962
0.5	1.147×10^{-6}	1.8278	−9.8085	−0.6195	2.8010	0.0610	0.1878

this Section and (b) validation of 8 flutter derivatives (A_i^*, H_i^*; $i = 1, 2, 3, 4$) obtained from the torsional and vertical mode of vibration, which is reported in the following Section. The time history of aeroelastic lift coefficient corresponding to the torsional mode oscillating at a reduced velocity of $U^* = 10.0$ is extracted from Mannini et al., 2016 by digitization. Then, the time history of corresponding force coefficients ($C_{l,ae}$) obtained from current CFD simulation are overlayed one over the other as shown in Fig. 15, where in the imposed harmonic motion on the deck system is also plotted as a function of non-dimensional time (α vs t^*). It is important to note that the horizontal axis in Fig. 15 includes the non-dimensional time (t^*), which is related to the physical time (t) by $t^* = Ut/B$.

From Fig. 15, a good agreement can again be noticed between the digitized time history of aeroelastic lift coefficient from Mannini et al., 2016 and the current CFD datasets, thus validating the numerical framework for dynamic simulation considered in this work. There are variations between the two simulations in the overlap of the time histories, which may be caused by differences in turbulence modeling approaches, space, and time discretization, among other reason. Nevertheless, it will be demonstrated in the upcoming Section 4.3.4 that the computed values of flutter derivatives using the same time history exhibit a very good agreement between the numerical and the experimental datasets available in the published literature. Thus, it is concluded that the simulation framework presented in the current work is able to reproduce the trend of real-world physical measurements, and thus the model is considered to be validated.

4.3.4. Validation of flutter derivatives from torsional and vertical vibration modes

The next metric used for validating the dynamic CFD simulation framework is through the comparison of 8 flutter derivatives (A_i^*, H_i^*; $i = 1, 2, 3, 4$) as a function of reduced velocity (U^*) obtained from the torsional and the heaving modes of vibration with that from the experimental CRIACIV section (Mannini, 2006) and the CFD datasets from Mannini et al., 2016. In addition, the flutter derivatives obtained from the Quasi-Steady Theory (QST) are also included in Fig. 16 for both the computational datasets, i.e., the one obtained from static simulation reported by Mannini et al., 2010 and the other obtained from static simulations from the k-ω SST model implemented in the current work. The inclusion of the curves from QST serves two essential purposes (a) these curves provide a baseline/reference for the trend of flutter derivatives when plotted as a function of reduced velocity (U^*) and (b) these curves also helps to demonstrate the limitations of the QST-based aero-structural design framework (i.e., how the flutter derivatives obtained from QST tend to exhibit greater degree of variability at higher reduced velocities, when compared with the ones obtained from an actual fluid-structure interaction study as proposed in this work). This also underscores the necessity to train the aeroelastic emulator with the flutter derivatives obtained from a real fluid-structure interaction for a better prediction of the response surface.

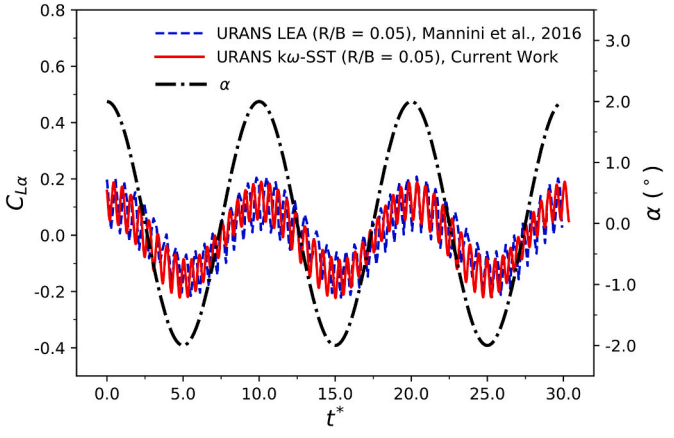

Fig. 15. Comparison of time history of aeroelastic lift coefficient with respect to non-dimensional time from the current dynamic CFD simulation and Mannini et al., 2016.

The comparison of flutter derivatives A_1^*, A_2^*, A_3^*, H_2^* and H_3^* exhibits a very good agreement with the experimental datasets as can be readily observed in Fig. 16. For H_1^*, the curve obtained from the current CFD simulation seems to have shifted slightly upwards but still captures the decreasing trend of H_1^* with increasing U^* quite well. The flutter derivatives A_4^* and H_4^*, however, exhibit some degree of variability when compared to the experimental datasets. But it is worth pointing out that the same flutter derivatives A_4^* and H_4^* show a decent agreement when the computational datasets from Mannini et al., 2016 are taken into consideration, both of which are based on the URANS framework. Regarding the variability with experimental datasets for A_4^* and H_4^*, it is emphasized in Mannini et al., 2016 that the experimental A_4^* and H_4^* are obtained from free vibration tests, which depend on the modification of stiffness matrix of the structural system by the aerodynamic stiffness contribution, which is quite low and at the same time uncertain. In addition, it has been observed that the flutter derivatives obtained from free and forced vibration exhibit some degree of variability (Mannini, 2015). Due to these reasons, the variability in case of A_4^* and H_4^* may have been observed between the CFD datasets from current simulation and that from Mannini, 2006. Even though there is some degree of variability in the flutter derivatives A_4^*, H_4^* and H_1^*, the other flutter derivatives exhibit a very good agreement overall and thus, holistically analyzing the flutter derivatives trend, it is concluded that the computational framework provides a good representation of real-world physical experimentation.

5. Aerodynamic and aeroelastic properties in the design domain

5.1. Force coefficient trend in the design domain

The time-averaged force coefficients and their slopes at angle of attack $\alpha = 0^\circ$ for 15 designs with an increasing non-dimensional deck depth H/B are reported in Table 9. It is to be noted that the original sampling plan consisted of 7 geometries in total, which are designated as 'Original' in Table 9 meaning those shape designs were part of the original sampling plan designed to build the aeroelastic emulator (Section 3.3) whereas the additional shape designs that were added later to better understand the trend of the force coefficients and the slopes as a function of the deck shape are designated as 'Added'. In general, the mean drag, lift, and moment coefficients increase with the increasing depth, however, the lift coefficient curve exhibits some interesting aerodynamic non-linearities. Similarly, the slopes of the drag and the moment coefficient remains nearly constant with subtle fluctuations whereas that of the lift coefficient exhibits a trend reversal of slope for certain geometries such as in the range of $0.1217 \leq H/B \leq 0.1386$. Thus, the results indicate that the time-averaged aerodynamic force (especially the lift force) is far from being a linear function of the deck depth in the design domain considered in this work. Further details are reported in Section 6.1.

5.2. Flutter derivatives trend in the design domain

There are different notations for expressing the flutter derivatives such as the Scanlan notation, the PoliMi notation, etc. However, as the Scanlan formulation is still the most widely used notation for expressing the flutter derivatives, the flutter derivatives for the 7 samples obtained from the 3 DoFs (pitching, heaving, and shoving motion) are first expressed as a function of reduced velocity in Scanlan notation in Fig. 18. Later, the flutter derivatives are also expressed in the PoliMi notation for all the 7 samples to highlight some salient features such as the manifestation of distinct non-linearities in the lower reduced

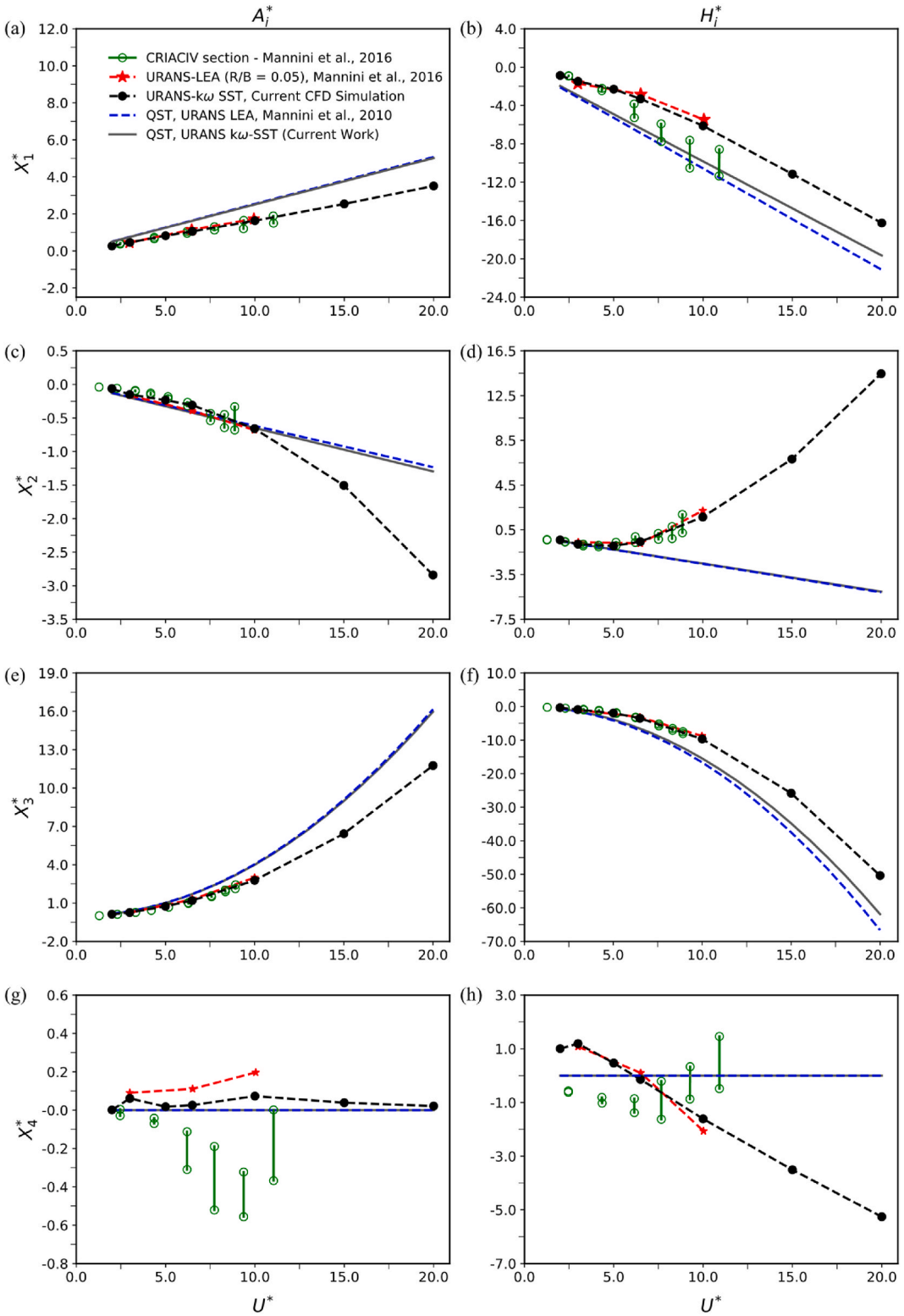

Fig. 16. Comparison of the flutter derivatives in Scanlan formulation based on the pitch and heave DoF from the current dynamic CFD simulation and published literature (a) A_1*, (b) H_1*, (c) A_2*, (d) H_2*, (e) A_3*, (d) H_3*, (f) A_4*, and (h) H_4*.

velocity range as well as the peculiar asymptotic trends at higher reduced velocity range. In addition to the flutter derivatives obtained from current CFD simulations, the variation of flutter derivatives as a function of reduced velocity from thin airfoil theory is also plotted in Fig. 18, which serves as an additional validation metric for the trend of flutter derivatives obtained from CFD simulations.

Much of the discussion in the following paragraphs about the interpretation of the trend of flutter derivatives as a function of reduced velocity for all the 7 samples is based on the following equations of the motion and how the obtained flutter derivatives modify the stiffness and the damping matrix of the structural system. With this aim, the equations of motion for the 3 DoF system (Holmes and Bekele, 2021) are

Table 9
Force coefficients and their slopes obtained for different deck geometries inside the design domain. Shape designs designated as 'Original' are part of the sampling plan described in Section 3.3. The 'Added' shape designs facilitate the interpretation of the aerodynamic behavior in the design domain.

Design	Sample	H/B	$C_{D,0^\circ}$	$C_{L,0^\circ}$	$C_{M,0^\circ}$	$C'_{D,0^\circ}$	$C'_{L,0^\circ}$	$C'_{M,0^\circ}$
1	Original	0.0879	0.028	−0.216	0.029	−0.164	4.630	1.515
2	Added	0.0992	0.032	−0.184	0.046	−0.125	4.541	1.549
3	Original	0.1104	0.037	−0.133	0.060	−0.093	4.977	1.593
4	Added	0.1217	0.043	−0.120	0.071	−0.011	4.367	1.551
5	Added	0.1274	0.047	−0.142	0.075	0.062	3.263	1.491
6	Original	0.1330	0.050	−0.147	0.079	0.028	3.847	1.526
7	Added	0.1386	0.055	−0.148	0.083	−0.007	4.759	1.559
8	Added	0.1443	0.059	−0.141	0.088	−0.037	5.725	1.584
9	Original	0.1556	0.068	−0.120	0.095	−0.027	6.409	1.571
10	Added	0.1668	0.077	−0.095	0.103	−0.037	7.357	1.559
11	Original	0.1781	0.086	−0.071	0.112	−0.074	7.693	1.558
12	Added	0.1894	0.094	−0.052	0.119	−0.100	7.777	1.541
13	Original	0.2007	0.103	−0.030	0.128	−0.119	7.872	1.516
14	Added	0.2119	0.110	−0.001	0.136	−0.173	8.248	1.501
15	Original	0.2232	0.116	0.035	0.144	−0.288	8.888	1.502

presented below in Eq. (25).

$$\ddot{x} + 2\eta_x\omega_x\dot{x} + \omega_x^2 x = P_1^*\dot{p} + P_2^*\dot{\alpha} + P_3^*\alpha + P_4^* p + P_5^*\dot{h} + P_6^* h \tag{25a}$$

$$\ddot{y} + 2\eta_y\omega_y\dot{y} + \omega_y^2 x = H_1^*\dot{h} + H_2^*\dot{\alpha} + H_3^*\alpha + H_4^* h + H_5^*\dot{p} + H_6^* p \tag{25b}$$

$$\ddot{\alpha} + 2\eta_\alpha\omega_\alpha\dot{\alpha} + \omega_\alpha^2\alpha = A_1^*\dot{h} + A_2^*\dot{\alpha} + A_3^*\alpha + A_4^* h + A_5^*\dot{p} + A_6^* p \tag{25c}$$

In Eq. (25), ω_x, ω_y, and ω_z are the undamped circular frequencies of the system in the respective motion, whereas η_x, η_y, and η_z are defined by $\eta_x = \omega_x/2\pi$, $\eta_y = \omega_y/2\pi$, and $\eta_\alpha = \omega_\alpha/2\pi$, respectively. In addition, the contribution of the full set of 18 flutter derivatives to the aerodynamic stiffness and damping matrices and to the aeroelastic forces linking the structural displacement and velocity is depicted in Fig. 17.

It can be observed in Fig. 18 that the flutter derivatives A_1^*, H_1^* and H_4^* exhibit a tentatively linear trend with respect to the reduced velocity (U^*) for the 7 shape designs. More specifically, the flutter derivative A_1^* (which physically implies the aerodynamic damping contribution to the aeroelastic moment due to deck velocity in the heaving direction) at higher U^* range exhibits a drop in the slope for the bluffer section as compared to relatively streamlined ones but the magnitude of A_1^* remains positive for all the deck sections. Such trend indicates that the effective damping of the aero-structural system in the heaving motion would be more reduced for streamlined sections. The flutter derivative H_1^* (which implies the aerodynamic damping contribution to the aeroelastic lift force due to structural velocity in the heaving direction) increases in absolute value (remains negative though) with increasing U^*, which for the bluffer sections is slightly faster than those compared to relatively streamlined sections as indicated by steeper slopes. The physical interpretation of such trend signifies that the negative H_1^*, when transported to the left-hand side of Eq. (25), would increase the overall damping in the direction of heaving motion. It is also worth mentioning the trend transition from linear, in the case of streamlined geometries, to parabolic, for bluffer geometries, which is very clear when representing them in PoliMi notation (See Fig. 19). Another important flutter derivative is A_2^*, which plays a critical role in stall flutter when it changes its sign from negative to positive. In the current study, A_2^* varies non-linearly as a function of U^* and it remains negative for the tested range of $2.0 \leq U^* \leq 20.0$ for all the 7 shape designs. However, it is worth pointing that the slope of A_2^* gradually decreases as the sections become bluffer (with lower negative values) as compared to more streamlined sections. For the flutter derivative H_2^* (which implies the aerodynamic damping contribution to the aeroelastic lift force due to the rate of change of α), the slope is negative and H_2^* is also negative for the lower U^* range. However, as U^* increases, the slope gradually tends to 0 for the streamlined sections. For the bluffer sections, H_2^* remains very close to 0 in the lower U^* range but the slope starts increasing rapidly as the value of U^* increases. The implication of such behavior in H_2^* is that the bluffer sections at higher U^* are more susceptible to the aeroelastic instability. The flutter derivative A_3^* exhibits some difference in the trend for the streamlined and bluffer sections at higher U^* as compared to the lower U^* range. In the lower U^* range, the change in A_3^* across the different values of U^* is marginal although at higher U^* range, the slope for the streamlined sections is greater than the bluffer ones meaning the aerodynamic stiffness contribution to the aeroelastic moment due to the pitching motion increases faster for the thinner sections as compared to the bluffer ones in the higher U^* range. H_3^* exhibits a non-linear (almost parabolic variation) trend with increasing U^*. In the lower U^* range, the change in H_3^* is marginal from one geometry to another and across the different U^* values. However, as the value of U^* increases, H_3^* takes a slightly higher negative values for the bluffer sections as compared to the streamlined ones. The values of A_4^* are observed to be fairly close to zero indicating only a feeble contribution of the heaving motion to the

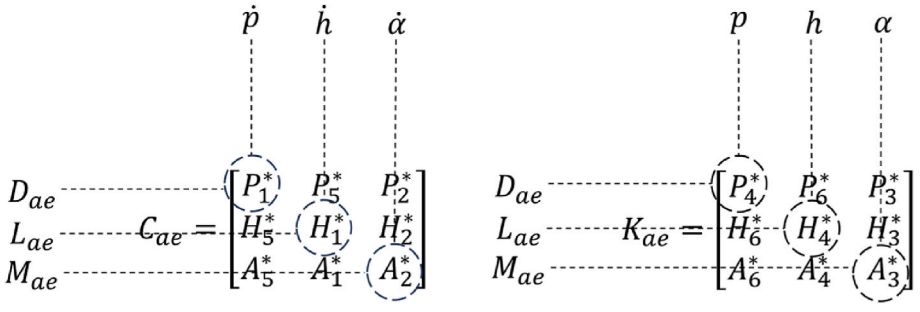

Fig. 17. Demonstration of the contribution of the full set of 18 flutter derivatives to the aerodynamic stiffness and damping matrix linking the structural velocity and displacement in the respective degree of freedom.

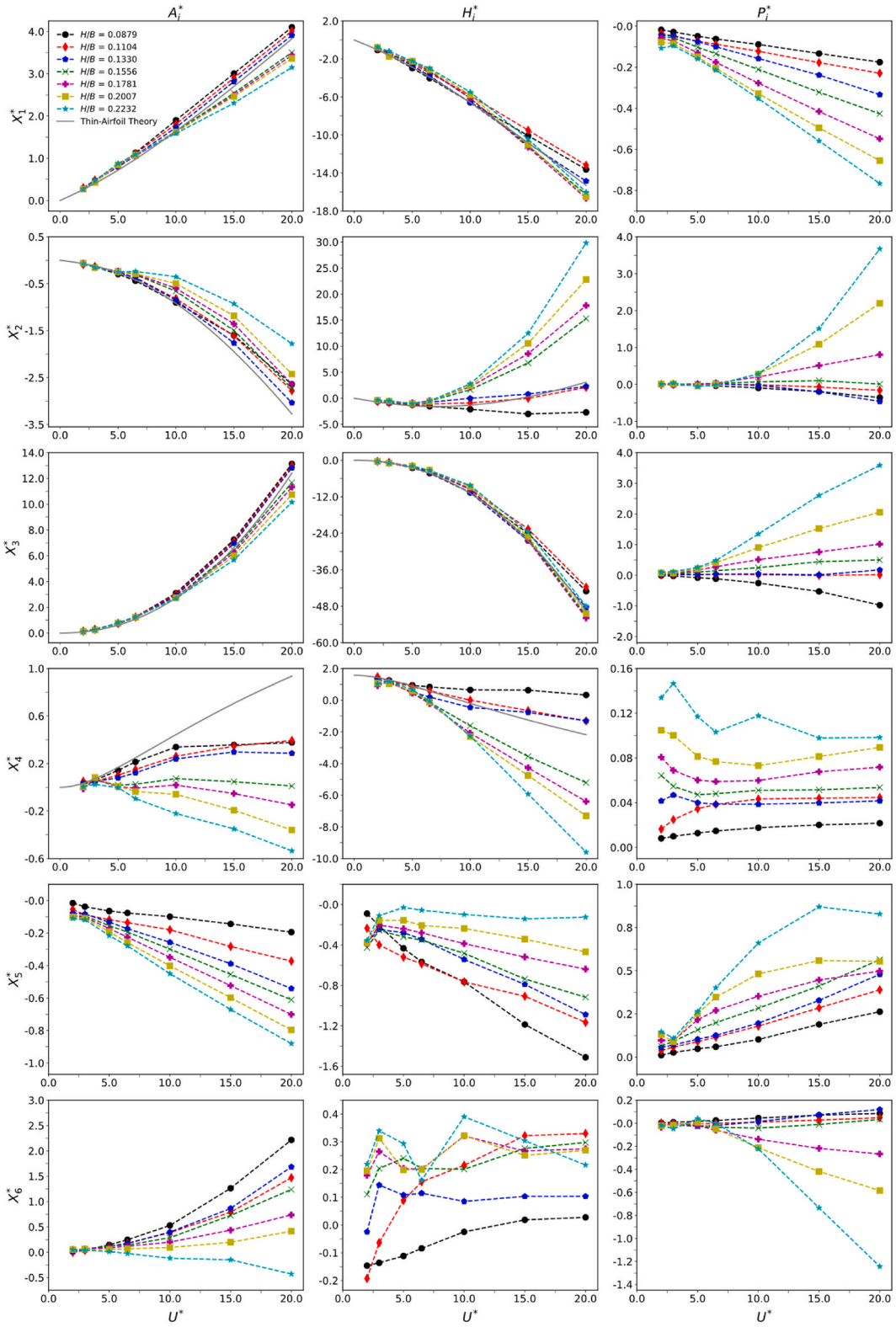

Fig. 18. Comparison of flutter derivatives (A_i*, H_i*, P_i*; $i = 1, 2, 3, 4, 5, 6$) in Scanlan formulation as a function of U* for all the 7 designs used in the sampling plan.

aeroelastic moments. It should be noted that A_4^* exhibits somewhat stark differences to that obtained from the thin airfoil theory as opposed to the general good agreement observed for A_i^*, H_i^*, where $i = 1, 2, 3$. In case of H_4^*, the values remain close to 0 or a slightly positive value across the range of U* for the most streamlined section. However, as the degree of bluffness of the section increases, H_4^* takes higher values with a negative sign with increasing U*. For the bluffest section, the slope is the greatest as compared to the relatively streamlined ones. This trend of H_4^* indicates that the overall stiffness of the system gets reduced for the streamlined sections whereas the opposite effect is observed for the bluffer ones. Also, the trend of H_4^* complies well with that obtained from thin airfoil theory with the streamlined sections bearing closer proximity

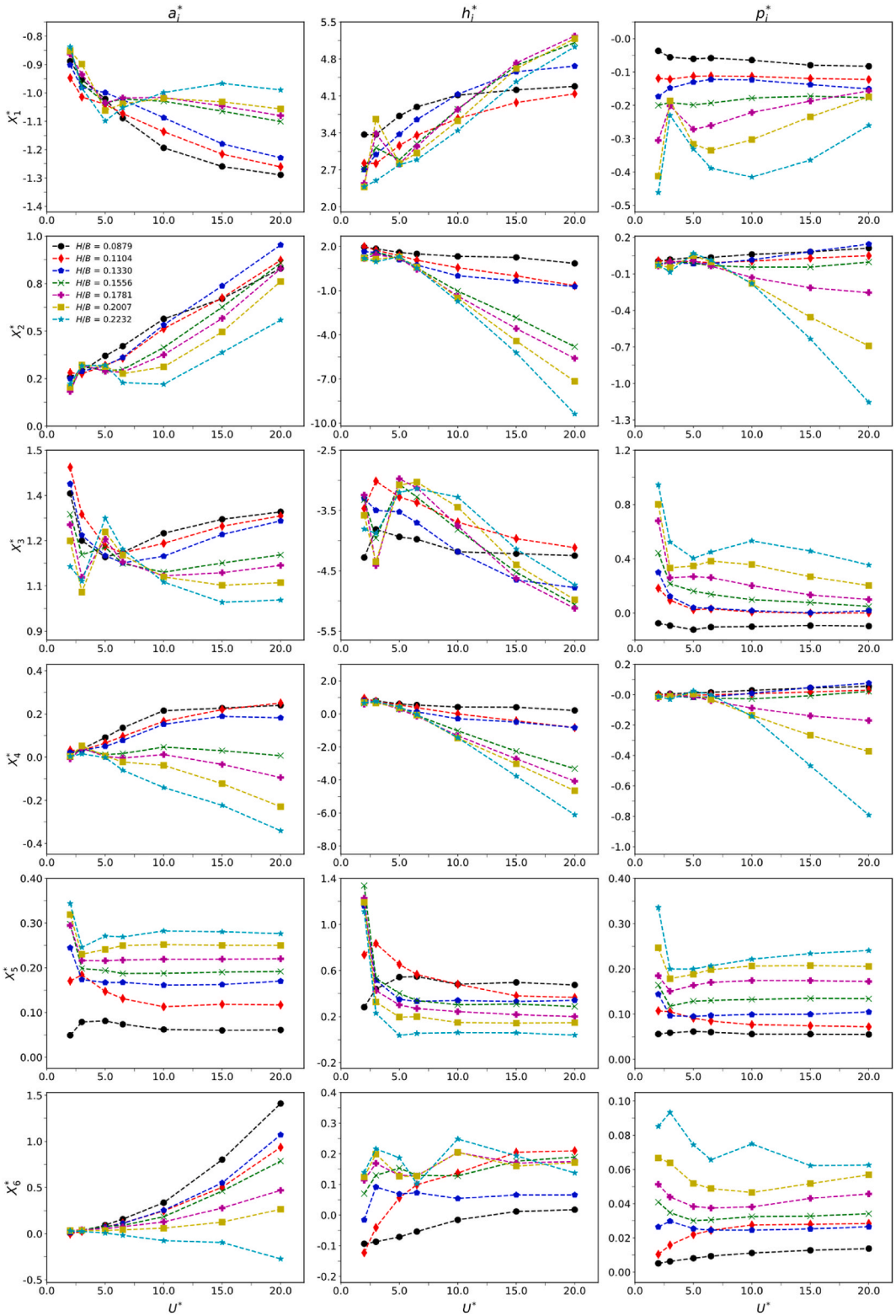

Fig. 19. Comparison of flutter derivatives (a_i^*, h_i^*, p_i^*; $i = 1, 2, 3, 4, 5, 6$) in PoliMi formulation as a function of U^* for all the 7 designs used in the sampling plan.

to the thin airfoil as compared to the bluffer ones.

Another important flutter derivative that contributes to the diagonal term of the aerodynamic stiffness matrix is the P_1^*. Except for a slight non-linearity for the bluffer sections in the lower U^* range, which is very clear when represented using the PoliMi notation (refer Fig. 19), P_1^* increases in magnitude (with a negative sign) almost linearly with increasing U^* and the rate of increase for the bluffer sections is relatively swifter as compared to the streamlined ones. For P_2^*, as U^* rises, the streamlined sections tend to exhibit a drop in the value of P_2^* towards the negative side whereas the bluffer sections exhibit a trend reversal in that the P_2^* rises swiftly to positive values as U^* increases. For P_3^*, the most streamlined section exhibits a gradually increasing magnitude with

negative sign at higher U^* range while the intermediate geometries ($H/B = 0.1104$ to $H/B = 0.1556$) almost remain stagnant at around $P_3^* = 0$ or a slightly positive value. However, as the section gets bluffer, P_3^* increases with a sharp slope and rises swiftly with increasing U^*. P_4^* exhibits some non-linear trend in the lower U^* range, which is more conspicuously visible for the bluffest section. P_4^* also exhibits a stationary trend with increasing U^* but exhibits an increase in the magnitude across all the ranges of U^* with increase in the depth of the section. The flutter derivative P_5^* exhibits an increasing trend with increasing U^* for all the sections; however, P_5^* increases in a linear manner for the streamlined sections whereas for the bluffer ones, it increases sharply and then later assumes a rough asymptotic trend around a particular value, which is higher for the bluffer sections. Similarly, the flutter derivative P_6^* increases in magnitude with a negative sign with increasing U^* with greater slope for higher H/B section ratios. For the thinner sections, P_6^* assumes a small positive slope and positive values. In general, it can be seen that the absolute value of all P_i^* flutter derivatives at all reduced velocities increases with the level of bluffness (H/B), which confirms the pivotal role of the drag flutter derivatives in the aeroelastic responses of bluff deck bridges (Miyata et al., 1995; Jones et al., 2003) and the importance of emulating these parameters as a function of the deck shape and reduced velocity during the aero-structural design and optimization of bridges.

Similarly, the flutter derivative H_5^* increases in magnitude with a negative sign for the relatively streamlined sections with increasing U^*. However, for the bluffer ones, the magnitude of H_5^* decreases and tends to approach towards 0 at higher U^*. On the other hand, some non-linearity is observed in the trend of H_6^* in the lower U^* range. For the thinner sections, H_6^* is negative at lower U^*, which increases to take 0 or a small positive value at higher U^* (such as $U^* = 20.0$). It is also observed that for streamlined geometries H_6^* assumes a roughly asymptotic trend approaching towards a constant value as U^* increases. However, this behavior is not very distinct and seems to have been delayed for the bluffest section. The flutter derivative A_5^* on the other hand increases in magnitude with negative sign with the increasing U^* in almost a linear manner. For the bluffer section, A_5^* takes higher values as compared to the thinner sections. Finally, A_6^* increases in magnitude with positive values with increasing U^* for all the shape design candidates except for $H/B = 0.2232$, which exhibits negative values and decreasing trend with increasing U^*.

In Fig. 18 and also while discussing the trend of flutter derivatives above, it is observed that several flutter derivatives such as the A_2^*, A_3^*, H_2^*, H_3^*, P_2^* and P_6^* show marginal or almost no variation in their magnitudes across the different values of U^* in the lower reduced velocity range when represented using the Scanlan notation. This is because the Scanlan formulation does not provide an adequate resolution and tends to obscure the non-linearities in the lower reduced velocity range (Zasso, 1996) because the different flutter derivative terms in Scanlan notation are already factored in by K_x or K_x^2 (where $x = h, p, \alpha$, are the reduced frequencies associated with respective motions) depending upon the motion component or its velocity. However, their PoliMi counterparts do not fare from this poor resolution and exhibit interesting non-linear trends in the lower reduced velocity range while also demonstrating an asymptotic trend converging towards a constant value in the higher U^* range. This behavior is more distinctly visible for relatively streamlined sections at high reduced velocities which complies well with the QST assumptions.

Hence, the full set of all the 18 flutter derivatives for the 7 samples as a function of reduced velocity is also plotted in PoliMi notation and is presented in Fig. 19. One of the key observations in PoliMi notation is that the flutter derivatives a_1^*, a_3^*, a_4^*, a_5^*, all h_i^*'s and all p_i^*'s attain a nearly constant value in the higher reduced velocity range, which is more distinctly visible for the streamlined geometries as compared to the bluffer ones in which the trend seems to have been slightly delayed due to subtle non-linearities in the curve. The relatively streamlined geometries comply readily with the asymptotic trend whereas the bluffer sections tend to approach towards the asymptotic trend (e.g., a_1^*, a_3^*) in some cases, although sometimes at higher reduced velocities, whereas in a few others even tend to digress from the asymptotic trend (a_2^*, h_2^*, h_4^*). Another notable feature of the flutter derivatives in PoliMi notation is the nonlinear trend in the lower reduced velocity range, which is visible in a_3^*, h_1^*, and h_3^*. Additionally, a striking feature of the trend in the PoliMi notation is the manifestation of distinct peaks in the lower reduced velocity range (such as for a_3^* at $U^* = 5.0$ for the geometries bluffer than the baseline geometry). Similar peaks were observed for some flutter derivatives in Zasso, 1996, and it was concluded that the peaks are due to the effect of vortex shedding. Such phenomenon is observed for a small range of reduced velocities in the lower reduced velocity region.

It must be highlighted that in order to guarantee an accurate simulation of the VIV response, the non-linearities caused by the deck motion amplitude must be considered to reproduce the complex mechanism occurring in the lock-in region properly. In this context, Wang and Chen (2022) have demonstrated that the steady vortex-induced vibration amplitude of a deck can be very well predicted by forced vibration CFD simulations and have found the results from CFD in good agreement with the wind tunnel tests. Other studies that have contributed to this direction include Tamura (1999), Noguchi et al. (2020), and Álvarez and Nieto (2024). While the present study is focused on emulating the self-excited forces as a function of the deck shape and reduced velocity, the numerical design methodology can be enhanced by adding these considerations when the design path requires an accurate simulation of the bridge amplitude-dependent response.

5.3. Performance of the QST formulation in estimating the flutter derivatives

In this Section, the limitation of the QST-based framework and the necessity for a more general and a versatile framework is substantiated with the help of flutter derivatives obtained from an actual fluid-structure interaction and using the quasi-steady theory. To demonstrate the limitations of the QST-based framework, the flutter derivatives ($A_i^*, H_i^*; i = 1, 2, 3$) at $U^* = 20.0$ obtained from the quasi-steady theory and an actual fluid-structure interaction via dynamic CFD simulations is plotted for all the 7 shape designs in Fig. 20.

It can be readily inferred from Fig. 20 that all the flutter derivatives ($A_i^*, H_i^*; i = 1, 2, 3$) exhibit a bifurcating tendency for the bluffer sections, which indicates that the QST-based framework is not suitable for bluff deck sections, which are prone to massive flow separations. Although for the streamlined sections, the two curves (i.e., the one obtained from dynamic CFD simulations and from the QST) tend to converge towards a similar value in case of H_i^* ($i = 1, 2, 3$); however, the discrepancy between the flutter derivatives obtained from dynamic simulation and QST is clearly visible for A_i^* ($i = 1, 2, 3$). This observation suggests that the application of QST-based framework to even the most streamlined section in the current scope of work yields inaccuracies as is the case for A_i^* ($i = 1, 2, 3$). Besides, another important observation from the plots in Fig. 20 is that flutter derivatives obtained from the QST formulation always results in an over-prediction of the absolute magnitude of the flutter derivatives A_i^* ($i = 1, 2, 3$) and H_i^* ($i = 1, 3$). This observation indicates that the QST formulation over-predicts the aeroelastic loads in this application case in the higher reduced velocity range and the extent of over-prediction rises with the degree of the bluffness of the section, which compromises the aeroelastic performance of any deck designed using the QST formulation. Hence, the necessity to opt for a more general and a versatile aero-structural design framework as proposed in this work is justified based on the observations above.

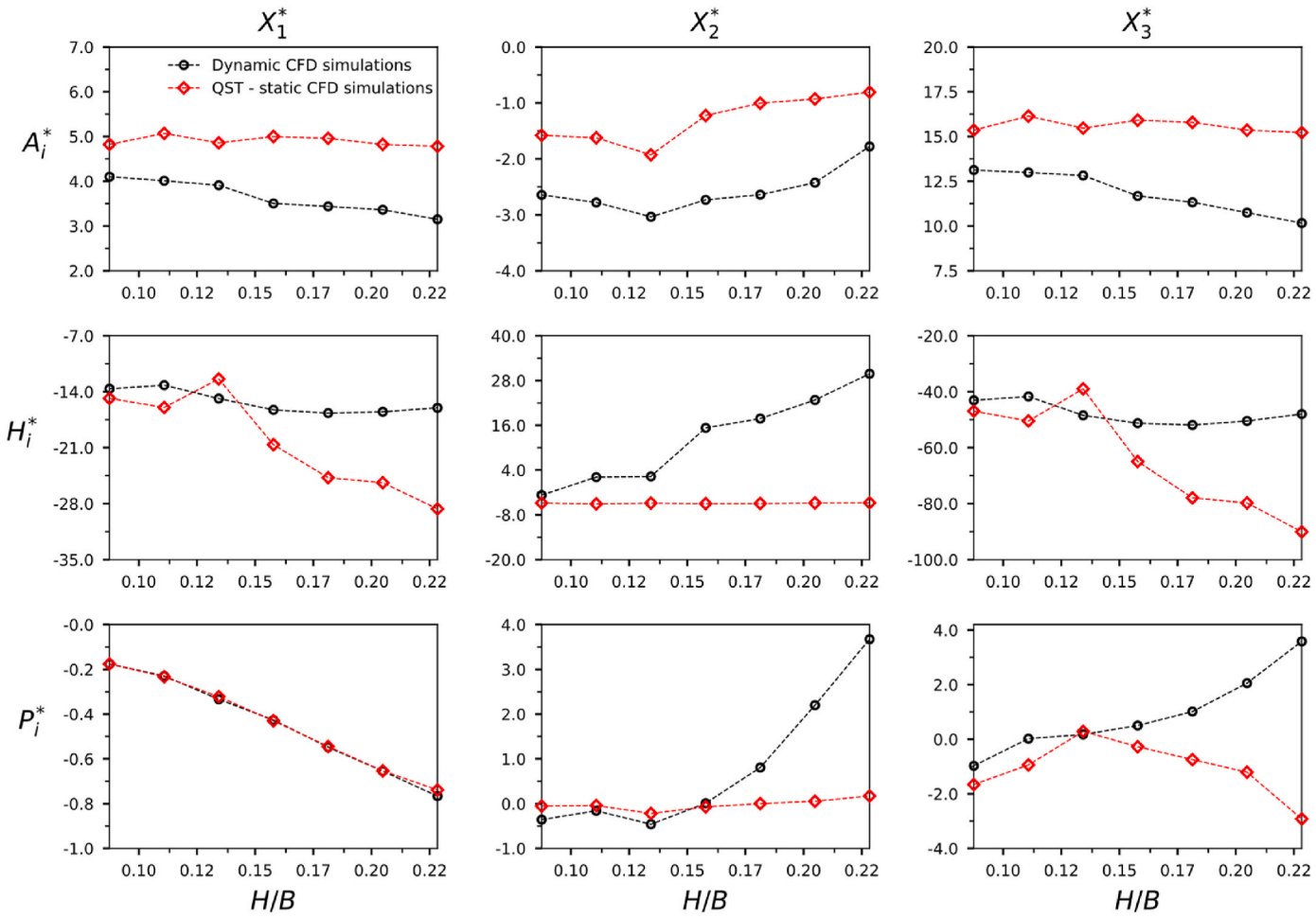

Fig. 20. Comparison of flutter derivatives (A_i^*, H_i^*, P_i^*; $i = 1, 2, 3$) from dynamic CFD simulations and those estimated using the QST formulation based on static CFD simulation represented in Scanlan notation at $U^* = 20.0$ as a function of H/B for all the 7 designs used in the sampling plan.

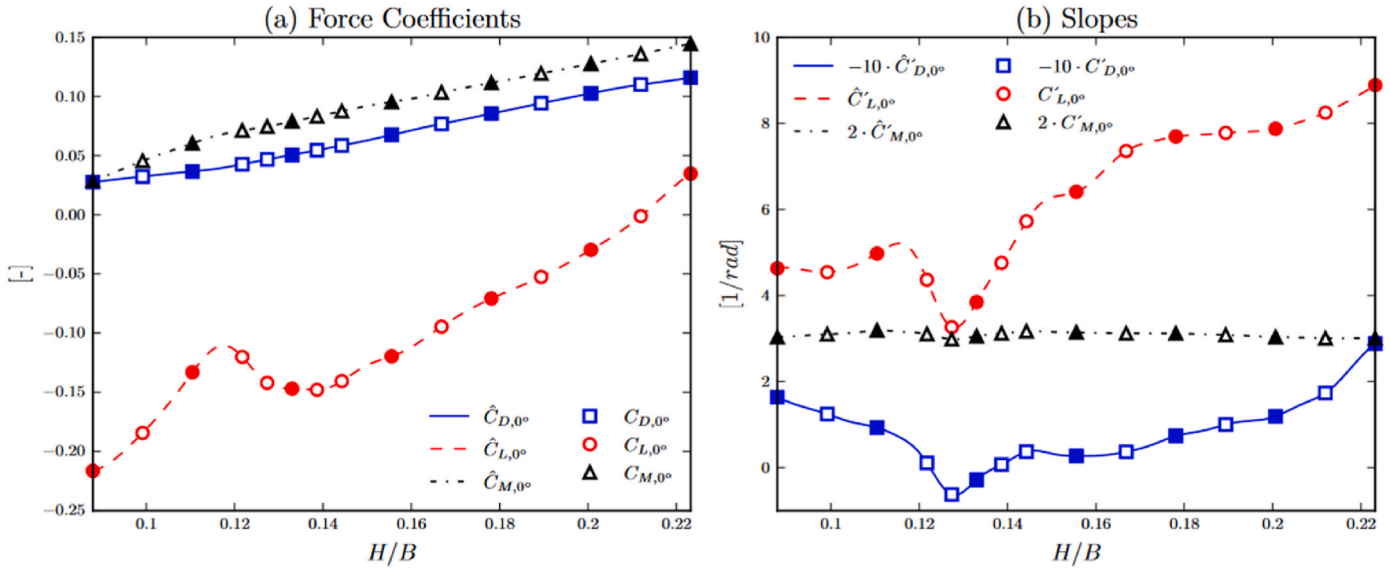

Fig. 21. Response curve for time-averaged force coefficients and their slopes with increasing depth of deck. Hollow markers are added shape designs and full markers are original shape designs according to Table 9. The symbol "^" indicates surrogate response curve. The slope of the drag coefficient is multiplied by a scale factor of −10 and the slope of the moment coefficient is multiplied by 2 to facilitate its visualization.

6. Emulation of aerodynamic and self-excited forces

6.1. Emulating shape-dependent force coefficients and slopes

The time-averaged integrated force coefficients and their slopes can be used for estimating the aerodynamic admittance functions, as described in Section 2.1.3. Hence, the data reported in Section 5.1. is used to build a steady aerodynamic surrogate model $\mathscr{A}_s$ to emulate the variation of the time-averaged integrated force coefficients and their slopes with regards to the deck shape S_d. The input of this steady aerodynamic surrogate is the deck shape, and the output are the frequency-independent force coefficients and their slopes, which can be formulated as:

$$\mathscr{A}_s(S_d) = \left[C_{D,0^\circ}, C_{L,0^\circ}, C_{M,0^\circ}, C'_{D,0^\circ}, C'_{L,0^\circ}, C'_{M,0^\circ}\right] \tag{26}$$

Fig. 21 shows the aerodynamic response curves obtained in the design domain. In general, it is inferred that the mean static wind loads on the shape design candidates increase with the increase in the depth of the deck section. This is due to variation in the formation, distribution, and the size of different vortical structures formed in the vicinity of the deck section resulting in different aerodynamic loads. However, an interesting observation from the curves in Fig. 21 is also that the variation of mean lift force is not quite linear as demonstrated by a distinct peak for $0.11 \leq H/B \leq 0.13$ in Fig. 21 (a). Similarly, the non-linearity in the trend of slopes of the lift coefficient is again distinctly visible for the shape design candidates with H/B ratios in the range of $0.12 \leq H/B \leq 0.14$. Thus, the curves suggest that it is of critical importance to properly account for the aerodynamic non-linearities while assessing the wind loads on different shape design candidates because some of the shapes in the nearby range might satisfy the buffeting and other aeroelastic design requirements and specifications very well, however, a few design sections might still fail the design requirements and specifications due to the appearance of sudden aerodynamic non-linearities for certain designs.

6.2. Emulating shape- and frequency-dependent flutter derivatives

Based on the discussions in Section 2.3 and 3.2, a simulation test grid of 7 × 7 × 3 (i.e., no. of geometries × no. of reduced velocities × DoF) resulting in a total of 147 simulations were carried out to obtain the time history of aeroelastic forces. As already stated, the aerodynamic flutter derivatives were computed from the time history of aeroelastic forces using the method of least squares and the flutter derivatives are presented in the form of a response surface, which is a multi-variate function of deck shape (H) and the reduced velocity (U^*). The flutter derivatives in both the Scanlan and PoliMi notations are presented in Fig. 22 for A_i^*'s, where $i = 1, 2, 3$. Similar conclusion as highlighted in Section 4.4 are revealed by the response surfaces of flutter derivative in Fig. 18, i.e., the variation in the magnitude of flutter derivatives across different reduced velocities fades away in the lower reduced velocity range while the same when plotted in PoliMi notation demonstrates interesting non-linearities as observed for a_i^*'s, where $i = 1, 2, 3$. Similar conclusions hold true for other flutter derivatives as well such as the H_i^*'s and h_i^*'s, where $i = 1, 2, 3$. The response surfaces for the flutter derivatives P_2^*, P_3^*, P_5^*, A_4^*, H_4^*, P_6^* and A_5^*, A_6^*, H_5^*, H_6^*, P_1^*, P_4^* are presented in Figs. 24 and 25 respectively. The Kriging surrogate is able to provide smooth, continuous and differentiable response surfaces for the 18 flutter derivatives even in regions of the surrogate domain showing high level of non-linearities (see Figs. 22 and 23), which is a fundamental feature for the implementation of the aeroelastic surrogate into aero-structural design optimization frameworks.

7. Buffetting response analysis and deck shape tailoring

The impact of deck shape modifications on the bridge aeroelastic performance is studied in this section by comparing the buffeting response obtained along the shape design domain under turbulent synoptic winds. The buffeting analysis is conducted in the frequency domain, as discussed in Section 2.4. Frequency domain analysis

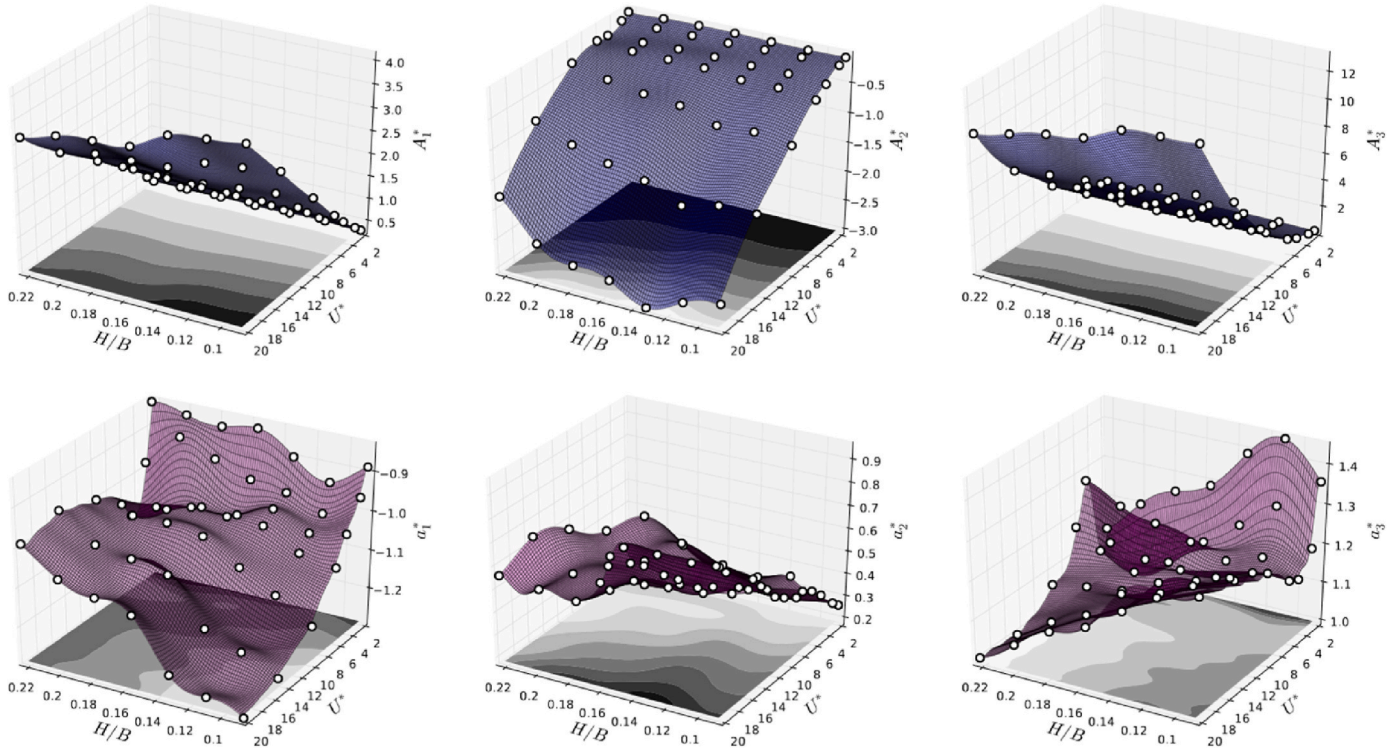

Fig. 22. Response surface of the flutter derivatives (A_1^*, A_2^*, A_3^*, a_1^*, a_2^*, a_3^*) for the design domain $\mathscr{D}_s$. Comparison of representations using Scanlan and PoliMi notation to highlight the non-linear behavior at low reduced velocities.

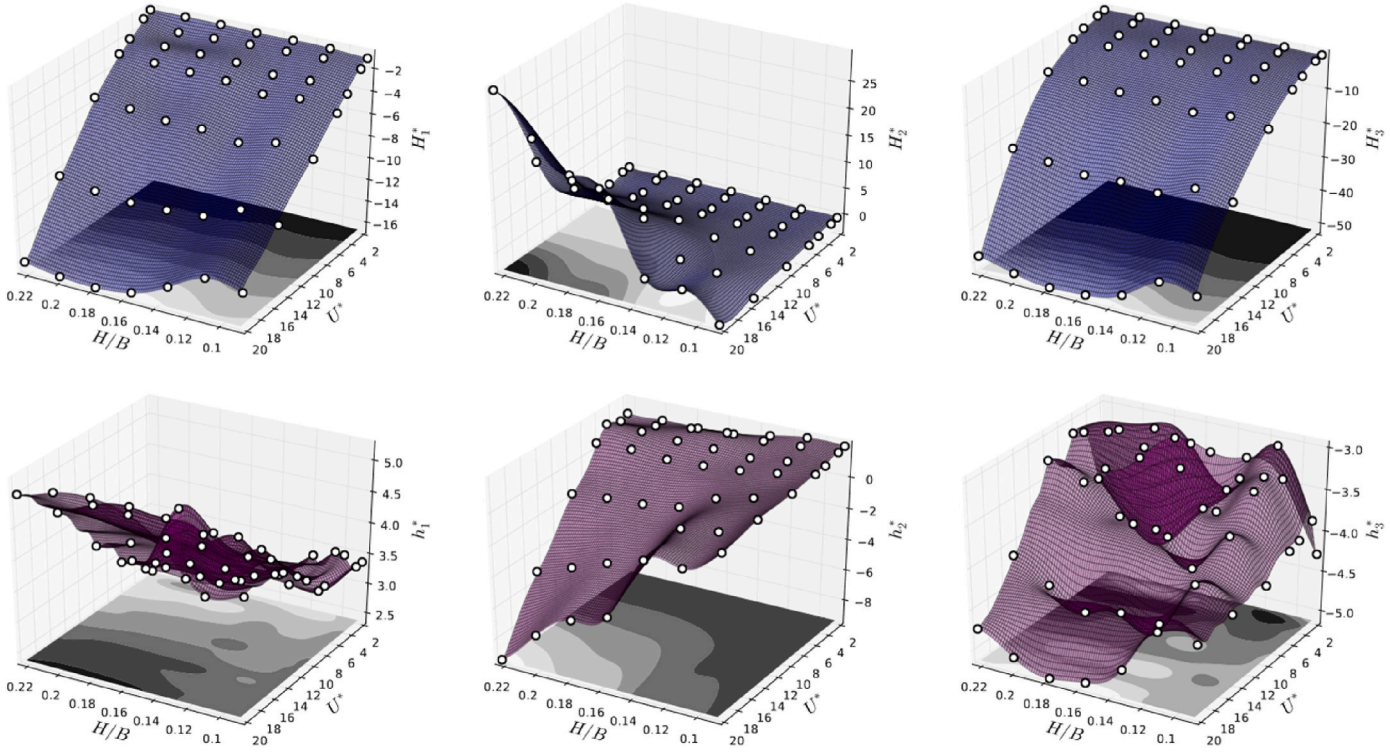

Fig. 23. Response surface of the flutter derivatives (H_1^*, H_2^*, H_3^*, h_1^*, h_2^*, h_3^*) for the design domain $\mathscr{D}_s$. Comparison of representations using Scanlan and PoliMi notation to highlight the non-linear behavior at low reduced velocities.

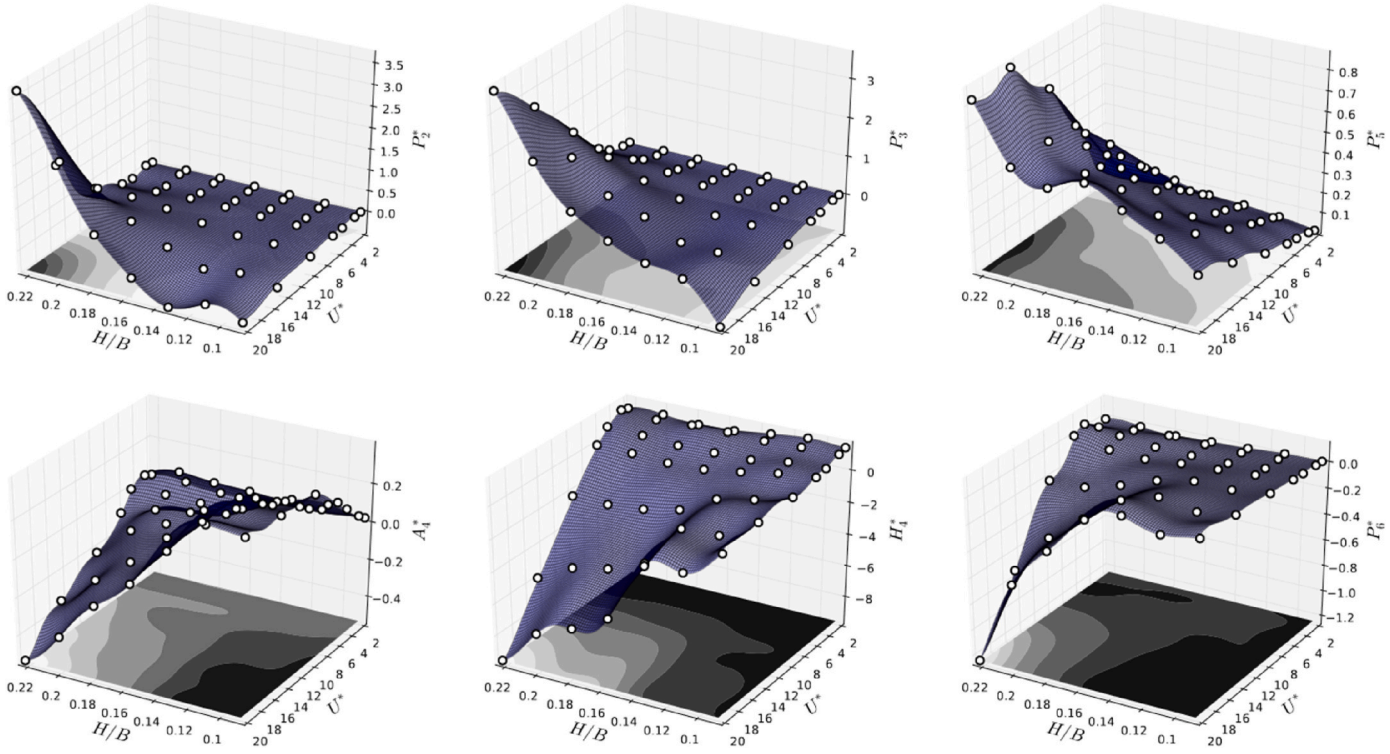

Fig. 24. Response surface of the flutter derivatives (P_2^*, P_3^*, P_5^*, A_4^*, H_4^*, P_6^*) for the design domain $\mathscr{D}_s$ represented using the Scanlan notation.

considers the frequency dependency of the fluid-structure interaction parameters, namely the flutter derivatives and admittance functions, which permits taking into account their non-linear features. However, it does not consider their sensitivity to the time-variant angle of attack. Hence, frequency domain analysis is a good alternative to studying the buffeting response of bluff decks with nonlinear aerodynamics under synoptic winds where the variations in the angle of attack and mean velocity are negligible. The test case adopted consists of a 1-node 3-DoF

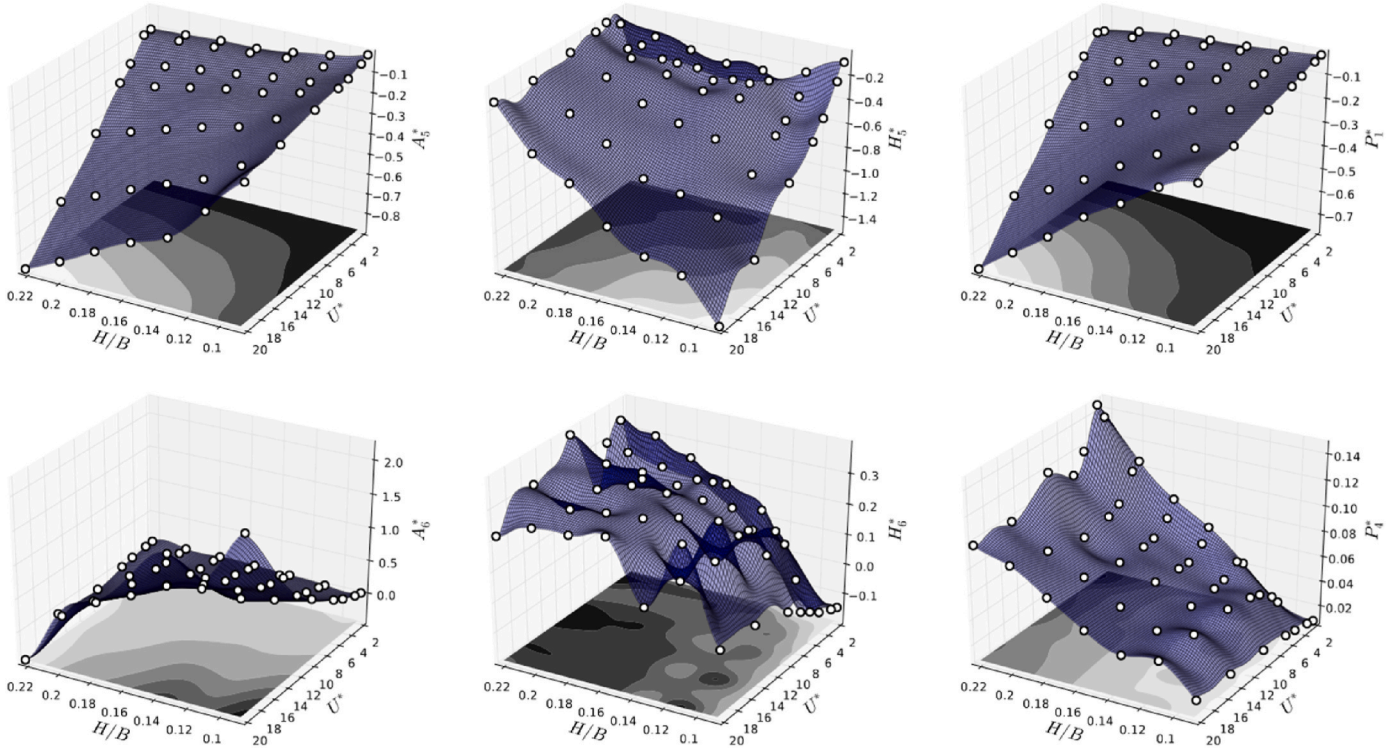

Fig. 25. Response surface of the flutter derivatives (A_5*, A_6*, H_5*, H_6*, P_1*, P_4*) for the design domain $\mathscr{D}_s$ represented using the Scanlan notation.

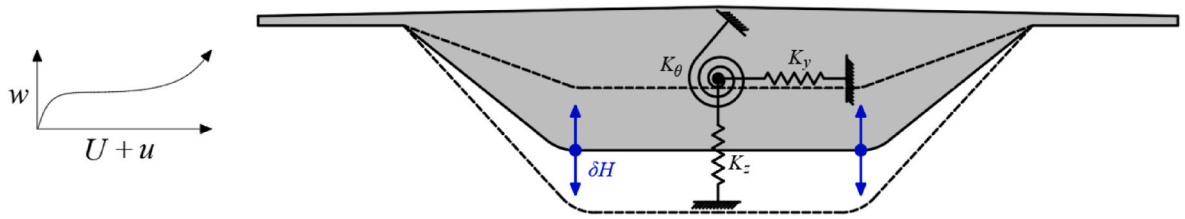

Fig. 26. Schematic representation of the 1-node 3-DoF system with variable depth and under the action of turbulent wind used as a demonstration example for the wind-resistant design of the deck.

system with a variable depth, as shown in Fig. 26. Changes in the deck depth impact the aerodynamic and aeroelastic properties. Aiming at focusing on this effect and for the sake of simplicity, the mechanical properties are kept constant, adopting the values reported in Table 10. However, it must be noted that deck shape modifications notably influence the natural frequencies and mode shapes due to variations in the translational and torsional moments of inertia and mass moments of inertia. This data was taken from the mechanical and dynamic properties of the Miradoiros Bridge (Baldomir et al., 2010; Cid Montoya et al., 2018a), a cable-stayed bridge project with a main span of 658 m. The aerodynamic dimensions adopted for the deck are 22 m chordwise width and 1 m spanwise length. These parameters were selected to boost the influence of nonlinear features at low reduced velocities on the buffeting response at a mean wind velocity of $U_{mean} = 40$ m/s. The resulting reduced velocities associated with the lateral, vertical, and torsional natural frequencies reported in Table 10 are $U_y^* = 7.19$, $V_z^* = 4.64$, and $V_\theta^* = 2.40$, respectively. These values are clearly in the low reduced velocity range, where more nonlinear features can be observed in the flutter derivatives, as shown in Fig. 19. Slight changes in the natural frequencies lead to variations in the reduced velocities that can cause drastic changes in the flutter derivatives. For instance, the value of the A_3^* for deck cross-section with high depth is very sensitive to changes in U^* in the region $U^* = [3, 7.5]$, as can be anticipated from Figs. 18 and 19, which has an impact on the buffeting response.

Table 10
Structural data used for the 1-node 3-DOF deck structural system used as a demonstration example for the wind-resistant design of the deck.

Quantity	Description	Value
M [T/m]	Mass per unit length	22.66
I_M [T m^2/m]	Moment of inertia per unit of length	4435.80
f_y [Hz]	Lateral structural eigenfrequency	0.253
f_z [Hz]	Vertical structural eigenfrequency	0.392
f_θ [Hz]	Torsional structural eigenfrequency	0.758
ξ [-]	Damping ratio (for all modes)	0.015

7.1. Synoptic wind modeling

The buffeting analysis considers a turbulent synoptic wind, assuming negligible variations in the angle of attack and mean wind velocity. The wind is modeled adopting a turbulence intensity of $I_u = \sigma_u/U = 0.07$ in the horizontal flow direction while a turbulence intensity of $I_w = \sigma_w/U = 0.03$ in the vertical direction. The integral length scales in the horizontal and vertical direction are $L_u = 200$ m and $L_w = 20$ m, respectively. The Von Karman spectrum (Von Kármán, 1948) is adopted for the diagonal terms (S_{uu} and S_{ww}) of the cross-power spectrum matrix, while

the off-diagonal terms are equated to 0. The air density is taken as $\rho = 1.22$ kg/m^3. These reference values are based on previous studies, for instance, Diana et al., 2020a; Patruno and Ricci, 2017.

7.2. Buffeting response trends in the shape design domain

The PSD of lateral, vertical, and torsional accelerations of the 1-node 3-DoF system described above are presented in Fig. 27 (a), (b), and (c), respectively. These PSDs were calculated using the aeroelastic surrogate model to emulate the 18 flutter derivatives for each deck design candidate. The torsional response is expressed as the equivalent vertical displacement of the deck side edge as $Z_{eq} = \theta B/2$. The three responses are monomodal functions, given the simplicity of the 1-node 3-DoF system. However, the effect of the buffeting forces and aeroelastic forces as a function of the deck shape is evident.

Fig. 27 (d), (e), and (f) show the RMS of acceleration of the lateral, vertical, and torsional responses calculated following the procedure described in Section 2.4.2. Using surrogate-based design methods permits the calculation of continuous, smooth, and differentiable response surfaces or curves, which facilitates design tasks and permits the implementation of gradient-based optimization algorithms. It can be seen the growing trend of the lateral and vertical responses as the depth of the cross-section increases. However, variations in the torsional response are minimal throughout the entire design domain. The RMS of accelerations are typically adopted as the acceptance criteria in standards and project specifications. The limit values prescribed in the Messina Bridge Project (Stretto di Messina, 2004) are $\ddot{u}_{RMS,max} = 0.15\,m/s^2$, $\ddot{w}_{RMS,max} = 0.25\,m/s^2$, and $\ddot{Z}_{eq,RMS,max} = 0.125\,m/\,s^2$. We adopt the same values here to conduct the buffeting-resistant design of the deck. The buffeting response of the deck is calculated using the aeroelastic surrogate reported in Section 6 for the emulation of the flutter derivatives and also the QST formulation (Eq. (6)). These results are shown in Fig. 27 (d), (e), and (f) as black and blue solid lines, respectively. The impact of the flutter derivatives on the buffeting response, even at not that high wind velocities, and the relevance of adopting the adequate modeling scheme, i.e., the aeroelastic surrogate for bluff deck design, can be clearly seen for each buffeting response. In fact, Fig. 27 (e) shows that the errors in the assessment of the RMS of vertical accelerations increase as the section becomes bluffer. This can be anticipated by analyzing the differences in the flutter derivatives reported in Fig. 20, particularly for H_i^*. On the other hand, the differences for the A_i^* are not that large, which results in a torsional response with slight differences, as shown in Fig. 27 (f). The lateral response reported in Fig. 27 (d) shows a very good agreement due to the similitude reported in Fig. 18 for the P_1^*, which has a key role on the lateral damping as explained in Fig. 17, obtained using either the AS or QST approaches.

7.3. Buffering-resistant design: deck shape tailoring

Deck shape modifications are very effective in mitigating buffeting-induced responses. Imposing a maximum response for the three degrees of freedom as described in Section 6.2. leads to the definition of the feasible design domain, which is graphically sketched in Fig. 28. This design is conditioned by the local climate (wind modeling), shape-dependent mechanical properties, and shape-dependent aerodynamic and aeroelastic properties. As shown in Fig. 27 (d), (e), and (f), the limitation is not active for the lateral and torsional responses. However, the limitation in the vertical response of $\ddot{w}_{RMS,max} = 0.25\,m/s^2$, conditions the feasible design domain. Hence, values of $H/B > 0.143$ lead to

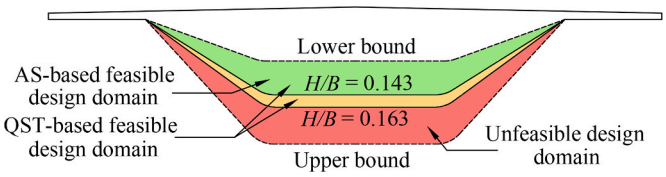

Fig. 28. Buffeting-resistant deck shape tailoring. Comparison of the feasible design domains obtained using the Aeroelastic Surrogate (AS)-based approach (green) and the QST-based approach (orange and green), and the unfeasible design domain (red).

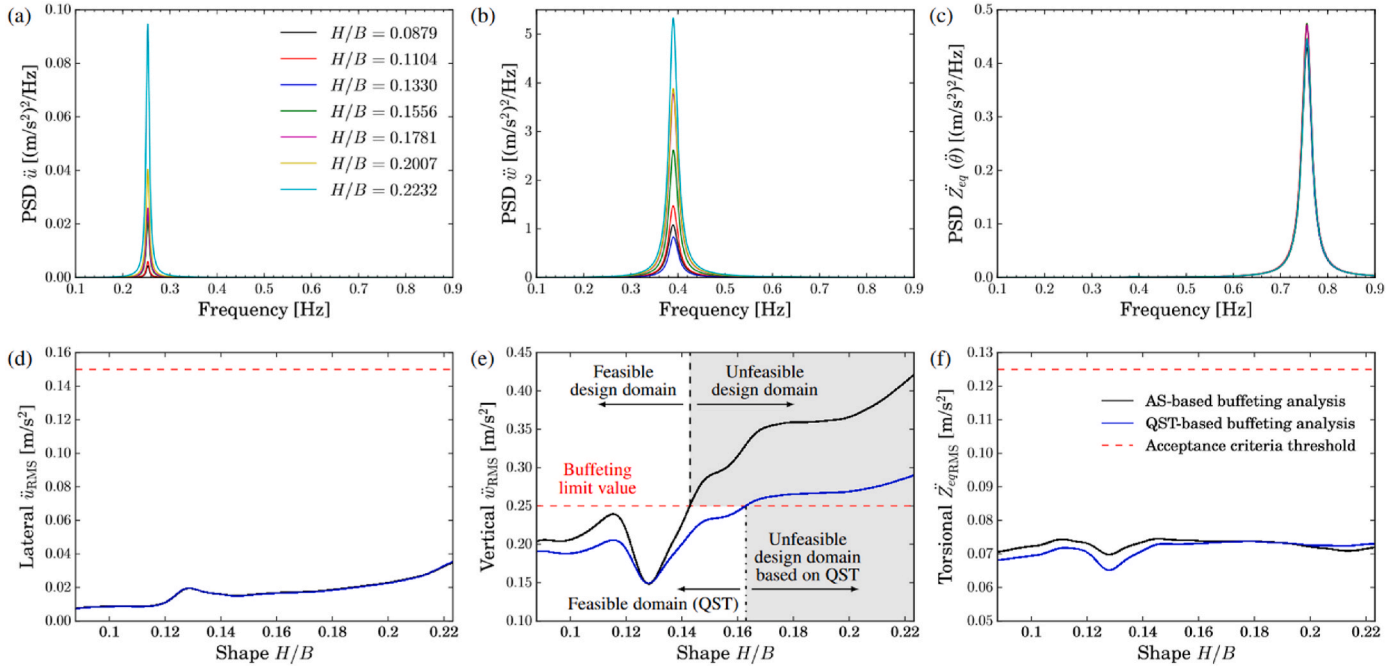

Fig. 27. Buffeting response of the 1-node 3-DoF system under a turbulent synoptic wind with a mean velocity of $U_{mean} = 40$ m/s. Subplots (a), (b), and (c) show the PSD of the lateral, vertical, and torsional degree-of-freedom for the seven samples used in the sampling plan (see Section 3.3.) using the Aeroelastic surrogate (AS) reported in Section 6. In subplots (d), (e), and (f), the RMS of accelerations as a function of the deck depth calculated using the AS and the QST are compared with the thresholds imposed as acceptance criteria, which permits the identification of the feasible and unfeasible design domain regions.

RMS of vertical accelerations higher than the maximum values adopted, which makes this region of the design domain unfeasible, as shown in Fig. 27. A different feasible design domain would be obtained if other mechanical properties, wind conditions, or limit values were adopted. Moreover, it is also important to highlight the role of the fluid-structure interaction modeling approach. Adopting the QST formulation instead of the proposed aeroelastic surrogate to estimate the flutter derivatives can cause drastic changes in the feasible design domain. Fig. 27 also shows in blue the buffeting response calculated using the QST and the resulting new feasible design domain corresponding to $H/B \leq 0.163$, which is also plotted in Fig. 28. It is important to remark that all deck shape designs between $H/B = 0.143$ and 0.163 surpasses the vertical threshold when performing the buffeting analysis with the AS. In particular, if the design obtained using the QST-based approach is selected ($H/B = 0.163$), the actual vertical buffeting acceleration calculated using the AS would be $\ddot{w}_{RMS} = 0.33\, m/s^2$, which would clearly surpass the imposed threshold of $\ddot{w}_{RMS,max} = 0.25\, m/s^2$. Consequently, the results obtained using the QST are not conservative for this case and can clearly pose a risk for the obtained designs. Hence, the definition of the feasible design domain, including bluff geometries at low reduced velocities, can only be defined by directly extracting the shape- and frequency-dependent flutter derivatives, hence avoiding the limitations of the QST formulation. This methodology opens the door to implementing aero-structural optimization frameworks to optimize the deck shape design of long-span bridges, considering flutter and buffeting responses effectively and accurately.

8. Concluding remarks

The self-excited forces of bluff decks present multiple nonlinearities that must be properly modeled to conduct the shape design and optimization of a deck cross-section accurately. This study proposes an aeroelastic surrogate to emulate the frequency-dependent self-excited forces for the shape design and optimization of bridge decks, including streamlined, bluff, and any other geometry or typology where the accuracy of the QST may be compromised, such as in truss and twin-box decks. Detailed verification and validation studies based on wind tunnel data of the static and dynamic CFD simulations were conducted to evaluate the performance of 2D URANS with the Menter's $k\omega$-SST turbulence model in a single-box bluff deck similar to the Sunshine Skyway bridge deck. The deck depth was systematically changed in order to understand and model its impact on the self-excited forces. Numerical simulations of forced vibrations in the three degrees of freedom permitted the extraction of the 18 flutter derivatives, which are required for modeling the aeroelastic response of bluff decks properly. This was done for multiple deck designs at several reduced velocities to collect enough information to build a comprehensive emulator. A special focus was set on the low reduced velocities range to capture potential nonlinearities by increasing the number of samples in that region of the domain. Then, a kriging surrogate was trained using the CFD datasets to produce an emulator that provides the values of the 18 flutter derivatives for a given shape and reduced velocity value. The computed response surfaces were analyzed using Scanlan's and PoliMi's formulations in order to properly visualize the nonlinear features and the asymptotic behavior at high reduced velocities which is imposed by the level of bluffness of the deck cross-section. As expected, notable differences were found with the flutter derivatives obtained using the QST formulation. The potential impact of these differences on a bridge aeroelastic response and wind-resistant design was analyzed by computing the buffeting response of a 1-node 3-DoF structural system with variable deck depth. The remarkable differences found in the H_i^* flutter derivatives, particularly for the bluffer geometries, led to drastic changes in the calculated RMS of buffeting vertical accelerations. This fact clearly impacts the eventual deck shape tailoring, seeking to keep those accelerations below a prescribed acceptance criteria threshold. Hence, the use of the proposed aeroelastic emulator in wind-resistant design frameworks involving non-streamlined deck cross-sections is fundamental for accurately balancing the contradictory design demands posed by the structural and aeroelastic requirements. Future research will delve into the implementation of the developed QST-free aeroelastic emulator into aero-structural optimization frameworks considering full bridge models, multiple design variables to simultaneously optimize the deck, cable-supporting system, and towers design, and multiple design constraints of structural and aeroelastic nature to control all relevant wind-induced responses.

CRediT authorship contribution statement

Sumit Verma: Writing – review & editing, Writing – original draft, Visualization, Validation, Software, Methodology, Investigation, Formal analysis, Data curation. **Miguel Cid Montoya:** Writing – review & editing, Writing – original draft, Visualization, Software, Project administration, Methodology, Investigation, Funding acquisition, Conceptualization. **Ashutosh Mishra:** Visualization, Software, Data curation.

Declaration of competing interest

The authors declare that they have no known competing financial interests or personal relationships that could have appeared to influence the work reported in this paper.

Data availability

Data will be made available on request.

Acknowledgements

This paper is based upon work supported by the National Science Foundation (NSF) under Grants No. CMMI-2301824. This support is gratefully acknowledged. Miguel Cid Montoya also acknowledges the support of the new faculty start-up funds provided by Texas A&M University-Corpus Christi.

References

Abbas, T., Kavrakov, I., Morgenthal, G., 2017. Methods for flutter stability analysis of long-span bridges: a review. Proc. Instit. Civil Eng.-Bridge Eng. 170 (4), 271–310. https://doi.org/10.1680/jbren.15.00039.

AIAA G-077-1998, 2002. Guide for the verification and validation of computational fluid dynamics simulations. https://doi.org/10.2514/4.472855.001.

Álvarez, A.J., Nieto, F., Kwok, K.C.S., Hernández, S., 2018. Aerodynamic performance of twin-box decks: A parametric study on gap width effects based on validated 2D URANS simulations. J. Wind Eng. Ind. Aerod. 182, 202–221. https://doi.org/10.1016/j.jweia.2018.09.004.

Álvarez, A.J., Nieto, F., Nguyen, D.T., Owen, J.S., Hernández, S., 2019. 3D LES simulations of a static and vertically free-to-oscillate 4:1 rectangular cylinder: effects of the grid resolution. J. Wind Eng. Ind. Aerod. 192, 31–44. https://doi.org/10.1016/j.jweia.2019.06.012.

Álvarez, A.J., Nieto, F., 2024. Correlation and modal analysis techniques for the study of the VIV response of a twin-box deck based on 3D LES simulations. Meccanica. https://doi.org/10.1007/s11012-024-01774-6.

Argentini, T., Rocchi, D., Somaschini, C., Spinelli, U., Zanelli, F., Larsen, A., 2022. Aeroelastic stability of a twin-box deck: Comparison of different procedures to assess the effect of geometric details. J. Wind Eng. Ind. Aerod. 220, 104878 https://doi.org/10.1016/j.jweia.2021.104878.

Arıoğlu, E., 2021. Importance of "heuristics" in suspension bridge engineering and 1915 Çanakkale bridge. Springer Tracts Transp. Traffic 17, 19–41. https://doi.org/10.1007/978-3-030-59169-4_2.

Arora, J.S., 2011. Introduction to Optimum Design, third ed. Elsevier Academic Press. https://doi.org/10.1016/C2013-0-15344-5.

Baldomir, A., Hernández, S., Nieto, F., Jurado, J.A., 2010. Cable optimization of a long span cable stayed bridge in La Coruña (Spain). Adv. Eng. Software 41, 931–938. https://doi.org/10.1016/j.advengsoft.2010.05.001.

Barni, N., Oiseth, O., Mannini, C., 2022. Buffeting response of a suspension bridge based on the 2D rational function approximation model for self-excited forces. Eng. Struct. 261, 114267 https://doi.org/10.1016/j.engstruct.2022.114267.

Bocciolone, M., Cheli, F., Curami, A., Zasso, A., 1992. Wind measurements on the Humber bridge and numerical simulations. J. Wind Eng. Ind. Aerod. 42 (1–3), 1393–1404. https://doi.org/10.1016/0167-6105(92)90147-3.

Borri, C., Costa, C., 2004. Quasi-steady analysis of a two-dimensional bridge deck element. Comput. Struct. 82 (13–14), 993–1006. https://doi.org/10.1016/j.compstruc.2004.03.019.

Brusiani, F., de Miranda, S., Patruno, L., Ubertini, F., Vaona, P., 2013. On the evaluation of bridge deck flutter derivatives using RANS turbulence models. J. Wind Eng. Ind. Aerod. 119, 39–47. https://doi.org/10.1016/j.jweia.2013.05.002.

Calamelli, F., Rossi, R., Argentini, T., Rocchi, D., Diana, G., 2024. A nonlinear approach for the simulation of the buffeting response of long span bridges under non-synoptic storm winds. J. Wind Eng. Ind. Aerod. 247, 105681 https://doi.org/10.1016/j.jweia.2024.105681.

Caracoglia, L., Jones, N.P., 2003. Time domain vs. frequency domain characterization of aeroelastic forces for bridge deck sections. J. Wind Eng. Ind. Aerod. 91, 371–402. https://doi.org/10.1016/S0167-6105(02)00399-9.

Chen, A., He, X., Xiang, H., 2002. Identification of 18 flutter derivatives of bridge decks. J. Wind Eng. Ind. Aerod. 90, 2007–2022. https://doi.org/10.1016/S0167-6105(02)00317-3.

Chen, W.F., Duan, L., 1999. Bridge Engineering Handbook. CRC Press.

Chen, X., Kareem, A., 2002. Advances in modeling of aerodynamic forces on bridge decks. J. Eng. Mech. 128 (11), 1193–1205, 10.1061/(ASCE)0733-9399(2002)128:11(1193).

Chen, X., Kareem, A., 2003. Aeroelastic analysis of bridges: effects of turbulence and aerodynamic nonlinearities. J. Eng. Mech. 129 (8), 885–895. https://doi.org/10.1061/(ASCE)0733-9399(2003)129:8(885.

Cheynet, E., Jakobsen, J.B., Snæbjörnsson, J., 2016. Buffeting response of a suspension bridge in complex terrain. Eng. Struct. 128, 474–487. https://doi.org/10.1016/j.engstruct.2016.09.060.

Cid Montoya, M., Nieto, F., Hernández, S., Kusano, I., Álvarez, A.J., Jurado, J.Á., 2018a. CFD-based aeroelastic characterization of streamlined bridge deck cross-sections subject to shape modifications using surrogate models. J. Wind Eng. Ind. Aerod. 177, 405–428. https://doi.org/10.1016/j.jweia.2018.01.014.

Cid Montoya, M., Hernández, S., Nieto, F., 2018b. Shape optimization of streamlined decks of cable-stayed bridges considering aeroelastic and structural constraints. J. Wind Eng. Ind. Aerod. 177, 429–455. https://doi.org/10.1016/j.jweia.2017.12.018.

Cid Montoya, M., Hernández, S., Nieto, F., Kareem, A., 2020. Aero-structural design of bridges focusing on the buffeting response: Formulation, parametric studies and deck shape tailoring. J. Wind Eng. Ind. Aerod. 204, 104243 https://doi.org/10.1016/j.jweia.2020.104243.

Cid Montoya, M., Nieto, F., Hernández, S., Fontán, A., Jurado, J.A., Kareem, A., 2021. Optimization of bridges with short gap streamlined twin-box decks considering structural, flutter and buffeting performance. J. Wind Eng. Ind. Aerod. 208, 104316 https://doi.org/10.1016/j.jweia.2020.104316.

Cid Montoya, M., Hernández, S., Kareem, A., 2022. Aero-structural optimization-based tailoring of bridge deck geometry. Eng. Struct. 270, 114067 https://doi.org/10.1016/j.engstruct.2022.114067.

Cid Montoya, M., Bai, H., Ye, M., 2023. Shaping bridge decks for VIV mitigation: A wind tunnel data-driven adaptive surrogate-based optimization method. J. Wind Eng. Ind. Aerod. 242, 105568 https://doi.org/10.1016/j.jweia.2023.105568.

Cid Montoya, M., 2024. Sequential aero-structural optimization method for efficient bridge design. Comput. Aided Civ. Infrastruct. Eng. 39, 319–344. https://doi.org/10.1111/mice.13005.

Chowdhury, A.G., Sarkar, P.P., 2003. A new technique for identification of eighteen flutter derivatives using a three-degree-of-freedom section model. Eng. Struct. 25 (14), 1763–1772. https://doi.org/10.1016/j.engstruct.2003.07.002.

Chowdhury, A.G., Sarkar, P.P., 2004. Identification of eighteen flutter derivatives of an airfoil and a bridge deck. Wind Struct. 7 (3), 187–202. https://doi.org/10.12989/was.2004.7.3.187.

Cruz, E.C., Andal, M.D.C., Rizabal, K.D.S., Inocencio, I.A.D., Kasilag, I.I.E.P., 2023. Typhoon hazard analysis of the Cebu-Cordova link expressway across Mactan channel. Coast. Eng. Proc. 37 (management), 135. https://doi.org/10.9753/icce.v37.management.135.

Davenport, A.G., 1963. Buffetting of a suspension bridge by storm winds. J. Struct. Div. 88 (3), 233–270. https://doi.org/10.1061/JSDEAG.0000773.

Davenport, A.G., 1967. The dependence of wind loads on meteorological parameters. In: Proceedings of Wind Effects on Buildings and Structures, Ottawa, Canada. September 11-15, 1967. https://www.aivc.org/sites/default/files/airbase_391.pdf.

Davenport, A.G., King, J.P.C., 1982a. The incorporation of dynamic wind loads into the design specifications for long-span bridges. In: Proceedings of ASCE Fall Convention and Structures Congress. New Orleans, Louisiana, USA.

Davenport, A.G., King, J.P.C., 1982b. A Study of Wind Effects for the Sunshine Skyway Bridge, Tampa, Florida - Concrete and Steel Alternates. Univ. Western Ontario. *Research Report BLWT-SS24-1982 and BLWT-SS25-1982*, October 1982.

Deng, Y., Li, S., Zhang, M., Lei, X., Chen, Z., 2021. Wake-induced vibrations of the hangers of the Xihoumen bridge. J. Bridge Eng. 26 (10), 05021012 https://doi.org/10.1061/(ASCE)BE.1943-5592.0001779.

Diana, G., Bruni, S., Cigada, A., Collina, A., 1993. Turbulence effect on flutter velocity in long span suspended bridges. J. Wind Eng. Ind. Aerod. 48 (2–3), 329–342. https://doi.org/10.1016/0167-6105(93)90144-D.

Diana, G., Rocchi, T., Argentini, S., Muggiasca, S., 2010. Aerodynamic instability of a bridge deck section model: Linear and nonlinear approach to force modeling. J. Wind Eng. Ind. Aerod. 98, 363–374. https://doi.org/10.1016/j.jweia.2010.01.003.

Diana, G., Fiammenghi, G., Belloli, M., Rocchi, D., 2013a. Wind tunnel tests and numerical approach for long span bridges: the Messina bridge. J. Wind Eng. Ind. Aerod. 122, 38–49. https://doi.org/10.1016/j.jweia.2013.07.012.

Diana, G., Rocchi, D., Argentini, T., 2013b. An experimental validation of a band superposition model of the aerodynamic forces acting on multi-box deck sections. J. Wind Eng. Ind. Aerod. 113, 40–58. https://doi.org/10.1016/j.jweia.2012.12.005.

Diana, G., Omarini, S., 2020. A non-linear method to compute the buffeting response of a bridge validation of the model through wind tunnel tests. J. Wind Eng. Ind. Aerod. 201, 104163 https://doi.org/10.1016/j.jweia.2020.104163.

Diana, G., Stoyanoff, S., Aas-Jakobsen, K., Allsop, A., Andersen, M., Argentini, T., Cid Montoya, M., Hernández, S., Jurado, J.A., Katsuchi, H., Kavrakov, I., Kim, H., Larose, G., Larsen, A., Morgenthal, G., Øiseth, O., Omarini, S., Rocchi, D., Svendsen, M., Wu, T., 2020a. IABSE Task Group 3.1 benchmark results. Part 1: Numerical analysis of a two-degree-of-freedom bridge deck section based on analytical aerodynamics. Struct. Eng. Int. 30 (3), 401–410. https://doi.org/10.1080/10168664.2019.1639480.

Diana, G., Stoyanoff, S., Aas-Jakobsen, K., Allsop, A., Andersen, M., Argentini, T., Cid Montoya, M., Hernández, S., Jurado, J.A., Katsuchi, H., Kavrakov, I., Kim, H., Larose, G., Larsen, A., Morgenthal, G., Øiseth, O., Omarini, S., Rocchi, D., Svendsen, M., Wu, T., 2020b. IABSE task group 3.1 benchmark results. Part 2: Numerical analysis of a three-degree-of-freedom bridge deck section based on experimental aerodynamics. Struct. Eng. Int. 30 (3), 411–420. https://doi.org/10.1080/10168664.2019.1661331.

Diana, G., Stoyanoff, S., Allsop, A., Amerio, L., Andersen, M.S., Argentini, T., Calamelli, F., Cid Montoya, M., de Goyet, V.V., Hernández, S., Jurado, J.A., Kavrakov, I., Larose, G., Larsen, A., Morgenthal, G., Rocchi, D., Svendsen, M.N., Wu, T., 2023. IABSE task group 3.1 benchmark results. Numerical full bridge stability and buffeting simulations. Struct. Eng. Int. 33 (4), 623–634. https://doi.org/10.1080/10168664.2022.2104188.

Díaz García, M.A., Cicero, S., Ramos Gutiérrez, O.R., 2018. Structural integrity assessment of the welded joints of the constitution of 1812 bridge (Cádiz, Spain). Eng. Fail. Anal. 90, 518–533. https://doi.org/10.1016/j.engfailanal.2018.04.012.

Donea, J., Huerta, A., Ponthot, J.-Ph, Rodriguez-Ferran, A., 2004. Encyclopedia of Computational Mechanics, Volume 2: Solids and Structures, Chapter Arbitrary Lagrangian-Eulerian Methods. Wiley, Chichester, pp. 413–438.

Dyrbye, C., Hansen, S.O., 1997. Wind Loads on Structures. John Wiley and Sons Ltd.

Febo, S., D'Asdia, P., 2010. Aeroelastic pre-design of streamlined multiple-box decks. In: *Atti del 11° Convegno Nazionale di Ingegneria del Vento*, IN-VENTO-2010, vol. 1.

Frandsen, J., 2004. Numerical bridge deck studies using finite elements. Part I: flutter. J. Fluid Struct. 19 (2), 171–191. https://doi.org/10.1016/j.jfluidstructs.2003.12.005.

Fransos, D., Bruno, L., 2010. Edge degree-of-sharpness and free-stream turbulence scale effects on the aerodynamics of a bridge deck. J. Wind Eng. Ind. Aerod. 98 (10–11), 661–671. https://doi.org/10.1016/j.jweia.2010.06.008.

Ferziger, J.H., Peric, M., 1996. Computational Methods for Fluid Dynamics. Springer-Verlag, *Heidelberg*, Germany.

Forrester, J., Sóbester, A., Keane, A.J., 2008. Engineering Design via Surrogate Modelling: A Practical Guide. John Wiley & Sons.

Haftka, R.T., Gürdal, Z., 1992. Elements of Structural Optimization. Springer, 9780792315049.

Hernández, S., 2010. Structural optimization. 1960-2010 and beyond. Comput. Technol. Rev. 2, 177–222. https://doi.org/10.4203/ctr.2.8.

Holmes, J.D., Bekele, S.A., 2021. Wind Loading of Structures, fourth ed. CRC Press. *Taylor and Fransis Group*.

Hui, M.C., Ding, Q.S., Xu, Y.L., 2005. Buffeting response analysis of stonecutters bridge. Trans. Hong Kong Inst. Eng. 12 (2), 8–21. https://doi.org/10.1080/1023697X.2005.10667998.

Hui, M.C.H., Wong, C.K.P., 2009. Stonecutters bridge – durability, maintenance and safety considerations. Struct. Infrastruct. Eng. 5 (3), 229–243. https://doi.org/10.1080/15732470601130337.

Iwamoto, M., Fujino, Y., 1995. Identification of flutter derivatives of bridge deck from free vibration data. J. Wind Eng. Ind. Aerod. 54–55, 55–63. https://doi.org/10.1016/0167-6105(94)00029-D.

Jain, A., Jones, N.P., Scanlan, R.H., 1996. Coupled aeroelastic and aerodynamic response analysis of long-span bridges. J. Wind Eng. Ind. Aerod. 60, 69–80. https://doi.org/10.1016/0167-6105(96)00024-4.

Jaouadi, Z., Abbas, T., Morgenthal, G., Lahmer, T., 2020. Single and multi-objective shape optimization of streamlined bridge decks. Struct. Multidiscip. Optim. 61, 1495–1514. https://doi.org/10.1007/s00158-019-02431-3.

Jasak, H., Tuković, Ž., 2007. Automatic mesh motion for unstructured finite volume method. Trans. FAMENA 30, 1–18.

Jiang, B., Zhou, Z., Yan, K., Hu, C., 2020. Effect of web inclination of streamlined flat box deck on aerostatic performance of a bridge. J. Bridge Eng. 26 (2), 04020126 https://doi.org/10.1061/(ASCE)BE.1943-5592.0001663.

Jones, N.P., Raggett, J.D., Ozkan, E., 2003. Prediction of cable supported bridge response to wind: coupled flutter assessment during retrofit. J. Wind Eng. Ind. Aerod. 91 (12–15), 1445–1464. https://doi.org/10.1016/j.jweia.2003.09.030.

Kareem, A., Wu, T., 2013. Wind-induced effects on bluff bodies in turbulent flows: Nonstationary, non-Gaussian and nonlinear features. J. Wind Eng. Ind. Aerod. 122, 21–37. https://doi.org/10.1016/j.jweia.2013.06.002.

Kareem, A., Wu, T., 2015. Changing dynamic of bridge aerodynamics. Proceedings of the Institution of Civil Engineers - Structures and Buildings 168 (2), 94–106. https://doi.org/10.1680/stbu.14.00022.

Kashima, S., Yanaka, Y., Suzuki, S., Mori, K., 2001. Monitoring the Akashi Kaikyo bridge: first experiences. Struct. Eng. Int. 11 (2), 120–123. https://doi.org/10.2749/101686601780347200.

Kavrakov, I., Morgenthal, G., 2017. A comparative assessment of aerodynamic models for buffeting and flutter of long-span bridges. Engineering 3 (6), 823–838. https://doi.org/10.1016/j.eng.2017.11.008.
King, J.P.C., Kopp, G., Vickery, P.J., Mikitiuk, M., Kong, L., 2005. A study of wind effects for Prospect Verona bridge, Maine, USA. https://www.maine.gov/mdot/contractors/projects/2012/007965.58-prospect-verona/wr007965.58.pdf.
Kinney, J.W., Rothman, H., Stahl, F., 1966. Verrazano-narrow bridge: Fabrication and construction of superstructure. J. Construct. Div. 92 (2) https://doi.org/10.1061/JCCEAZ.0000161.
Krige, D.G., 1951. A statistical approach to some basic mine valuation problems on the Witwatersrand. J. South Afr. Inst. Min. Metall. 52 (6), 119–139. https://hdl.handle.net/10520/AJA0038223X_4792.
Kusano, I., Cid Montoya, M., Baldomir, A., Nieto, F., Jurado, J.Á., Hernández, S., 2020. Reliability based design optimization for bridge girder shape and plate thicknesses of long-span suspension bridges considering aeroelastic constraint. J. Wind Eng. Ind. Aerod. 202, 104176 https://doi.org/10.1016/j.jweia.2020.104176.
Kwok, K.C., Qin, X.R., Fok, C.H., Hitchcock, P.A., 2012. Wind-induced pressures around a sectional twin-deck bridge model: effects of gap-width on the aerodynamic forces and vortex shedding mechanisms. J. Wind Eng. Ind. Aerod. 110, 50–61. https://doi.org/10.1016/j.jweia.2012.07.010.
Laima, S., Li, H., 2015. Effects of gap width on flow motions around twin-box girders and vortex-induced vibrations. J. Wind Eng. Ind. Aerod. 139, 37–49. https://doi.org/10.1016/j.jweia.2015.01.009.
Larose, G.L., Davenport, A.G., King, J.P.C., 1992. Wind effects on long span bridges: consistency of wind tunnel results. J. Wind Eng. Ind. Aerod. 42 (1–3), 1191–1202. https://doi.org/10.1016/0167-6105(92)90126-U.
Larose, G.L., Livesey, F.M., 1997. Performance of streamlined bridge decks in relation to the aerodynamics of a flat plate. J. Wind Eng. Ind. Aerod. 69, 851–860. https://doi.org/10.1016/S0167-6105(97)00211-0.
Larose, G.L., 1999. Experimental determination of the aerodynamic admittance of a bridge deck segment. J. Fluid Struct. 13 (7–8), 1029–1040. https://doi.org/10.1006/jfls.1999.0244.
Larsen, A., Wall, A., 2012. Shaping of bridge box girders to avoid vortex shedding response. J. Wind Eng. Ind. Aerod. 104, 159–165. https://doi.org/10.1016/j.jweia.2012.04.018.
Lazzari, M., Vitalini, R.V., Saetta, A.V., 2004. Aeroelastic forces and dynamic response of long-span bridges. Int. J. Numer. Methods Eng. 60 (6), 1011–1048. https://doi.org/10.1002/nme.987.
Lazzari, M., 2005. Time domain modelling of aeroelastic bridge decks: A comparative study and an application. Int. J. Numer. Methods Eng. 62 (8), 1064–1104. https://doi.org/10.1002/nme.1238.
Li, H., He, X.H., Hu, L., Xu, G.J., 2021. Quantification of aerodynamic forces for truss bridge-girders based on wind tunnel test and kriging surrogate model. Adv. Struct. Eng. 24, 2161–2175. https://doi.org/10.1177/1369433221992497.
Lin, Y., Cheng, C.M., Wu, J.C., Lan, T.L., Wu, K.T., 2005. Effects of deck shape and oncoming turbulence on bridge aerodynamics. Tamkang J. Sci. Eng. 8 (1), 43–56. https://core.ac.uk/download/pdf/225190025.pdf.
Ludke, S., 2013. The golden gate bridge art deco suspension bridge masterpiece. Structures Congress 576–587. https://doi.org/10.1061/9780784412848.051.
Mannini, C., 2006. Flutter Vulnerability Assessment of Flexible Bridge Decks. University of Florence, Italy – TU Braunschweig, Germany, Verlag Dr, Mulller, Saarbrucken. PhD Dissertation. https://d-nb.info/983616051/34.
Mannini, C., Soda, A., VoB, R., Schewe, G., 2010. Unsteady RANS simulations of flow around a bridge section. J. Wind Eng. Ind. Aerod. 98 (12), 742–753. https://doi.org/10.1016/j.jweia.2010.06.010.
Mannini, C., 2015. Applicability of URANS and DES simulations of flow past rectangular cylinders and bridge sections. Computation 3 (3), 479–508. https://doi.org/10.3390/computation3030479.
Mannini, C., Sbragi, G., Schewe, G., 2016. Analysis of self-excited forces for a box-girder bridge deck through unsteady RANS simulations. J. Fluid Struct. 63, 57–76. https://doi.org/10.1016/j.jfluidstructs.2016.02.007.
Martin, L.A., Yousif, Z., Campbell, B.L., Furrer, M., Chynoweth, M., 2023. Planning and design of the Gordie Howe international bridge, north America. In: Proceedings of the Institution of Civil Engineers - Bridge Engineering 0 0:0, pp. 1–17. https://doi.org/10.1680/jbren.21.00057.
Matsumoto, M., Kobayashi, Y., Shirato, H., 1996. The influence of aerodynamic derivatives on flutter. J. Wind Eng. Ind. Aerod. 60, 227–239. https://doi.org/10.1016/0167-6105(96)00036-0.
McKay, M.D., Beckman, R.J., Conover, W.J., 1979. A comparison of three methods for selecting values of input variables in the analysis of output from a computer code. Technometrics 21 (2), 239–245. https://doi.org/10.2307/1268522.
Menter, F.R., Kuntz, M., Langtry, R., 2003. Ten years of industrial experience with the SST turbulence model. Turbulence. In: Proceedings of the Fourth International Symposium on Turbulence, Heat and Mass Transfer, vol. 4. Begell House, Antalya, Turkey, pp. 625–632.
Miyata, T., Akiyama, H., Sato, H., Toriyumi, Y., 1995. Full model wind tunnel study on the Akashi Kaikyo Bridge. In: Proceedings of the 9th International Conference on Wind Engineering, pp. 793–798.
Nasr, A., Kjellstrom, E., Bjornsson, I., Honfi, D., Ivanov, O.L., Johansson, J., 2020. Bridges in a changing climate: a study of the potential impacts of climate change on bridges and their possible adaptations. Struct. Infrastruct. Eng. 16 (4), 738–749. https://doi.org/10.1080/15732479.2019.1670215.
Neuhaus, C., Roesler, S., Höffer, R., Hortmanns, M., 2009. Identification of 18 flutter derivatives by forced vibration tests: a new experimental rig. In: In Proceedings Of the 5th European and African Conference On Wind Engineering (EACWE2009). Florence, Italy, paper no. 126.
Nieto, F., Owen, J.S., Hargreaves, D.M., Hernandez, S., 2015. Bridge deck flutter derivatives: Efficient numerical evaluation exploiting their interdependence. J. Wind Eng. Ind. Aerod. 136, 138–150. https://doi.org/10.1016/j.jweia.2014.11.006.
Nieto, F., Cid Montoya, M., Hernández, S., Kusano, I., Casteleiro, A., Álvarez, A.J., Jurado, J.Á., Fontán, A., 2020. Aerodynamic and aeroelastic responses of short gap twin-box decks: Box geometry and gap distance dependent surrogate based design. J. Wind Eng. Ind. Aerod. 201, 104147 https://doi.org/10.1016/j.jweia.2020.104147.
Noguchi, K., Ito, Y., Yagi, T., 2020. Numerical evaluation of vortex-induced vibration amplitude of a box girder bridge using forced oscillation method. J. Wind Eng. Ind. Aerod. 196, 104029 https://doi.org/10.1016/j.jweia.2019.104029.
Oberkampf, W.L., Trucano, T.G., 2002. Verification and validation in computational fluid dynamics. Prog. Aero. Sci. 38 (3), 209–272. https://doi.org/10.1016/S0376-0421(02)00005-2.
Øiseth, O., Rönnquist, A., Sigbjörnsson, R., 2010. Simplified prediction of wind-induced response and stability limit of slender long-span suspension bridges, based on modified quasi-steady theory: a case study. J. Wind Eng. Ind. Aerod. 98 (12), 730–741. https://doi.org/10.1016/j.jweia.2010.06.009.
Øiseth, O., Rönnquist, A., Sigbjörnsson, R., 2011. Time domain modeling of self-excited aerodynamic forces for cable-supported bridges: A comparative study. Comput. Struct. 89 (13–14), 1306–1322. https://doi.org/10.1016/j.compstruc.2011.03.017.
Olsson, A., Sandberg, G., Dahlblom, O., 2003. On Latin hypercube sampling for structural reliability analysis. Struct. Saf. 25 (1), 47–68. https://doi.org/10.1016/S0167-4730(02)00039-5.
Orcesi, A., O'Connor, A., Bastidas-Arteaga, E., Stewart, M.G., Imam, B., Kreislova, K., Schoefs, F., Markogiannaki, O., Wu, T., Li, Y., Salman, A., Hawchar, L., Ryan, P.C., 2022a. Investigating the effects of climate change on material properties and structural performance. Struct. Eng. Int. 32 (4), 577–588. https://doi.org/10.1080/10168664.2022.2107468.
Orcesi, A., O'Connor, A., Diamantidis, D., Sykora, M., Wu, T., Akiyama, M., Alhamid, A. K., Schmidt, F., Pregnolato, M., Li, Y., Salarieh, B., Salman, A.M., Bastidas-Arteaga, E., Markogiannaki, O., Schoefs, F., 2022b. Investigating the effects of climate change on structural actions. Struct. Eng. Int. 32 (4), 563–576. https://doi.org/10.1080/10168664.2022.2098894.
Patruno, L., Ricci, M., 2017. On the generation of synthetic divergence-free homogeneous anisotropic turbulence. Comput. Methods Appl. Mech. Eng. 315, 396–417. https://doi.org/10.1016/j.cma.2016.11.005.
Petersen, A., Ostenfeld, K.H., Andersen, E.Y., 1987. The Farø bridges, long life at low costs. In: Proc. ASCE Structures Congress'87, Orlando, Florida. August 1987.
Picheny, V., Ginsbourger, D., Roustant, O., Haftka, R.T., Kim, N.H., 2010. Adaptive designs of experiments for accurate approximation of a target region, ASME. J. Mech. Des. 132 (7), 071008 https://doi.org/10.1115/1.4001873.
Ricciardelli, F., Hangan, H., 2001. Pressure distribution and aerodynamic forces on stationary box bridge sections. Wind Struct. 4 (5), 399–412. https://doi.org/10.12989/was.2001.4.5.399.
Russo, S., Piana, G., Patruno, L., Carpinteri, A., 2023. Preliminary flutter stability assessment of the double-deck george Washington bridge. Appl. Sci. 13 (11), 6389. https://doi.org/10.3390/app13116389.
Sacks, J., Welch, W.J., Mitchell, T.J., Wynn, H., 1989. Design and analysis of computer experiments. Stat. Sci. 4 (4), 409–423. https://doi.org/10.1214/ss/1177012413.
Salvatori, L., Spinelli, P., 2007. A discrete 3D model for bridge aerodynamics and aeroelasticity: nonlinearities and linearizations. Meccanica 42, 31–46. https://doi.org/10.1007/s11012-006-9022-x.
Sarkar, P.P., Jones, N.P., Scanlan, R.H., 1994. Identification of aeroelastic parameters of flexible bridges. J. Eng. Mech. 120 (8), 1718–1742. https://doi.org/10.1061/(ASCE)0733-9399(1994)120:8(1718.
Šarkić, A., Fisch, R., Höffer, R., Bletzinger, K.-U., 2012. Bridge flutter derivatives based on computed, validated pressure fields. J. Wind Eng. Ind. Aerod. 104–106, 141–151. https://doi.org/10.1016/j.jweia.2012.02.033.
Šarkić, A., Rüdiger, H., Stanko, B., 2015. Numerical simulations and experimental validations of force coefficients and flutter derivatives of a bridge deck. J. Wind Eng. Ind. Aerod. 144, 172–182. https://doi.org/10.1016/j.jweia.2015.04.017.
Sarwar, M., Ishihara, T., Shimada, K., Yamasaki, Y., Ikeda, T., 2008. Prediction of aerodynamic characteristics of a box girder bridge section using the LES turbulence model. J. Wind Eng. Ind. Aerod. 96 (10–11), 1895–1911. https://doi.org/10.1016/j.jweia.2008.02.015.
Scanlan, R.H., Tomko, J.J., 1971. Airfoil and bridge deck flutter derivatives. J. Eng. Mech. Div. 97 (6), 1717–1737. https://doi.org/10.1061/JMCEA3.0001526.
Scanlan, R.H., 1987. On flutter and buffeting mechanisms in long-span bridges. In: Lin, Y. K., Schuëller, G.I., Spanos, P. (Eds.), Stochastic Structural Mechanics, Lecture Notes in Engineering, vol. 31. Springer, Berlin, Heidelberg. https://doi.org/10.1007/978-3-642-83254-3_19.
Scanlan, R.H., 1988. On flutter and buffeting mechanisms in long-span bridges. Probabilist. Eng. Mech. 3 (1), 22–27. https://doi.org/10.1016/0266-8920(88)90004-5.
Selvam, R.P., Govindaswamy, S., Bosch, H., 2002. Aeroelastic analysis of bridges using FEM and moving grids. Wind Struct. 5 (2–4), 257–266. https://doi.org/10.12989/was.2002.5.2_4.257.
Shahawy, M.A., Arockiasamy, M., 1996a. Analytical and measured strains in sunshine Skyway bridge. II. J. Bridge Eng. 1 (2), 87–97, 10.1061/(ASCE)1084-0702(1996)1:2(87).
Shahawy, M.A., Arockiasamy, M., 1996b. Field instrumentation to study the time-dependent behavior in sunshine Skyway bridge. I. J. Bridge Eng. 1 (2), 76–86. https://doi.org/10.1061/(ASCE)1084-0702(1996)1:2(76.

Shiraishi, N., Matsumoto, M., 1983. On classification of vortex-induced oscillation and its application for bridge structures. J. Wind Eng. Ind. Aerod. 14 (1–3), 419–430. https://doi.org/10.1016/0167-6105(83)90043-0.

Singh, L., Jones, N.P., Scanlan, R.H., Lorendeaux, O., 1996. Identification of lateral flutter derivatives of bridge decks. J. Wind Eng. Ind. Aerod. 60, 81–89. https://doi.org/10.1016/0167-6105(96)00025-6.

Stretto di Messina, 2004. Messina Strait Bridge: Basis of design and expected performance, (original in Italian: Ponte sullo Stretto di Messina: Fondamenti Progettuali e Prestazioni Attese per l' Opera di attraversamento). Technical report, Stretto di Messina Report GCG.F.04.01, 2004.

Strømmen, E., 2010. Theory of Bridge Aerodynamics. Springer Science & Business Media. https://doi.org/10.1007/978-3-642-13660-3.

Sun, D., Owen, J.S., Wright, N.G., 2009. Application of the k–ω turbulence model for a wind-induced vibration study of 2D bluff bodies. J. Wind Eng. Ind. Aerod. 97 (2), 77–87. https://doi.org/10.1016/j.jweia.2008.08.002.

Szechenyi, E., 1973. Etude du comportement aéroélastique du pont de Saint-Nazaire à Saint-Brévin. ONERA, Palaiseau, France. Report NT 2/3044 RY (in French).

Tamura, T., 1999. Reliability on CFD estimation for wind-structure interaction problems. J. Wind Eng. Ind. Aerod. 81 (1–3), 117–143. https://doi.org/10.1016/S0167-6105(99)00012-4.

Theodorsen, T., 1934. General theory of aerodynamic instability and the mechanism of flutter. NACA Report 496, 413–433.

Tinmitondé, S., He, X., Yan, L., 2022. Single-objective aerodynamic optimization of a streamlined bridge deck subjected to shape modification using a polynomial emulator and genetic algorithm. Struct. Multidiscip. Optim. 65 (12), 356. https://doi.org/10.1007/s00158-022-03459-8.

Tubino, F., 2005. Relationships among aerodynamic admittance functions, flutter derivatives and static coefficients for long-span bridges. J. Wind Eng. Ind. Aerod. 93 (12), 929–950. https://doi.org/10.1016/j.jweia.2005.09.002.

TxDOT, 2022. Independent Structural Analysis for the Corpus Christi Harbor Bridge Project. Texas Department of Transportation, Bridge Division, SYSTRA International Bridge Technologies. TM1001-5.

Von Kármán, T., 1948. Progress in the statistical theory of turbulence. Proc. Natl. Acad. Sci. USA 34 (11), 530–539. https://doi.org/10.1073/pnas.34.11.530.

Wang, Y., Chen, X., 2022. Extraction of aerodynamic damping and prediction of vortex-induced vibration of bridge deck using CFD simulation of forced vibration. J. Wind Eng. Ind. Aerod. 224, 104982 https://doi.org/10.1016/j.jweia.2022.104982.

Wang, Z.L., Zhao, L., Chen, H.L., Fang, G., Li, K., Ge, Y., 2023. Flutter control of active aerodynamic flaps mounted on streamlined bridge deck fairing edges: An experimental study. Struct. Health Monit. 9970603 https://doi.org/10.1155/2023/9970603.

Wu, T., Kareem, A., 2013. Bridge aerodynamics and aeroelasticity: A comparison of modeling schemes. J. Fluid Struct. 43, 347–370. https://doi.org/10.1016/j.jfluidstructs.2013.09.015.

Wu, B., Wang, Q., Liao, H., Li, Y., Li, M., 2020. Flutter derivatives of a flat plate section and analysis of flutter instability at various wind angles of attack. J. Wind Eng. Ind. Aerod. 196, 104046 https://doi.org/10.1016/j.jweia.2019.104046.

Xu, F.Y., Ying, X.Y., Zhang, Z., 2014. Three-degree-of-freedom coupled numerical technique for extracting 18 aerodynamic derivatives of bridge decks. J. Struct. Eng. 140 (11), 04014085 https://doi.org/10.1061/(ASCE)ST.1943-541X.0001009.

Xu, F., Wu, T., Ying, X., Kareem, A., 2016. Higher-order self-excited drag forces on bridge decks. J. Eng. Mech. 142 (3), 06015007 https://doi.org/10.1061/(ASCE)EM.1943-7889.0001036.

Xu, G.J., Kareem, A., Shen, L., 2020. Surrogate modeling with sequential updating: applications to bridge deck–wave and bridge deck–wind interactions. J. Comput. Civ. Eng. 34, 04020023 https://doi.org/10.1061/(ASCE)CP.1943-5487.0000904.

Xue, Z., Han, B., Zhang, H., Xin, D., Zhan, J., Wang, R., 2021. External suction-blowing method for controlling vortex-induced vibration of a bridge. J. Wind Eng. Ind. Aerod. 215, 104661 https://doi.org/10.1016/j.jweia.2021.104661.

Yondo, R., Andrés, E., Valero, E., 2018. A review on design of experiments and surrogate models in aircraft real-time and many-query aerodynamic analyses. Prog. Aero. Sci. 96, 23–61. https://doi.org/10.1016/j.paerosci.2017.11.003.

Zasso, A., 1996. Flutter derivatives: advantages of a new representation convention. J. Wind Eng. Ind. Aerod. 60, 35–47. https://doi.org/10.1016/0167-6105(96)00022-0.

Zasso, A., Stoyanoff, S., Diana, G., Vullo, E., Khazem, D., Serzan, K., Pagani, A., Argentini, T., Rosa, L., Dallaire, P.O., 2013. Validation analyses of integrated procedures for evaluation of stability, buffeting response and wind loads on the Messina Bridge. J. Wind Eng. Ind. Aerod. 122, 50–59. https://doi.org/10.1016/j.jweia.2013.07.013.

Zheng, J., Fang, G., Wang, Z., Zhao, L., Ge, Y., 2023. Shape optimization of closed-box girder considering dynamic and aerodynamic effects on flutter: A CFD-enabled and Kriging surrogate-based strategy. Eng. Appl. Comput. Fluid Mech. 17 (1) https://doi.org/10.1080/19942060.2023.2191693.

Zhu, L.D., Xu, Y.L., 2005. Buffeting response of long-span cable-supported bridges under skew winds. Part 1: Theory. J. Sound Vib. 281 (3–5), 647–673. https://doi.org/10.1016/j.jsv.2004.01.026.

Zhuo, L., Liao, H., Zhou, Q., Li, M., 2022. Identification of aerodynamic derivatives of a box-girder bridge deck with twin active flaps using CFD simulations. J. Brg. Eng. 27 (3), 4022002 https://doi.org/10.1061/(ASCE)BE.1943-5592.0001830.